Spherically-symmetric inhomogeneities in general relativity and their effects in cosmology

Do Young Kim

Astrophysics Group
Cavendish Laboratory

and

Newnham College

2018 Dec

A dissertation submitted for the degree of Doctor of Philosophy

Summary

Name: Do Young Kim

Title: Spherically-symmetric inhomogeneities in general relativity and their effects in cosmology

Spherically-symmetric solutions are relevant in many areas of cosmology, from perturbations in the early Universe to growth of large scale structures in the later eras. In this thesis, we first focus on a comparison between the tetrad-based method and the widely used Lemaître-Tolman-Bondi (LTB) model for spherically-symmetric systems. We demonstrate that the tetrad-based method does not suffer from the gauge freedoms inherent to the LTB model, naturally accommodates non-zero pressure and has a more transparent physical interpretation.

Next we apply the tetrad-based method to a generalised form of 'Swiss cheese' model, which consists of an interior spherical region surrounded by a spherical shell of vacuum that is embedded in an exterior background universe, and verify the validity of Birkhoff's theorem at both the metric and tetrad level. Using this model, we reconsider critically the original theoretical arguments underlying the so-called $R_h = ct$ cosmological model, which has recently received considerable attention. These considerations in turn illustrate the interesting behaviour of a number of 'horizons' in general cosmological models. We also consider the theoretical arguments presented by Melia for the 'zero active mass' condition, which he claims is required by the Friedmann-Robertson-Walker spacetime. We demonstrate that this claim is false and results from a flaw in the logic of Melia's argument.

We then use the tetrad-based methodology for modelling a cosmic void, in particular for the void observed in the direction of Draco in the WISE-2MASS galaxy survey, and a corresponding cosmic microwave background (CMB) temperature decrement in the Planck data in the same direction. We find that the present-day density and velocity profiles of the void are not well constrained by the existing data, so that void models produced from the tetrad based and LTB approaches can differ substantially while remaining broadly consistent with the observations.

We next consider the effect of pressure on perturbations. We develop both an analytic and a numerical approach for solving the field equations for a fluid with a fixed equation of

state. We find an exact analytic solution for linearised equations, which may be novel in form, and which can be used to select the appropriate growing modes that can be used as an initial condition for evolving clusters and voids. Applying this to radiation as an example, we find oscillatory behaviour which corresponds to the initial stages of what become baryon acoustic oscillations. We then develop a numerical method for solving the field equations, which we use to compare behaviour of radiation waves in the non-linear and linear regimes. We find that non-linear oscillations travel faster than linear waves, which is interestingly analogous to non-linear waves in ocean waves. We also examine perturbations of fluids with a negative equation of state parameter, w, and find that at certain scales and range of w, it can support the growth of structure.

Finally, we consider the effect of pressure on photon propagation. We derive analytic expressions for pressure using a spherical top-hat density model, and use these to calculate the effect of pressure on the photon's path and energy. We find that the effect of pressure is negligible for fluids at cosmological densities and that it is valid to ignore it when propagating a photon.

Contents

Declaration

This dissertation is the result of my own work and includes nothing which is the outcome of work done in collaboration except as declared in the Preface and specified in the text. Throughout this dissertation the plural pronoun 'we' is used for stylistic reasons and should be taken to refer to either the singular author, or to the author and her thesis advisors.

It is not substantially the same as any that I have submitted, or, is being concurrently submitted for a degree or diploma or other qualification at the University of Cambridge or any other University or similar institution except as declared in the Preface and specified in the text. I further state that no substantial part of my dissertation has already been submitted, or, is being concurrently submitted for any such degree, diploma or other qualification at the University of Cambridge or any other University or similar institution except as declared in the Preface and specified in the text.

It does not exceed the prescribed word limit for the relevant Degree Committee.

Acknowledgements

I offer my sincerest thanks to my supervisors, Professors Anthony Lasenby and Mike Hobson, for their support and encouragement over the years, and their understanding during difficult times. Without their guidance and advice this work would not have been possible.

My life in the department would not have been the same without the fun and amusing chats I had with my fellow PhD students, Carina Negreanu, Sonke Hee, James Luis, Lukas Hergt, Haoyang Ye, and Yun-Cherng Lin. I would like to thank Becky Williams for the coffee break chats and the Churchill lunch crew for entertaining conversations and pointing me to (relatively) good food in West Cambridge. I am glad I have had the opportunity to meet such a wonderful group of people.

I cannot express enough of my gratitude towards my friends for their help in getting through the toughest times. I especially thank my friend Carina for always being there for me, during the highs and lows, both in person and via numerous messages. I am very grateful to Anna Ott, Becky Williams, Gráinne McGread, Lina Sleath, Hannah McQuail and Helen Davidge for their words of encouragement over the years and helping me keep a healthy balance in life.

I would like to take this opportunity to thank the members of the department for the help I've received over the years.

I express my deep gratitude to Samsung Scholarship for their financial support and their honourable mission to further the areas of human knowledge.

Finally I dedicate this thesis to my parents, without whom I would not be the person I am today.

Chapter 1

Introduction

The best theory of gravity we have so far is still Einstein's theory of general relativity. Throughout this dissertation, we employ the tetrad-based formalism in general relativity to study various cosmological effects in spherically-symmetric systems. In this Introduction, we introduce the concepts in Einstein's theory of gravity, the history and the motivations behind studying spherically-symmetric systems, and finally, the fundamentals of the tetrad-based approach to general relativity.

1.1 Einstein's general relativity

In the theory of general relativity, gravity is considered not as a force but as a manifestation of the curvature of spacetime. The presence of matter distorts spacetime thereby inducing curvature, which in turn affects other matter. Objects follow the shortest path (defined as a geodesic) between two points in a curved spacetime, resulting in the perceived effect of gravity. Other fundamental forces are still modelled as fields but on the background of spacetime.

Using variational principles, the physics of general relativity can be encapsulated by the Einstein–Hilbert action,

$$S_{\rm EH} = \int R\sqrt{-g}d^4x, \tag{1.1}$$

where g is the determinant of the metric tensor, $g_{\mu\nu}$, and R is the Ricci scalar. In the presence of matter, the action requires an extra term, such that

$$S = \frac{1}{2\kappa}S_{\rm EH} + S_{\rm M} = \int \left(\frac{1}{2\kappa}R + \mathcal{L}_{\rm M}\right)\sqrt{-g}d^4x, \tag{1.2}$$

where $\kappa = 8\pi G/c^4$. By applying the principle of least action, which denotes that the action is at an extremal with respect to variations of the metric, one arrives at Einstein's field equations,

$$R_{\mu\nu} - \frac{1}{2}Rg_{\mu\nu} = -\frac{8\pi G}{c^4}T_{\mu\nu}, \tag{1.3}$$

where $R_{\mu\nu}$ is the Ricci tensor, and $T_{\mu\nu}$ is the energy-momentum tensor, defined by

$$T_{\mu\nu} = \frac{-2}{\sqrt{-g}}\frac{\delta}{\delta g^{\mu\nu}}\left(\sqrt{-g}\mathcal{L}_{\mathrm{M}}\right). \tag{1.4}$$

The energy-momentum tensor describes the matter and non-gravitational forces. Due to the symmetries of spacetime, the field equations reduce to 6 independent equations, which are highly non-linear.

Spacetime is represented by a manifold, on which the metric tensor, $g_{\mu\nu}$, can be defined. The metric tensor is used to define the line-element, which describes the local geometry of a manifold at any point:

$$ds^2 = g_{\mu\nu}dx^\mu dx^\nu, \tag{1.5}$$

where dx^μ are infinitesimal coordinate displacements. The components of the metric tensor depend on the choice of the local coordinate system.

1.2 Spherically-symmetric systems

After Einstein's publication of the theory of general relativity in 1915 (Einstein 1915), many exact solutions of the field equations were proposed. The first solution was found by Karl Schwarzschild in 1916 (Schwarzschild 1916), for the spacetime around a fixed, static point mass in a vacuum, which is often used today to describe the spacetime around a black hole. Einstein himself proposed a static model of the Universe a year later by adding a cosmological constant term to the field equations (Einstein 1917). In 1922, Alexander Friedmann (Friedmann 1922) proposed a solution for a dynamic Universe, that could contract or expand with time. With a strong belief in the static nature of the Universe, Einstein quickly dismissed this as a mathematical curiosity that has no basis on physical nature, in the original version of his answer to Friedmann (Einstein 1923). Georges Lemaître (Lemaître 1927) independently arrived at similar results to Friedmann in 1927, but it largely went unnoticed at the time. Upon the experimental evidence found by Hubble (1929) that the Universe is indeed expanding, and Eddington's demonstration that Einstein's static model of the universe is unstable in 1930 (Eddington 1930), the expanding model of the Universe gained traction. With Robertson and Walker's further contributions (Robertson 1935, 1936b,a; Walker 1937) to Friedmann and Lemaître's solution in 1930s, the model came to be known as the Friedmann-Robertson-Walker

(also known as Friedmann-Lemaître-Robertson-Walker) model:

$$ds^2 = d\hat{t}^2 - S^2(\hat{t})\left(\frac{d\hat{r}^2}{1-k\hat{r}^2} + \hat{r}^2\, d\Omega^2\right), \tag{1.6}$$

where $\hat{t}$ and $\hat{r}$ are comoving coordinates, $S(\hat{t})$ is the scale factor, and k is the curvature parameter. The Friedmann-Robertson-Walker (FRW) model, which assumes that the universe is entirely homogeneous and isotropic, did surprisingly well to predict the evolution and characteristics of the Universe, and is still used even in the current era of precision cosmology.

Of course, the universe is not in fact homogeneous, as structures do indeed exist. The first inhomogeneous cosmological solution was found in 1933, when Lemaître investigated the solution for a spherically symmetric inhomogeneous fluid with non-uniform pressure, which he applied in the context of the static Einstein universe (Lemaître 1933). The solution was also independently found by (Tolman 1934) for dust, and developed further by Bondi (1947), who extended the solution outside of simply small deviations from the Einstein universe, by looking at a general case. The dust form of this model is called the Lemaître-Tolman-Bondi (or Lemaître-Tolman) model, and its metric is given by

$$ds^2 = d\hat{t}^2 - \frac{(\partial_{\hat{r}} R)^2}{1+2E(\hat{r})} - R^2 d\Omega^2, \tag{1.7}$$

where R is in general a function of $\hat{t}$ and $\hat{r}$, and $E(\hat{r}) > -1/2$. $E(\hat{r})$ is a function that is associated with the curvature of hypersurfaces with constant $\hat{t}$. As it also uses comoving coordinates, the FRW metric can be seen as a special case of the Lemaître-Tolman-Bondi (LTB) metric, with homogeneity imposed.

In this dissertation, we will be focussing on spherically-symmetric systems, particularly focussing on an inhomogeneity embedded in an expanding universe. Imposing spherical symmetry is useful in several ways. Firstly, spherical symmetry is ubiquitous in cosmology. Astrophysical objects such as planets are very well modelled as spherical. We can also apply spherically-symmetric models to clusters and voids, for instance to study the Sachs-Wolfe effect on the cosmic microwave background, as we shall see in Chapter 4. Even though spherical symmetry is an approximation for these structures, imposing this symmetry often enables us to access the physics in the system via an analytical approach, which would be difficult to achieve otherwise, and one would need to resort to a purely numerical method. In addition it enables us to probe into the non-linear regime, as we shall see in Chapter 5, which is not possible unless using an N-body simulation. Lastly, there has been a resurgence of interest in spherically-symmetric solutions due to the work in modified gravity, where imposing spherical symmetry is one of the few ways in which it is possible to extract a solution. Hence, not only does imposing spherical symmetry make the highly non-linear field equations easier to

solve, but it also enables us to develop an intuition for the physics behind the dynamics of the cosmological and astrophysical effects.

As we know the universe is expanding, it is of interest to examine the spacetime surrounding objects embedded in an expanding exterior, to ensure we include the effects of both. One of the first examples in this area is McVittie (1933, 1956)'s work on the spacetime outside a rigid body in an expanding, homogeneous universe, attempting to combine the Schwarzschild and FRW metrics. Another example is the Einstein-Straus model (Einstein & Straus 1945), in which the authors show that the Schwarzschild metric can be matched to an FRW model made of dust. The interpretation of McVittie's metric and the photon and particle orbits in this spacetime were studied by Nolan (1999); Nolan (2014). Further work was carried out by Nandra et al. (2012a,b); Nolan (2017) on this spacetime, particularly in the context of curved spacetimes and the astrophysical consequences. Nandra et al. (2013) extend this to study the evolution of a finite spherical inhomogeneity of uniform density, embedded in an exterior region with uniform density, where both are dynamic.

In practice, spherically-symmetric inhomogeneities are often modelled using the LTB model. Such models can incorporate an arbitrary (usually continuous) density profile for the central object, which is usually not compensated but can be made so by an appropriate choice of initial radial density and velocity profiles, where a model is compensated at some radius if the inhomogeneity does not have any gravitational effect beyond this point, and effectively 'looks homogeneous' beyond its boundary. Nonetheless, these models again assume both the interior and exterior regions to be pressureless, although it is possible to accommodate cosmological models with uniform pressure (Lynden-Bell & Bičák 2016; Sussman et al. 2005). The standard LTB metric can be extended to include non-uniform pressure but only when it is anisotropic (Sussman 2009; Mimoso et al. 2013; Del Campo et al. 2012). Lastly, a more generalised version of the LTB solutions has been presented in Lasky & Lun (2006) to describe a central object with pressure embedded in a static vacuum exterior.

There has been a recent resurgence of interest in the LTB model prompted by the possibility that it may explain the observations of accelerated expansion of the Universe without invoking dark energy. This might occur if we, as observers, reside in a part of the universe that happens to be expanding faster than the region exterior to it. By observing a source in the exterior region, one would then measure an *apparent* acceleration of the universe's expansion, but this would be only a local effect. The effects of local inhomogeneities on the apparent acceleration of the universe have been widely studied (Célérier 2012a,b; Bolejko & Célérier 2010; Bene & Csapo 2010; Kainulainen & Marra 2009; Marra et al. 2008, 2007; Alexander et al. 2009), and have been linked with the observations of distant Type-Ia supernova. However it has been shown that such models would induce variations in the CMB black-body spectrum through

scattering, which disagrees with observations Caldwell & Stebbins (2008); Clarkson (2012). In addition, LTB models have been used to study the effects of inhomogeneities on observed cosmological parameters, such as the Hubble constant (Romano & Vallejo 2015; Romano & Chen 2011a,b), and to calculate effects of a void as a possible explanation for the cold spot in the cosmic microwave background (CMB) (Szapudi et al. 2014; Nadathur et al. 2014).

However, the LTB model has some limitations. In addition to the usual restriction to pressureless systems, the LTB model is typically expressed in comoving coordinates and thus provides a Lagrangian picture of the fluid evolution that can be difficult to interpret. More importantly, the LTB metric contains a residual gauge freedom that necessitates the imposition of arbitrary initial conditions to determine the system evolution, as we shall see in Chapter 2.

Hence in this thesis, we use a different, tetrad-based method for solving the Einstein field equations for spherically-symmetric systems. The method was originally presented in Lasenby et al. (1998) in the language of geometric algebra, and was recently re-expressed in more traditional tetrad notation in Nandra et al. (2012a, 2013). The advantages of the approach are that it can straightforwardly accommodate non-uniform pressure, has no gauge ambiguities (except in vacuum regions, as we shall discuss later in Chapter 2) and is expressed in terms of a 'physical' (non-comoving) radial coordinate. As a result, in contrast to the LTB model, the method has a clear and intuitive physical interpretation. Indeed, the gauge choices employed result in equations that are essentially Newtonian in form. As our method employs an Eulerian picture of the fluid, it is straightforward to extract the velocity profile, and in fact many of the equations are expressed in terms of measurable quantities. In contrast, using the LTB model makes it easy to overlook the effects of velocity, which can have important physical consequences, as we shall show in Chapter 4.

1.3 Tetrad-based solution for spherical systems

The tetrad (or vierbein) formalism enables us to replace the choice of coordinates with a local basis in the tangent space. In 1929, Hermann Weyl first introduced the concept of tetrads into general relativity (Weyl 1929), when demonstrating how the concept of a spinor can be used in curved space, which previously could only be used in flat Lorentzian spacetime. In his paper, Weyl uses tetrads as a means to link Lorentzian space and curved Riemannian space at each point in spacetime.

The general theory of vierbeins, which is valid in any dimensions (then called 'vielbeins') and with metrics of any signature, is called the Cartan formalism (Cartan 1937). It was developed by Élie Cartan, a French mathematician whose contributions were in the theory of Lie groups, differential systems and differential geometry. His work in general relativity includes

the Einstein-Cartan theory, gravitation which includes non-zero torsion. Cartan developed his formalism when working on the method of the moving frames, where an ordered basis of a vector space is used to describe the extrinsic properties of a smooth manifold. Cartan helped develop key concepts in differential geometry, such as the Cartan connection, that are now used in general relativity for computing quantities in a curved spacetime.

We now describe the tetrad formalism as used in the theory of general relativity, following Weyl's prescription (Weyl 1929), and the notation that we use in the rest of this dissertation.

Consider a Riemannian spacetime in which events are labelled with a set of coordinates x^μ. At each point, there are corresponding coordinate basis vectors $\boldsymbol{e}_\mu$ that are related to the metric via $\boldsymbol{e}_\mu \cdot \boldsymbol{e}_\nu = g_{\mu\nu}$. At each point, we may also define a *local Lorentz frame* by another set of orthogonal basis vectors $\hat{\boldsymbol{e}}_a$ (expressed in Roman indices), which are not derived from any coordinate system. These basis vectors are related to the Minkowski metric $\eta_{ab} = \mathrm{diag}(1, -1, -1, -1)$ via $\hat{\boldsymbol{e}}_a \cdot \hat{\boldsymbol{e}}_b = \eta_{ab}$. A vector $\boldsymbol{v}$ can be expressed at any point in terms of its components in either basis, via $v_\mu = \boldsymbol{v} \cdot \boldsymbol{e}_\mu$ and $\hat{v}_a = \boldsymbol{v} \cdot \hat{\boldsymbol{e}}_a$. The relationship between the two sets of basis vectors is defined in terms of tetrads, or vierbeins $e_a{}^\mu$, where the inverse is given by $e^a{}_\mu$, such that

$$\hat{\boldsymbol{e}}_a = e_a{}^\mu \boldsymbol{e}_\mu, \qquad \boldsymbol{e}_\mu = e^a{}_\mu \hat{\boldsymbol{e}}_a. \tag{1.8}$$

One can easily show that the metric elements can be expressed in terms of the tetrads by $g_{\mu\nu} = \eta_{ab} e^a_\mu e^b_\nu$.

At each point, the local Lorentz frames define a family of ideal observers whose worldlines are the integral curves of the timelike unit vector field $\hat{\boldsymbol{e}}_0$. The three spacelike unit vector fields $\hat{\boldsymbol{e}}_i$ ($i = 1, 2, 3$) specify the spatial triad carried by the observer along a given worldline. One can think of the triad as defining the orthogonal spatial coordinate axes of a local laboratory frame that is valid very near the observer's worldline. The worldlines are not required to be time-like geodesics in general, and therefore the observers may be accelerating.

The Einstein–Hilbert action for general relativity is invariant under general coordinate transformations and local rotations of the Lorentz frames, which together constitute the gauge freedoms at our disposal. For a spherically-symmetric system, we start by introducing a set of spherical polar coordinates $[x^\mu] = (t, r, \theta, \phi)$ and their corresponding coordinate basis vectors $\boldsymbol{e}_\mu$ ($\mu = 0, 1, 2, 3$). We first demand that (minus) the angular part of the line-element $ds^2 = g_{\mu\nu}\, dx^\mu\, dx^\nu$ has the form $r^2\, d\Omega^2$, where $d\Omega^2 = d\theta^2 + \sin^2\theta\, d\phi^2$. Aside from trivial spatial rotations of the coordinates, which leave the description of the spherically-symmetric system unchanged, this choice absorbs the gauge freedoms associated with transformations of the r, θ and ϕ coordinates, and in particular lifts r from the status of an arbitrary radial coordinate to a quantity that is, in principle, physically measurable. It is a 'physical' (non-comoving)

coordinate[a] for which the proper area of a sphere of radius r is $4\pi r^2$. Note that there can be regions where this direct interpretation may be difficult, for example, inside the Schwarzschild radius where the r and t coordinates swap physical character (Plebański & Krasiński 2006). In addition there may be regions that are not covered by our 'physical' coordinates, such as in the closed universe, in which case we can easily transform to stereographic coordinates to explore the regions beyond the horizon (Lasenby et al. 1998; Nandra et al. 2012a). However, for practical purposes, such as modelling voids and overdensities, which will be explored in Chapter 4, these regions are normally beyond the physical region which needs to be considered.

The next step is to determine the general form of the tetrad $e_a{}^\mu$ that is consistent with spherical symmetry and this choice of coordinates. One immediately requires that, in (1.8), the coordinate basis vector pairs $\{\boldsymbol{e}_0, \boldsymbol{e}_1\}$ and $\{\boldsymbol{e}_2, \boldsymbol{e}_3\}$ decouple. Moreover, one can perform local rotations of the Lorentz frames to align $\hat{\boldsymbol{e}}_2$ and $\hat{\boldsymbol{e}}_3$ with the coordinate basis vectors $\boldsymbol{e}_2$ and $\boldsymbol{e}_3$ at each point. Consequently, the tetrad components $e_a{}^\mu$ may be written in terms of four unknown functions, which we denote by $f_1(r,t)$, $f_2(r,t)$, $g_1(r,t)$ and $g_2(r,t)$. Note that dependencies on both r and t will often be suppressed in the equations presented below, whereas we will usually make explicit dependency on either r and t alone. In particular, we may take the non-zero tetrad components and their inverses to be

$$\begin{aligned}
e_0{}^0 &= f_1, & e^0{}_0 &= g_1/(f_1 g_1 - f_2 g_2),\\
e_1{}^0 &= f_2, & e^0{}_1 &= -f_2/(f_1 g_1 - f_2 g_2),\\
e_0{}^1 &= g_2, & e^1{}_0 &= -g_2/(f_1 g_1 - f_2 g_2),\\
e_1{}^1 &= g_1, & e^1{}_1 &= f_1/(f_1 g_1 - f_2 g_2),\\
e_2{}^2 &= 1/r, & e^2{}_2 &= r,\\
e_3{}^3 &= 1/(r\sin\theta), & e^3{}_3 &= r\sin\theta.
\end{aligned} \tag{1.9}$$

Our remaining gauge freedoms lie in the ability to transform to a new time coordinate, which may be a function of t and r, and in performing local rotations of the Lorentz frames in the $(\hat{\boldsymbol{e}}_0, \hat{\boldsymbol{e}}_1)$-hyperplane (corresponding to a Lorentz boost in the radial direction at each point). The former possibility gives us complete freedom in the choice of the function f_2, and the greatest simplification of the tetrad components (1.9) is obtained by setting $f_2 \equiv 0$, which we call the Newtonian gauge because it allows simple Newtonian interpretations of the dynamics, as we shall see. In this gauge, the metric coefficients derived from the tetrad components lead to the line-element

$$ds^2 = \frac{g_1^2 - g_2^2}{f_1^2 g_1^2}\,dt^2 + \frac{2g_2}{f_1 g_1^2}\,dt\,dr - \frac{1}{g_1^2}\,dr^2 - r^2 d\Omega^2. \tag{1.10}$$

[a]These coordinates are sometimes called 'curvature coordinates' by some in the GR community.

Finally, the remaining gauge freedom (which leaves the line-element unchanged) can be employed (at least in non-vacuum regions) to choose the timelike unit frame vector $\hat{\boldsymbol{e}}_0$ at each point to coincide with the four-velocity of the fluid at that point. Note that throughout this thesis we consider Einstein equations with a perfect fluid source. Thus, by construction, the four-velocity $\boldsymbol{v}$ of a fluid particle (or an observer comoving with the fluid) has components $[\hat{v}^a] = [1, 0, 0, 0]$ in the tetrad frame. Since $v^\mu = e_a^{\ \mu}\hat{v}^a$, the four-velocity may be written in terms of the tetrad components and the coordinate basis vectors as $\boldsymbol{v} = f_1\boldsymbol{e}_0 + g_2\boldsymbol{e}_1$. Thus, the components of a comoving observer's four-velocity in the coordinate basis are simply $[v^\mu] \equiv [\dot{t}, \dot{r}, \dot{\theta}, \dot{\phi}] = [f_1, g_2, 0, 0]$, where dots denote differentiation with respect to the observer's proper time τ.

As a consequence of this final gauge choice, it is convenient to define the two linear differential operators

$$\begin{aligned} L_t &\equiv f_1\partial_t + g_2\partial_r, \\ L_r &\equiv g_1\partial_r. \end{aligned} \tag{1.11}$$

We may identify L_t as the derivative with respect to the proper time of a comoving observer, since $L_t = \dot{t}\partial_t + \dot{r}\partial_r = d/d\tau$, and similarly one may show that L_r coincides with the derivative with respect to the radial proper distance of a comoving observer. Moreover, since g_2 is the rate of change of the r coordinate of a fluid particle with respect to its proper time, it can be physically interpreted as the fluid 3-velocity. We will therefore, in general, use g_2 and v interchangeably in our analysis.

It is also convenient to introduce explicitly the spin-connection coefficients $F \equiv \omega^0{}_{11}$ and $G \equiv \omega^1{}_{00}$, as described in Nandra et al. (2012a), which are both, in general, functions of t and r. Since we are assuming standard general relativity, however, for which torsion vanishes, the spin-connection coefficients can be written entirely in terms of the tetrad components and their derivatives. For the torsion to vanish and for the resulting Riemann tensor to satisfy its Bianchi identity, the spin-connection coefficients F and G and the non-zero tetrad components f_1, g_1 and g_2 must satisfy the relationships

$$\begin{aligned} L_r f_1 &= -Gf_1 \Rightarrow f_1 = \exp\left\{-\int^r \tfrac{G}{g_1}dr\right\}, \\ L_r g_2 &= Fg_1, \\ L_t g_1 &= Gg_2, \end{aligned} \tag{1.12}$$

where the explicit solution for f_1 contains no arbitrary function of t, because one can always be absorbed by a further t-dependent rescaling of the time coordinate (which does not change f_2).

For matter in the form of a perfect fluid with proper density ρ and isotropic rest-frame pressure p, the Einstein field equations and the contracted Bianchi identities lead to the following

system[b] of dynamical and continuity equations (Lasenby et al. 1998)

$$\begin{aligned} L_r p &= -G(\rho + p), \\ L_r M &= 4\pi g_1 r^2 \rho, \\ L_t \rho &= -\left(\frac{2g_2}{r} + F\right)(\rho + p), \\ L_t M &= -4\pi g_2 r^2 p, \end{aligned} \tag{1.13}$$

where we have defined the function of t and r (in general)

$$M \equiv \tfrac{1}{2} r \left(g_2^2 - g_1^2 + 1 - \tfrac{1}{3}\Lambda r^2\right), \tag{1.14}$$

and Λ is the cosmological constant and M is the intrinsic mass (or energy) interior to r.

The physical interpretation of the functions F, G and M is straightforward. As shown in Nandra et al. (2012a), for an object in general radial motion (not necessarily co-moving with the fluid) with four-velocity components $[\hat{u}^a] = [\hat{u}^0, \hat{u}^1, 0, 0]$ in the tetrad frame, the corresponding components of the object's four-acceleration are

$$\begin{aligned} \hat{a}^0 &= \dot{\hat{u}}^0 + G\hat{u}^0\hat{u}^1 + F(\hat{u}^1)^2, \\ \hat{a}^1 &= \dot{\hat{u}}^1 + G(\hat{u}^0)^2 + F\hat{u}^0\hat{u}^1, \end{aligned} \tag{1.15}$$

and its proper acceleration is $\alpha = \sqrt{-\hat{a}^b \hat{a}_b}$, which provides a physical interpretation of the functions F and G. In particular, for the special case in which the object is co-moving with the fluid, one has $[\hat{u}^b] = [1, 0, 0, 0]$ and so $[\hat{a}^b] = [0, G, 0, 0]$. Thus the proper acceleration of a fluid particle is $\alpha = G$ in the radial direction. Indeed, the $L_r p$-equation in (1.13) shows that, in the absence of a pressure gradient, G vanishes and so the motion becomes geodesic. The physical interpretation of the function M can be obtained from the forms of the equations in (1.13) in which it appears. In particular, the $L_r M$-equation can be written simply as $\partial_r M = 4\pi r^2 \rho$, which shows that M plays the role of an intrinsic mass that is determined by the amount of mass-energy in a sphere of radius r. One can easily show that M is in fact equal to the Misner-Sharp mass (Nolan 1998; Nakao 1995), and hence is an intrinsic quantity. It is useful to note that Lasenby et al. (1998) have shown that in spherically symmetric systems, M and r appear explicitly in the eigenvalues of the Weyl tensor, and r is also a measurable quantity; hence the name 'physical' coordinate. As they are both intrinsic (i.e. measurable) quantities, it is useful to construct our equations in terms of these variables.

[b] In Lasenby et al. (1998), two further equations are given, namely $L_r g_1 = F g_2 + \frac{M}{r^2} - \frac{1}{3}\Lambda r - 4\pi r\rho$ and $L_t g_2 = G g_1 - \frac{M}{r^2} + \frac{1}{3}\Lambda r - 4\pi r p$, but these may be derived from the $L_r M$ and $L_t M$ equations, respectively, in combination with the definition of M given in (1.14).

The equations (1.12)–(1.14) thus have clear physical interpretations and contain no residual gauge freedom (in non-vacuum regions). In particular, given an equation of state $p = p(\rho)$, and initial data in the form of the density $\rho(r, t_0)$ and the velocity $g_2(r, t_0)$, the future evolution of the system is fully determined. This is because ρ determines p and M on a time slice and the definition of M then determines g_1. The equations for $L_r g_2$, $L_r p$ and $L_r f_1$ then determine the remaining information, namely F, G and f_1 respectively, on the time slice. Finally, the $L_t \rho$ equation and $L_t M$ equation (together with the definition of M) enable one to propagate ρ and g_2, respectively, to the next time slice and the repeat the process. The equations can thus be implemented numerically as a simple set of first-order update equations. This approach was illustrated in Lasenby et al. (1998, 1999); Dabrowski et al. (1998).

An alternative way of solving the system of equations (1.12)–(1.14), which was employed in Nandra et al. (2012a,b, 2013), is not to impose an equation of state, but instead specify a form for $\rho(r, t)$ for all t or, equivalently, a form for $M(r, t)$ followed by use of the $L_r M$. In general, the remaining equations need to be solved as a set of coupled PDEs. Nonetheless, as shown in Nandra et al. (2012a,b, 2013), if $\rho(r, t)$ is piecewise uniform in r, then one may combine the $L_t \rho$, $L_t M$ and $L_r M$ equations to obtain an ODE in r that may be solved to obtain an expression for the fluid velocity $g_2(r, t)$ and hence $F(r, t)$, albeit with each containing a time-dependent 'constant' of integration, and the definition of M then determines $g_1(r, t)$. One may then obtain the fluid pressure $p(r, t)$ by first using the $L_t M$ equation to eliminate f_1 from the $L_r p$ equation, which then yields the 'generalised Oppenheimer–Volkov' equation (Nandra et al. 2013)

$$\partial_r p = -\left(\frac{\rho + p}{r}\right) \cdot \left(\frac{M + 4\pi r^3 p - \frac{1}{3}\Lambda r^3 + r^2 v \partial_r v - 4\pi r^4 (\rho + p)(\partial_t M)^{-1} v \partial_t v}{(1 + v^2) r - 2M - \frac{1}{3}\Lambda r^3}\right).$$

This equation is, in fact, valid for any spherically-symmetric perfect fluid system and reduces to the standard Oppenheimer–Volkov equation with a cosmological constant (Oppenheimer & Volkoff 1939; Winter 2000) for a static spherically-symmetric system. After solving (1.16) for $p(r, t)$, which requires the imposition of a boundary condition on the pressure at some radius, one may complete the solution either by obtaining $f_1(r, t)$ from the $L_t \rho$ equation and hence $G(r, t)$ from any other equation that contains it, or by obtaining $G(r, t)$ from the $L_r p$ equation and then $f_1(r, t)$ from the $L_r f_1$ equation.

Finally, although the system of equations (1.12)–(1.14) accommodates non-zero pressure, it is worth considering briefly the special case of a pressureless fluid. In this case, the $L_r p$ equation forces G to vanish, so the motion of the fluid particles becomes geodesic and the $L_r f_1$ equation forces $f_1 = 1$. Consequently, the components in the coordinate basis of the four-velocity of a fluid particle are $[v^\mu] \equiv [\dot{t}, \dot{r}, \dot{\theta}, \dot{\phi}] = [1, g_2, 0, 0]$, where dots denote differentiation with respect to the particle's proper time τ. Since $\dot{t} = 1$, the coordinate time matches the proper time of all observers comoving with the fluid. Hence the Newtonian gauge is a synchronous one: a global

'Newtonian' time is recovered on which all comoving observers agree (provided all clocks are synchronised initially)[c]. Furthermore, combining the $L_t M$ equation and the definition of M yields $(\partial_t + g_2\partial_r)g_2 = -M/r^2 + \frac{1}{3}\Lambda r$, which has the form of the Euler equation in Newtonian fluid dynamics (recalling that g_2 is the fluid velocity v). Finally, setting $\Lambda = 0$ for a moment, the definition of M can itself be rearranged to give $\frac{1}{2}g_2 - M/r = \frac{1}{2}(g_1^2 - 1)$, which is the Bernoulli equation for zero pressure and total (non-relativistic) energy per unit mass $\frac{1}{2}(g_1^2 - 1)$ (i.e. after subtraction of the rest-mass energy).

1.4 Outline of thesis

We start off in Chapter 2 by comparing the tetrad-based approach to the LTB model, in particular by applying both to known cosmological cases, the Schwarzschild and FRW spacetimes, and highlight the advantages of the tetrad-based method. We then apply our method to the generalised Swiss-cheese model, which we then use to investigate a common misinterpretation of Birkhoff's theorem, namely that the gravitational field in a vacuum in a spherically-symmetric distribution is only affected by the interior mass.

Building on our findings, in Chapter 3 we next examine the theoretical claims behind the $R_\mathrm{H} = ct$ model, which start from the Swiss-cheese model considered in the previous chapter. We show that the central assumption, that the Hubble distance is constant, is not required. We also show that the argument presented in Melia (2016) that the FRW cosmology implies the zero active mass condition, $\rho + 3p = 0$, holds at all epochs is false. These considerations then reveal the behaviour of 'horizons' in homogeneous and isotropic cosmological models.

We then apply our tetrad-based approach to model a cosmic void in Chapter 4, assuming a pressureless fluid. We examine the Draco void as an example, by using the WISE-2MASS galaxy survey, and a corresponding cosmic microwave background temperature decrement in the Planck data in the same direction. We compare our model to the LTB model of the void provided by Finelli et al. (2016), and hence show the importance of considering both the velocity and density profiles when modelling a void from data, as the CMB decrements are sensitive to both.

In Chapter 5 we consider the effects of pressure on perturbations, focusing on fluids with a fixed equation of state. We first present an analytic approach and find exact solutions to the linearised field equations, and develop a numerical scheme which can be used in the non-linear regime. Applying this to radiation as an example, we find oscillatory behaviour which corresponds to the initial stages of what become baryon acoustic oscillations. By comparing the

[c] In fact, these findings still hold in the slightly more general case in which there is no pressure *gradient*, thereby allowing for the fluid to have a non-zero homogeneous pressure.

analytic and numerical methods, we investigate how the oscillations behave in the non-linear regime. We also examine the behaviour of perturbations in fluids with a negative pressure, and see whether they can support the growth of structure.

Lastly we consider the effect of pressure on photon propagation in Chapter 6. We derive analytic expressions for pressure using a spherical top-hat density model, and illustrate using an example that the effect of pressure on photon propagation is negligible except in the very early epoch when pressures are very high.

We adopt natural units $c = G = 1$ throughout this thesis, and the metric signature $(+, -, -, -)$.

Chapter 2

Spherically-symmetric solutions in general relativity

2.1 Introduction

Spherically-symmetric solutions in general relativity are of fundamental importance to the study of compact objects, black holes and cosmology. Indeed, two of the oldest and most commonly studied exact solutions of Einstein's field equations are spherically symmetric: the Schwarzschild metric (Schwarzschild 1916) describes the gravitational field outside a static spherical massive body, and the Friedmann–Robertson–Walker (FRW) metric (Friedmann 1922, 1924; Lemaître 1931; Robertson 1935, 1936b,a; Walker 1937) describes a homogeneous and isotropic universe in terms of the evolution of its scale factor with cosmic time. Moreover, it was not long before McVittie (McVittie 1933, 1956) combined the Schwarzschild and FRW metrics to produce a new spherically-symmetric solution that describes a point mass embedded in an expanding universe, although there still remains some debate regarding its physical interpretation (Kaloper et al. 2010; Lake & Abdelqader 2011).

Subsequently, there have been numerous studies of the general-relativistic dynamics of self-gravitating spherical systems. For example, Misner, Thorne & Wheeler (Misner et al. 1973) describe the spherically-symmetric collapse of a 'ball of dust' having uniform density and zero pressure that is embedded in a static vacuum exterior spacetime, and later generalise their results to incorporate pressure internal to the object. By contrast, 'Swiss cheese' models (Harwit 1998) consider an exterior expanding FRW universe, albeit pressureless, in which a

uniform pressureless spherical object is embedded and surrounded by a 'compensating void' that itself expands into the background and ensures that there is no net gravitational effect on the exterior universe.

A more realistic description than the Swiss cheese models is provided by models based on the Lemaître–Tolman–Bondi (LTB) solution (Lemaître 1933; Tolman 1934; Bondi 1947). As discussed in the Introduction, the LTB model usually is restricted to dust, although recently a more generalised version including pressure was presented in Lasky & Lun (2006), for a central object with pressure embedded in a static vacuum exterior. The LTB method however has some limitations; for example it contains a residual gauge freedom, as we shall see in Section 2.3, which requires some arbitrary initial conditions to 'fix' the gauge, which can make interpretations difficult.

In contrast we believe that the tetrad-based method has many advantages over the LTB method, as discussed in the Introduction. In Lasenby et al. (1999); Dabrowski et al. (1998), the authors apply the method to modelling the evolution of a finite-size, spherically-symmetric object with continuous radial density and velocity profiles that is embedded in an expanding background universe (either spatially-flat, open or closed) and compensated so that it does not exert any gravitational influence on the exterior universe; the fluid is assumed to be pressureless throughout. In Nandra et al. (2012a), the authors use the method to obtain solutions describing a point mass residing in either a spatially-flat, open or closed expanding universe containing a cosmological fluid with pressure. In the spatially-flat case, a simple coordinate transformation relates their solution to the corresponding one derived by McVittie, but for spatially-curved cosmologies their metrics are physically distinct from the corresponding McVittie metrics, as shown in Section 3.2 in Nandra et al. (2012a). Hence, we believe that the latter in fact do not necessarily describe spatially-curved cosmologies with a point mass in the centre, even though they may be solutions of Einstein's equations. In Nandra et al. (2013), the authors extend this study by applying the tetrad-based approach to obtain the solution describing the evolution of a finite spherical region of uniform interior density that is embedded in a background of uniform exterior density, where the fluid in both regions can support pressure and the expansion (or contraction) rates of the two regions are expressed in terms of interior and exterior Hubble parameters that are, in general, independent. They also derive a generalised form of the Oppenheimer–Volkov equation, valid for general time-dependent, spherically-symmetric systems.

In this Chapter, we present a comparison of our tetrad-based methodology with the LTB model for solving the Einstein field equations for spherically-symmetric systems. In particular, we focus on the issues of gauge ambiguity and the use of comoving versus 'physical' coordinate systems. We also clarify the correspondences, where they exist, between the two approaches. In

addition, we extend the analysis presented in Nandra et al. (2013) by applying our tetrad-based method to a generalised form of 'Swiss cheese' model, which consists of an interior spherical region surrounded by a spherical shell of vacuum that is embedded in an exterior background universe. In general, we allow the fluid in the interior and exterior regions to support pressure, and we demand neither that the interior region be compensated, nor that the interior and exterior regions be uniform. Nonetheless, our principal focus is the case in which the fluid in the interior and exterior regions has uniform (although, in general, different) densities. In particular, we pay special attention to the form of the solution in the intervening vacuum region and verify the validity of Birkhoff's theorem, the usual interpretation of which has recently been brought in question (Zhang & Yi 2012).

The structure of this Chapter is as follows. In Section 2.3 we compare our tetrad-based approach outlined in the Introduction to the more commonly-used LTB model. Note that the comparison serves as a pedagogical outline which presents the physical motivations behind each approach, with the aim of highlighting the advantages of using the tetrad-based method and 'physical' coordinates, by applying both methods to the familiar FRW and Schwarzschild spacetimes. We then present original results, where we apply our tetrad-based method to describe the evolution of a generalised form of 'Swiss cheese' model in Section 2.4 and investigate the validity of Birkhoff's theorem in its vacuum region in Section 2.5. Finally, we present our conclusions in Section 2.6.

2.2 Using the tetrad based approach

2.2.1 Application to Schwarzschild spacetime

As an illustration of our tetrad-based approach outlined in the Introduction, we now apply it to the special case in which the matter source is concentrated at the single point $r = 0$ and the cosmological constant vanishes (see also Lasenby et al. (1998)). For such a solution, $\rho = p = 0$ everywhere away from the origin and so $L_r M = 0$ and $L_t M = 0$, which together imply $M =$ constant. Retaining the symbol M for this constant, one finds that the system of equations (1.12)–(1.14) reduces just to the relationships (1.12) between the tetrad and spin-connection components and the definition of M in (1.14) (with $\Lambda \equiv 0$); no further equations yield new information.

We therefore have an under-determined system of equations and so some additional gauge-fixing is required to determine an explicit solution. This occurs because in the final part of our gauge-fixing procedure described in the Introduction, one chooses the timelike unit Lorentz frame vector at each point to coincide with the fluid four-velocity at that point, which clearly cannot be performed in a vacuum region. Nonetheless, one may instead choose the timelike

unit frame vector to coincide with the four-velocity $\boldsymbol{u}$ of some radially-moving test particle (which need not necessarily be in free-fall), so that its components in the tetrad frame are $[\hat{u}^a] = [1, 0, 0, 0]$ and hence in the coordinate basis one has $[u^\mu] \equiv [\dot{t}, \dot{r}, \dot{\theta}, \dot{\phi}] = [f_1, g_2, 0, 0]$, as previously. This ensures that our previous physical interpretations of the tetrad and spin-connection components still hold. It remains, however, to choose a particular class of radially-moving test particle, and the simplest and most natural choice is a radially free-falling particle that was released from rest at $r = \infty$. From the definition (1.14) of M (with $\Lambda \equiv 0$), one sees that g_1 corresponds to the total energy per unit rest mass of an infalling particle, and so for a particle released from rest at infinity one should adopt the gauge condition $g_1 = 1$. It is then a simple matter to obtain expressions for the remaining tetrad components and spin-connection coefficients. The resulting non-zero tetrad components are

$$f_1 = 1, \qquad g_1 = 1, \qquad g_2 = -\frac{2M}{r}, \tag{2.1}$$

and the spin-connection coefficients F and G read

$$F = \left(\frac{2M}{r}\right)^{-1/2} \frac{M}{r^2}, \qquad G = 0. \tag{2.2}$$

We note that the condition $G = 0$ is clearly consistent with the geodesic motion of the test particles.

The line-element (1.10) corresponding to the tetrad components (2.1) is given by

$$ds^2 = dt^2 - \left(dr + \sqrt{\frac{2M}{r}}\, dt\right)^2 - r^2\, d\Omega^2, \tag{2.3}$$

which we recognise as the Schwarzschild spacetime line-element expressed in terms of Painlevé–Gullstrand coordinates (Painlevé 1921; Gullstrand 1922). This coordinate system has a number of desirable features. For example, the line-element is regular for all positive values of r and the spacelike hypersurfaces t = constant have Euclidean geometry. Moreover, from (2.1), the non-zero components of the four-velocity of a particle released from rest at infinity are immediately

$$\dot{t} = 1, \qquad \dot{r} = -\sqrt{\frac{2M}{r}}, \tag{2.4}$$

and so we recover an essentially Newtonian description of the motion. In particular, we see that t coincides with the proper time of such particles.

It is also of interest to consider briefly how to recover the standard form of the Schwarzschild line-element in Schwarzschild coordinates. This may be achieved by fixing the gauge by instead choosing the preferred class of test particle to have fixed spatial coordinates, in particular $\dot{r} = 0$,

which immediately requires $g_2 = 0$. It is then straightforward to obtain the remaining tetrad components and spin-connection coefficients. One thus finds

$$f_1 = \left(1 - \frac{2M}{r}\right)^{-1/2}, \quad g_1 = \left(1 - \frac{2M}{r}\right)^{1/2}, \quad g_2 = 0, \tag{2.5}$$

and the spin-connection coefficients F and G are

$$F = 0, \qquad G = \left(1 - \frac{2M}{r}\right)^{-1/2} \frac{M}{r^2}. \tag{2.6}$$

We note that $G \neq 0$ is consistent with non-geodesic motion of the test particles. Moreover, the corresponding line-element (1.10) then takes the standard Schwarzschild form

$$ds^2 = \left(1 - \frac{2M}{r}\right) dt^2 - \frac{dr^2}{\left(1 - \frac{2M}{r}\right)} - r^2\, d\Omega^2. \tag{2.7}$$

There exists a subtlety in the presence of a horizon, however, since it is not possible inside it for a test particle to remain at fixed spatial coordinates, and hence one cannot have $g_2 = 0$. This is discussed in detail in Lasenby et al. (1998), where it is shown that the presence of a horizon is related to the onset of time-reversal asymmetry not easily identified using a wholly metric-based approach.

2.2.2 Application to FRW spacetime

As a second illustration of our approach, we apply it to the special case of a homogeneous and isotropic spacetime, as assumed in cosmology. This corresponds to setting ρ and p to be functions of t only. First we note that, unlike the Schwarzschild spacetime, there are no vacuum regions, and so no additional gauge-fixing will be required. It follows immediately from the $L_r p$ equation that $G = 0$ and then the $L_r f_1$ equation implies $f_1 = 1$. Since ρ is spatially uniform, one requires $M(r,t) = \frac{4}{3}\pi r^3 \rho$, which is consistent with the $L_r M$ equation. The $L_t M$ and $L_t \rho$ equations now jointly lead to the two conditions

$$F = \frac{g_2}{r}, \tag{2.8}$$

$$\partial_t \rho = -\frac{3g_2(\rho + p)}{r}, \tag{2.9}$$

but the first condition can only be consistent with $L_r g_2$ equation if $F = H(t)$ and $g_2 = rH(t)$. Finally, we obtain g_1 by first substituting the above expression for M into (1.14) and differentiating the result with respect to r to obtain the equation $L_r g_1 = (g_1^2 - 1)/r$, which may solved to yield $g_1^2 = 1 + r^2\phi(t)$, where $\phi(t)$ is an arbitrary function of t. Then the $L_t g_1$ equation implies that $\partial_t \phi = -2H(t)\phi$.

Thus, gathering our results together, the non-zero tetrad components are given by

$$\begin{aligned} f_1 &= 1, \\ g_1^2 &= 1 - kr^2 \exp\left\{-2\int^t H(t')\,dt'\right\}, \\ g_2 &= rH(t), \end{aligned} \tag{2.10}$$

where k is an arbitrary constant of integration, and the spin-connection coefficients F and G are

$$F = H(t), \qquad G = 0. \tag{2.11}$$

We note that the condition $G = 0$ demonstrates that the fluid particles move geodesically, since there are no pressure gradients. Moreover, on substituting the above results into (2.9) and the expression (1.14) for M, one obtains

$$\partial_t \rho = -3H(t)(\rho + p), \tag{2.12}$$

$$\tfrac{8}{3}\pi\rho = H^2(t) - \tfrac{1}{3}\Lambda + k\exp\left\{-2\int^t H(t')\,dt'\right\}. \tag{2.13}$$

Finally, differentiating (2.13) with respect to t and using (2.12), one also obtains the further (although clearly not independent) dynamical equation

$$\partial_t H(t) + H^2(t) - \tfrac{1}{3}\Lambda = -\tfrac{4}{3}\pi(\rho + 3p), \tag{2.14}$$

which we recognise as the standard 'acceleration' cosmological field equation expressed in terms of the Hubble parameter $H(t)$. Indeed, from (2.10), the non-zero components of the four-velocity of a fluid particle are immediately

$$\dot{t} = 1, \qquad \dot{r} = rH(t), \tag{2.15}$$

which both verifies that t coincides with proper time of such particles and recovers Hubble's law.

Thus, our approach has led us to work directly with $H(t)$, which is an intrinsic and measurable quantity, rather than the more usual scale factor, which we will denote by $S(t)$. Nonetheless, we can make contact with the latter simply by setting $H(t) \equiv \partial_t S(t)/S(t)$, in which case $g_1^2 = 1 - kr^2/S^2(t)$. The line-element (1.10) corresponding to the tetrad components (2.10) then reads

$$ds^2 = dt^2 - \left(1 - \frac{kr^2}{S^2(t)}\right)^{-1}[dr - rH(t)\,dt]^2 - r^2\,d\Omega^2, \tag{2.16}$$

and the dynamical equations (2.13) and (2.14) become

$$\frac{[\partial_t S(t)]^2 + k}{S^2(t)} - \tfrac{1}{3}\Lambda = \tfrac{8}{3}\pi\rho, \tag{2.17}$$

$$\frac{\partial_t^2 S(t)}{S(t)} - \tfrac{1}{3}\Lambda = -\tfrac{4}{3}\pi(\rho + 3p), \tag{2.18}$$

which we recognise as Friedmann's cosmological field equations in their standard form.

The line-element (2.16) represents the FRW spacetime expressed in terms of a 'physical' (i.e. non-comoving) radial coordinate r. We may rewrite this line-element in terms of a comoving radial coordinate $\hat{r} \equiv r/S(t)$, which yields the usual form

$$ds^2 = dt^2 - S^2(t)\left(\frac{d\hat{r}^2}{1-k\hat{r}^2} + \hat{r}^2\, d\Omega^2\right). \tag{2.19}$$

2.3 Comparison with LTB model

In contrast to our tetrad-based approach, the LTB model (Lemaître 1933; Tolman 1934; Bondi 1947) is based on the use of a *comoving* radial coordinate, which we denote by $\hat{r}$, and the assumption of a diagonal form for the metric. It is also usual to choose the time coordinate, which we denote by $\hat{t}$, to coincide with the proper time measured by observers comoving with the fluid, but for the moment we will consider the Lemaître metric (Plebański & Krasiński 2006), a slightly more general version of the LTB metric in which this requirement is not enforced. Thus, we consider a line element of the form

$$ds^2 = A^2 d\hat{t}^2 - B^2 d\hat{r}^2 - R^2 d\Omega^2, \tag{2.20}$$

where, in general, A, B and R may be arbitrary functions of both $\hat{r}$ and $\hat{t}$. Note that the LTB metric corresponds to setting $A = 1$.

We may understand the relationship between the line-element (2.20) and that given in (1.10), obtained using our tetrad-based approach, by performing a coordinate transformation that expresses the latter in terms of a comoving radial coordinate and brings it into diagonal form. We therefore consider the coordinate transformation

$$t = \hat{t}, \quad r = r(\hat{r}, \hat{t}), \quad \text{where} \quad \frac{\partial r}{\partial \hat{t}} = \frac{g_2}{f_1}. \tag{2.21}$$

Note that, although the time coordinates coincide, we still label the new one as $\hat{t}$, since the partial derivatives $\partial/\partial t$ and $\partial/\partial \hat{t}$ will, in general, be different because they hold fixed r and $\hat{r}$, respectively. One may verify that $\hat{r}$ is a comoving radial coordinate by recalling that the four-velocity components of a comoving observer in the Newtonian gauge are $[v^\mu] = (\dot{t}, \dot{r}, \dot{\theta}, \dot{\phi}) = (f_1, g_2, 0, 0)$, which transform under (2.21) into $[\hat{v}^\mu] = (\dot{\hat{t}}, \dot{\hat{r}}, \dot{\theta}, \dot{\phi}) = (f_1, 0, 0, 0)$. The physical nature of the transformation (2.21) may be further clarified by noting that

$$\frac{\partial}{\partial \hat{t}} = \frac{\partial t}{\partial \hat{t}}\frac{\partial}{\partial t} + \frac{\partial r}{\partial \hat{t}}\frac{\partial}{\partial r} = \frac{1}{f_1}\left(f_1 \frac{\partial}{\partial t} + g_2 \frac{\partial}{\partial r}\right) = \frac{1}{f_1} L_t, \tag{2.22}$$

where L_t, defined in (1.11), is the derivative with respect to the proper time of a comoving observer; indeed this is consistent with our finding above that $\dot{\hat{t}} = f_1$. Since L_t may be

considered as a relativistic form of convective derivative, one may interpret the transformation (2.21) as moving from a Eulerian to a Lagrangian description of the fluid motion. Similarly, one finds that

$$\frac{\partial}{\partial \hat{r}} = \frac{1}{g_1}\frac{\partial r}{\partial \hat{r}} L_r, \tag{2.23}$$

where L_r, also defined in (1.11), is the derivative with respect to the proper radial distance of a comoving observer.

Under the transformation (2.21) to a comoving radial coordinate, the line-element (1.10) takes the diagonal form

$$ds^2 = \frac{1}{f_1^2}\, d\hat{t}^2 - \frac{1}{g_1^2}\left(\frac{\partial r}{\partial \hat{r}}\right)^2 d\hat{r}^2 - r^2 d\Omega^2. \tag{2.24}$$

One should first note that this has been achieved without having to specify $\partial r/\partial \hat{r}$; this demonstrates that the Lemaître (and hence LTB) metric (2.20) possesses a residual gauge freedom, in contrast to the line-element (1.10) (recall that the final gauge choice made in Section 1.3 leaves the form of (1.10) unchanged).

Comparing (2.20) and (2.24), one first identifies that $r = R(\hat{r}, \hat{t})$ and hence the three non-zero tetrad components used in Section 1.3 are given by

$$f_1 = \frac{1}{A}, \qquad g_1 = \frac{1}{B}\partial_{\hat{r}} R, \qquad g_2 = \frac{1}{A}\partial_{\hat{t}} R, \tag{2.25}$$

where the final result is obtained using (2.21). The expressions for the spin-connection coefficients F and G are obtained from the relations (1.12) and read

$$F = \frac{1}{AB}\partial_{\hat{t}} B, \qquad G = \frac{1}{AB}\partial_{\hat{r}} A. \tag{2.26}$$

Substituting the expressions (2.25) and (2.26) into the dynamical and continuity equations (1.13), one then obtains

$$\partial_{\hat{r}} p = -\frac{(\rho + p)}{A}\partial_{\hat{r}} A, \tag{2.27}$$

$$\partial_{\hat{r}} M = 4\pi R^2 \rho\, \partial_{\hat{r}} R, \tag{2.28}$$

$$\partial_{\hat{t}} \rho = -(\rho + p)\left(\frac{2}{R}\partial_{\hat{t}} R + \frac{1}{B}\partial_{\hat{t}} B\right), \tag{2.29}$$

$$\partial_{\hat{t}} M = -4\pi R^2 p\, \partial_{\hat{t}} R, \tag{2.30}$$

where the expression for M in (1.14) now becomes

$$\frac{2M}{R} = \frac{1}{A^2}(\partial_{\hat{t}} R)^2 - \frac{1}{B^2}(\partial_{\hat{r}} R)^2 + 1 - \tfrac{1}{3}\Lambda R^2. \tag{2.31}$$

The assumed form (2.20) of the line-element and the system of equations (2.27)–(2.31) constitute a generalised form of the LTB model that can accommodate pressure and a non-zero cosmological constant. Nonetheless, unlike the tetrad-based approach, this model still

possesses a gauge freedom, since $\partial_{\hat{r}} R$ remains arbitrary. Thus, to determine the evolution of the system, one must first choose a form for the function $R(\hat{r}, \hat{t}_*)$ at some time $\hat{t}_*$ (usually given as an initial condition), which is not easily interpreted physically.

To make contact with the standard LTB model, we may now set $A = 1$ in the line-element (2.20), so that $\hat{t}$ coincides with the proper time measured by observers comoving with the fluid. Hence, like the Newtonian gauge, the standard LTB model employs a synchronous coordinate system. In terms of the tetrad components (2.25) and spin-connection coefficients (2.26), setting $A = 1$ corresponds to setting $f_1 = 1$ and $G = 0$, and hence (2.22) shows that the operators $\partial_{\hat{t}}$ and L_t then coincide. Thus, from the $L_t g_1$ equation in (1.12) one finds that $g_1 = g_1(\hat{r})$ is a function only of $\hat{r}$. Using the expression for g_1 in (2.25) and adopting the standard notation used in LTB models, we therefore define the function $E(\hat{r})$ by

$$1 + 2E(\hat{r}) \equiv \frac{1}{B^2}(\partial_{\hat{r}} R)^2, \tag{2.32}$$

which we may choose arbitrarily provided that $E(\hat{r}) > -\frac{1}{2}$. It is also immediately clear from (2.27) that setting $A = 1$ requires the pressure gradient to vanish. Thus, the standard LTB line-element can at best accommodate a fluid with a non-zero homogeneous pressure (note that the LTB model is by definition a solution for dust; however, as we have shown here, its line-element can accommodate non-zero homogeneous pressure). It is usual, however, to assume simply that the fluid is pressureless, in which case (2.30) shows that $M = M(\hat{r})$ is a function only of $\hat{r}$. Given our earlier interpretation of M in the tetrad-based approach, one may thus verify the usual interpretation of $M(\hat{r})$ in the LTB model as the mass-energy interior to a sphere of comoving radial coordinate $\hat{r}$ (i.e. the Misner-Sharp mass) which is naturally time-independent in the absence of pressure.

Collecting together our results, setting $A = 1$ in (2.20) and assuming a pressureless fluid thus imply that equations (2.32), (2.31) and (2.28) may be written, respectively, as

$$B^2 = \frac{(\partial_{\hat{r}} R)^2}{1 + 2E(\hat{r})}, \tag{2.33}$$

$$E(\hat{r}) = \tfrac{1}{2}(\partial_{\hat{t}} R)^2 - \frac{M(\hat{r})}{R} - \tfrac{1}{6}\Lambda R^2, \tag{2.34}$$

$$4\pi\rho = \frac{\partial_{\hat{r}} M(\hat{r})}{R^2 \partial_{\hat{r}} R}, \tag{2.35}$$

which we recognise as the standard equations for the LTB model (with the inclusion of a non-zero cosmological constant), where $M(\hat{r})$ and $E(\hat{r})$ may be chosen arbitrarily (subject to $M(\hat{r}) > 0$ and $E(\hat{r}) > -\frac{1}{2}$). Indeed, since the first equation in the set may be written as $E(\hat{r}) = \frac{1}{2}[g_1(\hat{r}) - 1]$, our approach also allows us to verify the usual interpretation of $E(\hat{r})$ as the total (non-relativistic) energy per unit rest mass of a fluid particle (i.e. after subtracting its rest

mass energy) at comoving coordinate radius $\hat{r}$. In addition to the usual set of equations (2.33)–(2.35), our approach also naturally yields the continuity equation (2.29), which originates from the contracted Bianchi identities, and in this case reduces to

$$\partial_{\hat{t}}\rho = -\left(\frac{2}{R}\partial_{\hat{t}}R + \frac{1}{\partial_{\hat{r}}R}\partial_{\hat{t}}\partial_{\hat{r}}R\right)\rho. \tag{2.36}$$

Finally, it is also worth mentioning that on integrating (2.34), it is usual to introduce another arbitrary function $t_{\rm b}(\hat{r})$, known as the "bang-time" and interpreted as a Big-Bang singularity surface at which R vanishes, i.e. $R(\hat{r}, \hat{t}_{\rm b}(\hat{r})) = 0$. From our tetrad-based approach, however, we see that this condition corresponds simply to identifying the origin $r = 0$ of our 'physical' radial coordinate.

2.3.1 Application to Schwarzschild spacetime

As an illustration of the LTB model, and in particular to compare it with the tetrad-based approach, we now apply it to the same physical situation as we considered in Section 2.2.1, namely that of a matter source concentrated into a single point and a vanishing cosmological constant. As previously, for such a solution, $\rho = p = 0$ everywhere away from the point mass, and so (2.30) implies that M = constant. Once again, the remaining system of equations is under-determined, and so some gauge-fixing is required. First we must choose a form for the arbitrary function $E(\hat{r})$. Similar to the approach adopted in Section 2.2.1, we may base our choice on some class of radially-moving test particle and, once again, the most natural choice is a radially free-falling particle released from rest at infinity. From the definition (2.32), we see that the choice of $g_1 = 1$ in our tetrad-based approach is equivalent to setting $E(\hat{r}) = 0$, which corresponds to the particle having zero energy (after subtraction of its rest mass energy).

Thus, with $M(\hat{r}) = M$ (a constant) and $E(\hat{r}) = 0$ (and $\Lambda = 0$), the LTB equation (2.34) reduces to

$$\partial_{\hat{t}}R = -\sqrt{\frac{2M}{R}}, \tag{2.37}$$

where we have taken the negative square root since the test particle is radially infalling. This equation may be immediately integrated to give $\frac{2}{3}R^{3/2} = -(2M)^{1/2}[\hat{t} - \hat{t}_b(\hat{r})]$, where the "bang-time" $\hat{t}_{\rm b}(\hat{r})$ may be an arbitrary function of $\hat{r}$, but is usually chosen such that $R(\hat{r}, \hat{t}_{\rm b}(\hat{r})) = 0$, which in this case requires $\hat{t}_{\rm b}(\hat{r}) = \hat{r}$. Thus, after this additional gauge-fixing, which was not required in the tetrad based approach, one has

$$R = \left[\frac{9M}{2}(\hat{r} - \hat{t})^2\right]^{1/3}, \qquad B = \tfrac{2}{3}\left[\frac{9M}{2(\hat{r} - \hat{t})}\right]^{1/3} \tag{2.38}$$

where the second result is derived straightforwardly from (2.33). Substituting these expressions into (2.20) with $A = 1$, one immediately obtains

$$ds^2 = d\hat{t}^2 - \tfrac{4}{9}\left[\frac{9M}{2(\hat{r}-\hat{t})}\right]^{2/3} d\hat{r}^2 - \left[\frac{9M}{2}(\hat{r}-\hat{t})^2\right]^{2/3} d\Omega^2, \tag{2.39}$$

which is the line-element for the Schwarzschild spacetime expressed in Lemaître coordinates (Lemaître 1933). This line-element is regular for all values of $\hat{r}$, except at $\hat{r} - \hat{t} = 0$, which corresponds to the location of the point mass (i.e. at $r = 0$ in terms of the 'physical' radial coordinate used in Section 2.2.1). It is straightforward to show that radially free-falling test particles released from rest at infinity have fixed values of $\hat{r}$, θ and ϕ, which therefore constitute comoving coordinates for such particles. From (2.39), one thus sees that $\hat{t}$ does indeed coincide, by construction, with the proper time of such particles.

It is interesting that, although the tetrad-based approach and the LTB model both employ synchronous time coordinates and are based on the trajectories of radially infalling particles released from rest at infinity, the two methods naturally lead to the very different line-elements (2.3) and (2.39). This occurs because of the use of a 'physical' radial coordinate in the former, whereas the latter employs a comoving radial coordinate, and also the requirement that the LTB line-element be diagonal. In our opinion, the former line-element, expressed in Painlevé–Gullstrand coordinates, is the more easily interpreted physically.

2.3.2 Application to FRW spacetime

As an second illustration of the LTB model, we now apply it to the special case of a homogeneous and isotropic spacetime, as considered in Section 2.2.2 using the tetrad-based approach. As before, this corresponds to setting ρ to be a function of $\hat{t}$ only, but for the LTB model we are limited to considering only pressureless fluids and so $p = 0$. In contrast to the tetrad-based approach, one must begin by making a gauge choice for the form for $M(\hat{r})$. This is most naturally achieved by introducing the scale factor $S(\hat{t})$ at the outset, such that $\rho(\hat{t}) = \rho_0[S_0/S(\hat{t})]^3$, where $\rho_0 \equiv \rho(\hat{t}_0)$ and $S_0 \equiv S(\hat{t}_0)$ are defined at some cosmic time $\hat{t} = \hat{t}_0$, usually taken in cosmology to be the current epoch. Keeping in mind the physical interpretation of $M(\hat{r})$, it is then simplest to assume the form $M(\hat{r}) = \frac{4}{3}\pi\rho_0 S_0^3 \hat{r}^3$. Once we have made this gauge choice, we find using (2.35) that

$$R = S(\hat{t})\hat{r}, \tag{2.40}$$

and we can then use (2.34) to determine the form of $E(\hat{r})$ to be $E(\hat{r}) = -\frac{1}{2}k\hat{r}^2$, where k is a constant.

Thus, with $M(\hat{r}) = \frac{4}{3}\pi\rho_0 S_0^3 \hat{r}^3$ and $E(\hat{r}) = -\frac{1}{2}k\hat{r}^2$, the LTB equations (2.33) and (2.35) lead straightforwardly to

$$B = \frac{S(\hat{t})}{\sqrt{1 - k\hat{r}^2}}, \tag{2.41}$$

and the corresponding line-element (2.20) (with $A = 1$) takes the usual FRW form

$$ds^2 = dt^2 - S^2(t)\left(\frac{d\hat{r}^2}{1 - k\hat{r}^2} + \hat{r}^2\, d\Omega^2\right). \tag{2.42}$$

Moreover, the remaining LTB equations (2.34) and (2.36) then yield the standard Friedmann equation and cosmological continuity equation, respectively, namely

$$\frac{[\partial_{\hat{t}} S(\hat{t})]^2 + k}{S^2(\hat{t})} - \tfrac{1}{3}\Lambda = \tfrac{8}{3}\pi\rho, \tag{2.43}$$

$$\partial_{\hat{t}}\rho = -3H(\hat{t})\rho, \tag{2.44}$$

where we have defined the Hubble parameter $H(\hat{t}) \equiv \partial_{\hat{t}} S(\hat{t})/S(\hat{t})$. These two equations can be combined to yield the standard 'acceleration' cosmological field equation for zero pressure, if desired.

Thus, we see that the LTB model has led us directly to working in terms of the scale factor, in contrast to the tetrad-based approach used in Section 2.2.2, which led naturally to the Hubble parameter, which is a directly measurable quantity. Again, this difference results from the use of a comoving radial coordinate in the LTB model and the assumption of a diagonal metric, as compared to using a 'physical' radial coordinate in the tetrad-based approach and making no such restriction on the form of the metric. Moreover, considerable gauge-fixing was required in the LTB model to obtain a definite form for the solution, whereas this was unnecessary in the tetrad-based approach.

2.4 Generalised Swiss cheese model

We now apply our tetrad-based approach to a generalised form of the Swiss cheese model. In its classic form, the Swiss cheese model consists of an exterior expanding FRW universe, albeit pressureless, in which a uniform pressureless spherical object is embedded and surrounded by a 'compensating void' that itself expands into the background and ensures that there is no net gravitational effect on the exterior universe. Such models were employed in some of the earliest attempts to describe non-linear cosmological inhomogeneities (Kantowski 1969; Rees & Sciama 1968; Dyer & Roeder 1972, 1973; Nottale 1982), since they have the advantage that analytical calculations can be performed, and compensation ensures observations in the exterior region can be modelled unambiguously. They have also been used in more recent attempts to characterise effects of inhomogeneities on cosmological observations, such as luminosity

distance and perceived dark energy (Brouzakis et al. 2007, 2008; Biswas & Notari 2008; Clifton & Zuntz 2009; Szybka 2011; Fleury 2014; Vanderveld et al. 2008; Valkenburg 2009; Flanagan et al. 2013; Lavinto et al. 2013; Lavinto & Räsänen 2015; Fleury et al. 2013). Nonetheless, the matter and velocity distributions are clearly unrealistic.

As mentioned in the Introduction, more realistic models can be constructed by working with continuous density and velocity profiles, while still restricting to spherical symmetry and ignoring pressure. Previous work using LTB models (Garcia-Bellido & Haugbølle 2008; Alonso et al. 2010) has usually ignored compensation, and this can lead to subtleties in modelling observations in the exterior region, since it is not described by a homogeneous FRW cosmology. Constructing compensated models can be difficult, however, since the initial density and velocity profiles must be carefully chosen so that streamline crossing is avoided. Otherwise, shock fronts form and one must include pressure to produce a realistic model. For example, if one perturbs just the density profile without perturbing the velocity profile, then streamline crossing is inevitable in any compensated model other than those of Swiss cheese type (where the problem would occur only in the vacuum region). Lasenby et al. (1999); Dabrowski et al. (1998) therefore present a family of continuous initial density and velocity profiles, described by polynomials in radius, that avoid the problem of streamline crossing in a very simple manner, while keeping the density profile compensated and realistic, and which are consistent with having grown from primordial fluctuations in the very early universe. The evolution of the resulting spatially-finite inhomogeneity was then determined in the absence of pressure using our tetrad-based method. We later use this model in Chapter 4 to represent a cosmic void.

In this Section, however, our primary focus is not the modelling of realistic cosmological inhomogeneities or the prediction of observational effects in the exterior region. Rather, we wish merely to extend the analysis presented in Nandra et al. (2013) (hereinafter NLH3) by applying our tetrad-based method to a generalised form of Swiss cheese model, in which we allow the fluid in the interior and exterior regions to support pressure, in general, and do not demand that the interior region be compensated. Aside from intellectual curiosity, the motivations for this study are two-fold: we first wish to verify that Birkhoff's theorem holds in the vacuum region, the usual interpretation of which has recently been brought into question for related systems (Zhang & Yi 2012); and, second, we wish, in the next Chapter, to consider the validity of the theoretical arguments that underpin the $R_\mathrm{h} = ct$ cosmological model (Melia 2007, 2009; Melia & Shevchuk 2012), which has recently received considerable attention (van Oirschot et al. 2010; Lewis & van Oirschot 2012; Mitra 2014). These investigations are presented, respectively, in Section 2.5 and Chapter 3.

As discussed in Section 1.3, instead of imposing an equation of state, $p = p(\rho)$, we solve the system of equations (1.12)–(1.14) by specify a form for $\rho(r, t)$ for all t or, equivalently, a

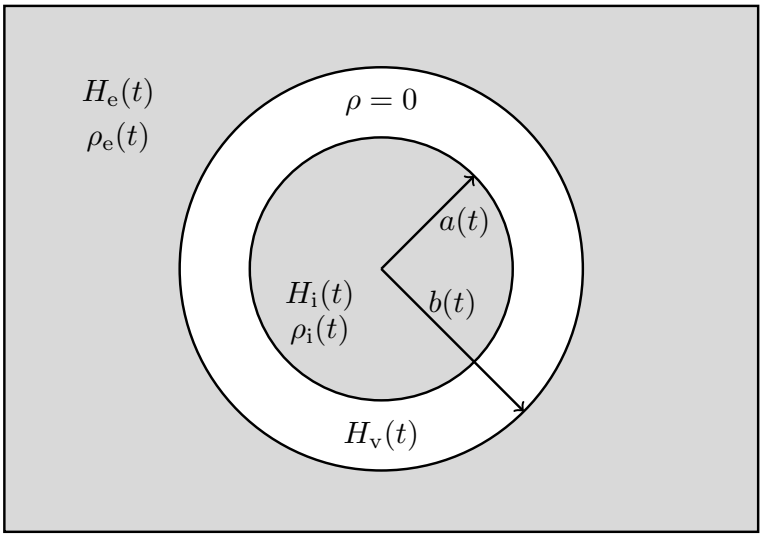

Figure 2.1: Generalised Swiss cheese model: a spherical interior region of uniform density $\rho_\mathrm{i}(t)$ and radius $a(t)$ is surrounded by a vacuum region of radius $b(t)$, which itself resides in an exterior region with uniform density $\rho_\mathrm{e}(t)$. The rates of expansion of the interior, vacuum and exterior regions are characterized by the 'Hubble parameters' $H_\mathrm{i}(t)$, $H_\mathrm{v}(t)$ and $H_\mathrm{e}(t)$, respectively. In general, the fluid can support pressure and the interior region need not be compensated.

form for $M(r,t)$ followed by use of the $L_r M$. We choose a form for $\rho(r,t)$ which is piecewise uniform in r such that we can combine the $L_t\rho$, $L_t M$ and $L_r M$ equations to obtain an ODE in r that may be solved to obtain an expression for the fluid velocity $g_2(r,t)$ and hence the rest of the system.

2.4.1 Model specification

The generalised Swiss cheese model is illustrated in Fig. 2.1 and consists of a spherical interior region of uniform density $\rho_\mathrm{i}(t)$ and radius $a(t)$ surrounded by a vacuum region of radius $b(t)$, which itself resides in an exterior region with uniform density $\rho_\mathrm{e}(t)$. The rates of expansion of the interior, vacuum and exterior regions are characterized by the 'Hubble parameters' $H_\mathrm{i}(t)$, $H_\mathrm{v}(t)$ and $H_\mathrm{e}(t)$, respectively (the definition of $H_\mathrm{v}(t)$ is discussed below). These functions are free for us to choose, and together with $M(r,t)$ and initial conditions, completely specify the evolution of the system. As we show later on, these 'Hubble parameters' are, in fact, equal to the covariant Hubble scalar in both the interior and exterior regions. In general, the interior region need not be compensated and the fluid in both the interior and exterior regions can support pressure.

From the figure, we may write down an expression for the total mass-energy $M(r,t)$

contained within a sphere of physical radius r at time t. It is clear that

$$M = \begin{cases} \frac{4}{3}\pi\rho_{\rm i}(t)r^3, & r \leq a(t), \\ \frac{4}{3}\pi\rho_{\rm i}(t)a(t)^3 \equiv M_0, & a(t) \leq r \leq b(t), \\ \frac{4}{3}\pi\rho_{\rm e}(t)r^3 + m(t), & r \geq b(t), \end{cases} \tag{2.45}$$

where M_0 is a constant and $m(t) = M_0 - \frac{4}{3}\pi\rho_{\rm e}(t)b(t)^3$ is the mass contained within $b(t)$ at time t, *in excess* of that which would be present due to the exterior background alone. For a compensated interior region, one thus has $m(t) \equiv 0$. We note that the system considered in NLH3 corresponds to setting $b(t) = a(t)$, so that there is no vacuum region.

As we will show below, in the general case where the fluid supports pressure, to determine the dynamical evolution of the system completely one must specify the internal and external Hubble parameters $H_{\rm i}(t)$ and $H_{\rm e}(t)$, together with the evolution $a(t)$ and $b(t)$ of the two boundaries (and the density $\rho_* \equiv \rho_{\rm i}(t_*)$ of the interior region at some reference time $t = t_*$). Typically, one should take $H_{\rm e}(t)$ to correspond to some expanding exterior universe of interest, but $H_{\rm i}(t)$, $a(t)$ and $b(t)$ can, in principle, have any form.[a] This follows both from the presence of the vacuum region and from allowing the relationship between the fluid pressure and density to be arbitrary, since then the interplay between pressure and gravity may allow expansion or contraction of the interior and vacuum regions at any rate. This freedom would disappear, however, if one imposed an equation of state on the fluid. In particular, in the special case of a pressureless fluid, $a(t)$ is straightforwardly determined from $H_{\rm i}(t)$ (and the radius $a_* \equiv a(t_*)$ at some reference time $t = t_*$).

We note that by leaving $H_{\rm i}(t)$ and $H_{\rm e}(t)$ free to choose, we are treating the system as being composed of a mathematical fluid, that is intended to mimic the kinematical evolution (if not the physics) of a combination of baryonic gas and dark matter, having a single effective density and a single effective pressure required for stability (for more details, see Nandra et al. (2012b)). This results in an effective 'equation' of state which depends on both r and t. Choosing the Hubble parameters and specifying the mass-energy $M(r,t)$ means that we can solve for $p(r,t)$ using the generalised Oppenheimer-Volkov equation (1.16). Hence the effective 'equation of state' is then determined. Treating the fluid as a single mathematical fluid avoids the complication of calculating the non-linear evolution of multi-fluid systems, whereby one would separate the fluid in each region into its baryonic and dark matter components.

[a] As shown by NLH3, however, in the case where $b(t) = a(t)$, so that there is no vacuum region, the evolution $a(t)$ of the single boundary between the two fluid regions cannot be set arbitrarily, but is instead determined by specifying $H_{\rm i}(t)$ and $H_{\rm e}(t)$ (together with the interior density $\rho_* \equiv \rho_{\rm i}(t_*)$ and the radius $a_* \equiv a(t_*)$ at some reference time $t = t_*$).

2.4.2 Boundary conditions

Any spatial surface at which the density is discontinuous, and which may in general be moving, will trace out a 3-dimensional (timelike) hypersurface Σ in spacetime on which the solution must satisfy the Israel junction conditions (Israel 1966, 1967). If $\hat{n}_\mu$ are the covariant components of the unit (spacelike) normal to Σ, pointing from the inside to the outside, then the Israel junction conditions require both of the induced metric $h_{\mu\nu} = g_{\mu\nu} + \hat{n}_\mu \hat{n}_\mu$ and the extrinsic curvature $K_{\alpha\beta} = h_\alpha{}^\mu h_\beta{}^\nu \nabla_\mu \hat{n}_\nu$, and the quantity $T_{\mu\nu}\hat{n}_\mu$, to agree on Σ.

For the model illustrated in Fig. 2.1, two such hypersurfaces are defined by $\Sigma(t, r) \equiv r - x(t) = 0$, where $x(t)$ can equal either $a(t)$ or $b(t)$. As discussed in Nandra et al. (2013), the components $\hat{n}_\mu$ are given by

$$[\hat{n}_\mu] = \frac{[-\partial_t x, 1, 0, 0]}{|f_1^2(\partial_t x)^2 - 2f_1 g_2 \partial_t x + g_2^2 - g_1^2|^{1/2}}, \tag{2.46}$$

where $\partial_t x \equiv dx(t)/dt$; one may readily verify that $\hat{n}_\mu \hat{n}^\mu = -1$, as required. One can show using this expression that the continuity of $T_{\mu\nu}\hat{n}_\mu$ across the boundary implies that the fluid velocity, g_2, is continuous and the equation of motion for $x(t)$ is given by $\partial_t x = g_2/f_1$.

Thus, on the hypersurface Σ, one has $dx(t)/dt = g_2/f_1$ and the expression (2.46) simplifies to

$$[\hat{n}_\mu] = \frac{1}{g_1}[-g_2/f_1, 1, 0, 0]. \tag{2.47}$$

After a long but straightforward calculation, one then finds that the only non-zero components of the extrinsic curvature of Σ are[b]

$$K_{00} = \frac{g_1}{f_1^3}\partial_r f_1, \qquad K_{11} = g_1 r, \qquad K_{22} = g_1 r \sin^2\theta. \tag{2.48}$$

Thus the continuity of the extrinsic curvature requires that f_1, g_1 and $\partial_r f_1$ are continuous there.

The above junction conditions have consequences for the continuity of other variables of interest. In particular, from the $L_r f_1$ equation in (1.12), one has $G = -(g_1/f_1)\partial_r f_1$, which must therefore also be continuous at the boundary. Moreover, the $L_r p$ equation in (1.13) and the continuity of g_1 and G imply that the pressure p is also continuous across the boundary, although its radial derivative, in general, has a step there.

Finally, we also adopt the boundary condition at large r that all physical quantities tend to those of the exterior cosmology. For spatially-flat and open universes, this corresponds to the limit $r \to \infty$, whereas for a closed universe one must instead consider the limit $x(t) \ll r < S(t)$, where $S(t)$ is the universal scale factor which also corresponds to the curvature scale for a closed

[b] The expression for K_{00} given here differs from that in Nandra et al. (2013), since the latter is incorrect owing to a sign error in the original calculation. Nonetheless, both forms lead to the same conclusion regarding the continuity of $\partial_r f_1$ at the boundary.

universe. In each case, we require the line-element (1.10) to tend at large r to the corresponding FRW line-element (2.16) with $H(t) = H_{\rm e}(t)$. Thus, for large r, one requires

$$f_1 \to 1, \qquad g_1 \to \sqrt{1 - \frac{kr^2}{S^2(t)}}, \qquad g_2 \to rH_{\rm e}(t). \tag{2.49}$$

2.4.3 Interior and exterior regions

From (2.45), one sees that the forms for M in the interior and exterior regions are the same as the model considered in NLH3, albeit with a different definition of $m(t)$. Moreover, the same boundary conditions (2.49) apply at large r. Therefore, many of the equations derived in NLH3 remain valid.

Specifically, in the interior region, the non-zero tetrad components are again given by

$$f_{1,{\rm i}} = -\frac{3H_{\rm i}(t)\,(\rho_{\rm i}(t) + p_{\rm i})}{\rho_{\rm i}'(t)}, \tag{2.50}$$

$$g_{1,{\rm i}} = \sqrt{1 + r^2\left(H_{\rm i}^2(t) - \tfrac{8}{3}\pi\rho_{\rm i}(t) - \tfrac{1}{3}\Lambda\right)}, \tag{2.51}$$

$$g_{2,{\rm i}} = rH_{\rm i}(t), \tag{2.52}$$

where, following NLH3, a prime denotes differentiation with respect to t. In order to evaluate the above expressions for $f_{1,{\rm i}}$ and $g_{1,{\rm i}}$, one requires forms for $\rho_{\rm i}(t)$ and $p_{\rm i}$. Substituting the above expression for the fluid velocity $g_{2,{\rm i}}$ and the enclosed mass $M = \frac{4\pi}{3}\rho_{\rm i}(t)r^3$ from (2.45) into the generalised Oppenheimer–Volkov equation (1.16), and integrating, will yield an (integral) expression for $p_{\rm i}$ in terms of $H_{\rm i}(t)$ and $\rho_{\rm i}(t)$, after imposing the condition that the pressure is continuous across the boundary $a(t)$ and hence vanishes there. Thus, it only remains to determine $\rho_{\rm i}(t)$, which is straightforwardly obtained for a given boundary evolution $a(t)$ by recalling that $M_0 \equiv \frac{4\pi}{3}\rho_{\rm i}(t)a^3(t)$ is a constant. In the special case of a pressureless fluid, it is worth noting that one immediately has $f_{1,{\rm i}} = 1$ and so (2.50) can be integrated to obtain $\rho_{\rm i}(t)$, which then determines $a(t)$.

For the exterior region, the non-zero tetrad elements are given by

$$f_{1,{\rm e}} = -\frac{3H_{\rm e}(t)\,(\rho_{\rm e}(t) + p_{\rm e})}{\rho_{\rm e}'(t)}, \tag{2.53}$$

$$\begin{aligned} g_{1,{\rm e}}^2 = 1 - \frac{2m(t)}{r} + \left(H_{\rm e}(t)^2 - \tfrac{8}{3}\pi\rho_{\rm e}(t) - \tfrac{1}{3}\Lambda\right)r^2 \\ + \frac{9H_{\rm e}^2(t)m'(t)}{16\pi^2\rho_{\rm e}'^2(t)r^4}\left(\tfrac{8}{3}\pi\rho_{\rm e}'(t)r^3 + m'(t)\right), \end{aligned} \tag{2.54}$$

$$g_{2,{\rm e}} = rH_{\rm e}(t) + \frac{3m'(t)H_{\rm e}(t)}{4\pi r^2\rho_{\rm e}'(t)}. \tag{2.55}$$

In order to evaluate the above expressions, one requires forms for $p_{\rm e}$, $\rho_{\rm e}(t)$ and $b(t)$. Substituting the expressions for M and $g_{2,{\rm e}}$ into the generalised Oppenheimer–Volkov equation (1.16),

integrating and imposing the condition that the pressure is continuous across the boundary $b(t)$ and hence vanishes there, will yield an (integral) expression for p_{e} in terms of $\rho_{\mathrm{e}}(t)$, $H_{\mathrm{e}}(t)$, $b(t)$ and the (in general) time-dependent uniform fluid pressure $p_\infty(t)$ at large r corresponding to the external cosmological model. One is free to specify $H_{\mathrm{e}}(t)$, $b(t)$ and $p_\infty(t)$, and the function $\rho_{\mathrm{e}}(t)$ may be determined from the following equations from NLH3 which remain valid in the exterior region:

$$\rho_{\mathrm{e}}'(t) + 3H_{\mathrm{e}}(t)\left(\rho_{\mathrm{e}}(t) + p_\infty(t)\right) = 0, \tag{2.56}$$

$$H_{\mathrm{e}}^2(t) - \tfrac{8}{3}\pi\rho_{\mathrm{e}}(t) - \tfrac{1}{3}\Lambda = -\frac{k}{R^2(t)}. \tag{2.57}$$

We recognise (2.56) and (2.57) as the standard cosmological fluid evolution equation and the Friedmann equation, respectively. Moreover, as in NLH3, these can be combined in the usual manner to yield the dynamical cosmological field equation

$$H_{\mathrm{e}}'(t) + H_{\mathrm{e}}^2(t) - \tfrac{1}{3}\Lambda = -\tfrac{4}{3}\pi(\rho_{\mathrm{e}}(t) + 3p_\infty(t)), \tag{2.58}$$

which thus provides an expression for $\rho_{\mathrm{e}}(t)$ in terms of $H_{\mathrm{e}}(t)$ and $p_\infty(t)$.

We are free to choose the boundary evolution $b(t)$, and it is most convenient to do this by defining the 'vacuum Hubble parameter' $H_{\mathrm{v}}(t)$, such that

$$g_{2,\mathrm{e}}(b(t), t) = b(t)H_{\mathrm{v}}(t). \tag{2.59}$$

Equating the above expression with (2.55) evaluated on the boundary $b(t)$, one obtains

$$\frac{b'(t)}{b(t)} = -\frac{H_{\mathrm{v}}(t)\rho_{\mathrm{e}}'(t)}{3\rho_{\mathrm{e}}(t)H_{\mathrm{e}}(t)}. \tag{2.60}$$

This then allows one to write (2.55) in the elegant form

$$g_{2,\mathrm{e}} = rH_{\mathrm{e}}(t) - \frac{b^3(t)}{r^2}\left(H_{\mathrm{e}}(t) - H_{\mathrm{v}}(t)\right). \tag{2.61}$$

In a similar manner, one may write the expression (2.54) as

$$\begin{aligned} g_{1,\mathrm{e}}^2 = 1 - \frac{2m}{r} + (H_{\mathrm{e}}^2 - \tfrac{8}{3}\pi\rho_{\mathrm{e}} - \tfrac{1}{3}\Lambda)r^2 \\ + \frac{b^3}{r}(H_{\mathrm{v}} - H_{\mathrm{e}})\left[2H_{\mathrm{e}} + \frac{b^3}{r^3}(H_{\mathrm{v}} - H_{\mathrm{e}})\right], \end{aligned} \tag{2.62}$$

where we have momentarily suppressed t-dependencies for brevity. It is worth noting that, for the special case of a pressureless fluid, one immediately has $p_{\mathrm{e}} = 0$ and $f_{1,\mathrm{e}} = 1$, so (2.60) becomes simply $b'(t)/b(t) = -H_{\mathrm{v}}(t)$.

2.4.4 Hubble scalar and shear in the interior and exterior regions

The fluid velocity covariant derivative can be split into parts with specific symmetry properties (Hawking & Ellis 1973; Ellis & van Elst 1999). The decomposition is given by (from equation (4.17) in Hawking & Ellis (1973), adapted to our metric signature)

$$\nabla_\nu v_\mu = \omega_{\mu\nu} + \sigma_{\mu\nu} + \tfrac{1}{3}\theta h_{\mu\nu} + \dot{v}_\mu v_\nu, \tag{2.63}$$

where $\omega_{\mu\nu}$ is the vorticity tensor, $\sigma_{\mu\nu}$ is the shear tensor, $h_{\mu\nu}$ is the projection tensor into the 3D subspace orthogonal to the fluid velocity, and the volume expansion scalar, θ, is defined as

$$\theta = \nabla_\mu v^\mu. \tag{2.64}$$

Hence, the Hubble scalar is defined as

$$H_s = \tfrac{1}{3}\theta. \tag{2.65}$$

The shear tensor is defined as the traceless component of the 'fully projected' part of the symmetric piece of $\nabla_\nu v_\mu$. Specifically we define

$$\theta_{\mu\nu} = h_\mu{}^\rho h_\nu{}^\tau \nabla_{(\tau} v_{\rho)}, \tag{2.66}$$

such that the shear tensor is given by

$$\sigma_{\mu\nu} = \theta_{\mu\nu} - \tfrac{1}{3} h_{\mu\nu}\theta. \tag{2.67}$$

The final quantity of interest is the relativistic 4-acceleration vector

$$\dot{v}^\mu = a^\mu = v^\nu \nabla_\nu v^\mu, \tag{2.68}$$

which represents the degree to which matter moves under forces other than those of gravity (see for example, Section 2.1 in Ellis & van Elst (1999)).

We now consider the values of these quantities in the interior and exterior regions of our spherically symmetric solutions.

Since the fluid 4-velocity components, in a (t, r, θ, ϕ) coordinate system, are given by $v^\mu = \frac{dx^\mu}{d\tau} = (f_1, g_2, 0, 0)$ (where g_2 is the fluid 3-velocity), the Hubble scalar (2.65) in terms of tetrad components is given by

$$H_s = \tfrac{1}{3}\left(\frac{\partial g_2}{\partial r} + 2\frac{g_2}{r}\right). \tag{2.69}$$

In fact, in both the interior and exterior regions, the Hubble scalar simply reduces to the interior and exterior Hubble parameters respectively, despite the 3-velocity field deviating from the Hubble flow. That this occurs in the interior region is unsurprising, since equation (2.52) shows

that the fluid 3-velocity here coincides with a pure Hubble flow, $rH_{\rm i}(t)$. In the exterior region, one again has $H_s(t) = H_e(t)$ despite the fluid 3-velocity g_2 deviating from a pure Hubble flow, $rH_{\rm e}(t)$ (see equation (2.61)). This occurs because the deviation is a function of time divided by r^2, for which the contribution to the 4-divergence $\nabla_\mu v^\mu$ vanishes.

We can construct the shear tensor using equation (2.67) above. If we denote $S = \frac{1}{3}\left(\frac{\partial g_2}{\partial r} - \frac{g_2}{r}\right)$, one can find using equation (2.67) that the eigenvalues of the shear tensor are 0 in the t direction, $2S$ in the r direction and $-S$ in the θ and ϕ directions. We note this is traceless as required for a shear tensor.

This shows a nice complementarity to what we just found for the Hubble scalar, since here the part of g_2 corresponding to the Hubble flow gives zero shear, as expected, whilst for the exterior, the deviation $-\frac{b^3(t)}{r^2}\left(H_{\rm e}(t) - H_{\rm v}(t)\right)$, as given in equation (2.61), gives us the tangential shear eigenvalue $-S$. Hence the model studied here, at least in the exterior region, is different from those studied by Nolan (2017), where the fluid is assumed to be wholly shear-free.

The fact a spherically symmetric fluid can have a Hubble scalar which is everywhere the same as the Hubble parameter at infinity (where there is just a cosmological flow), but nevertheless has non-zero shear (tending to zero at infinity), is perhaps worthy of further comment. Specifically, such a fluid would have to obey the irrotational version of one of the constraint equations which can be derived from the Ricci identity as applied to the velocity 4-vector. To discuss this briefly, we will use the notation employed in Brechet et al. (2007), which generalises the 1+3 covariant approach to fluid dynamics of Ellis & van Elst (1999) to the context of fluids with intrinsic spin, but is convenient here since it uses the same $(+,-,-,-)$ metric as the present work.

The Ricci identity from Brechet et al. (2007) is

$$2\nabla_{[\mu}\nabla_{\nu]}v_\rho = R_{[\mu\nu]\rho}{}^{\lambda}v_\lambda, \tag{2.70}$$

and by taking an antisymmetric trace-free part, employing the Einstein equations and (for current purposes) setting the spin and vorticity to zero, we can derive the equation

$$D_\lambda\sigma^\lambda_\mu - \tfrac{2}{3}D_\mu\theta = 0, \tag{2.71}$$

where D_λ is the fully projected covariant derivative, which in this case would satisfy

$$D_\mu\theta = h^\epsilon{}_\mu\nabla_\epsilon\theta. \tag{2.72}$$

Evaluating this constraint equation for the shear tensor and volume expansion scalar found above, we find that there is a non-zero entry for $\mu = r$, given (as a general function of the tetrad components) by

$$\left(D_\lambda\sigma^\lambda_\mu - \tfrac{2}{3}D_\mu\theta\right)\Big|_{\mu=r} \propto f_1^2\frac{\partial g_1}{\partial t} + f_1 g_2\frac{\partial g_1}{\partial r} + g_1 g_2\frac{\partial f_1}{\partial r}. \tag{2.73}$$

This looks as though there is a problem, but in fact the RHS here is proportional to the Einstein tensor entry G_{tr}, which due to our choice of fluid velocity vector, has to vanish (this can be confirmed independently via the explicit solutions for these quantities we have given in each region, including the external one). Thus our results for the shear and expansion factor, and in particular the fact that the expansion parameter can correspond to what one would have for a uniform Hubble flow, whilst the fluid still has non-zero shear, are fully consistent with the Ricci identity constraint on the shear divergence.

Finally, we note that the 4-acceleration $a^\mu = v^\nu \nabla_\nu v^\mu$ simply evaluates to a radial vector with magnitude G, as already discussed in Section 1.3.

2.4.5 Vacuum region

In the vacuum region, one has $\rho = p = 0$ and so $L_r M = 0$ and $L_t M = 0$, which together imply M is a constant, which we have denoted by M_0. As we found in our discussion of the Schwarzschild spacetime in Section 2.2.1, in a vacuum region the system of equations (1.12)–(1.14) reduces just to the relationships (1.12) between the tetrad and spin-connection components and the definition of $M(= M_0)$ in (1.14), from which one finds that the quantity

$$g_1^2 - g_2^2 = 1 - \frac{2M_0}{r} - \tfrac{1}{3}\Lambda r^2 \equiv \alpha(r) \tag{2.74}$$

is a function of r only. No further equations yield new information, and one thus has an underdetermined system of equations that requires additional gauge-fixing to determine an explicit solution.

This occurs because in a vacuum region one clearly cannot choose the timelike unit Lorentz frame vector at each point to coincide with the fluid four-velocity at that point. As we did for the Schwarzschild spacetime, however, one may instead choose the timelike unit frame vector to coincide with the four-velocity $\boldsymbol{u}$ of some radially-moving test particle (which need not necessarily be in free-fall), so that its components in the tetrad frame are $[\hat{u}^a] = [1, 0, 0, 0]$ and hence in the coordinate basis one has $[u^\mu] \equiv [\dot{t}, \dot{r}, \dot{\theta}, \dot{\phi}] = [f_{1,\mathrm{v}}, g_{2,\mathrm{v}}, 0, 0]$, as previously. Moreover, this ensures that our previous physical interpretations of the tetrad and spin-connection components still hold.

Unlike in the Schwarzschild spacetime, however, there is no simplest or most natural choice for the class of radially-moving test particle to use. All one requires is that the boundary conditions discussed in Section 2.4.2 hold at each boundary $a(t)$ and $b(t)$. It is most convenient to begin by choosing $g_{2,\mathrm{v}} = v(r,t)$, where v may be an arbitrary function satisfying the boundary conditions $v(a(t),t) = g_{2,\mathrm{i}}(a(t),t) = a(t)H_\mathrm{i}(t)$ and $v(b(t),t) = g_{2,\mathrm{e}}(b(t),t) = b(t)H_\mathrm{v}(t)$. Then $g_{1,\mathrm{v}}$ is easily found from (2.74) and is also continuous at both boundaries. Finally, eliminating

G between the $L_r f_1$ and $L_t g_1$ equations in (1.12) gives the general relation

$$\partial_r(f_1 g_1) + \frac{f_1^2}{g_2}\partial_t g_1 = 0, \tag{2.75}$$

and using (2.74) to substitute for g_1, one then finds

$$\partial_r\left(f_{1,\mathrm{v}}\sqrt{\alpha(r)+v^2}\right) + f_{1,\mathrm{v}}^2\frac{\partial_t v}{\sqrt{\alpha(r)+v^2}} = 0, \tag{2.76}$$

which may be straightforwardly solved for $f_{1,\mathrm{v}}$. Gathering these results together, in the vacuum region one thus has

$$\begin{aligned} g_{2,\mathrm{v}} &= v, \\ g_{1,\mathrm{v}} &= \sqrt{\alpha(r)+v^2}, \\ f_{1,\mathrm{v}} &= \left(\sqrt{\alpha(r)+v^2}\int\frac{\partial v/\partial t}{(\alpha(r)+v^2)^{3/2}}\,dr\right)^{-1}. \end{aligned} \tag{2.77}$$

Let is first consider the general case in which the fluid in the interior and exterior regions supports pressure. Suppose one specifies the form for $v(r,t_*)$ at some time t_*. One can then see from (2.76) that one also requires the profile $f_{1,\mathrm{v}}(r,t_*)$ in order to evolve v in time. Thus, both $v(r,t_*)$ and $f_{1,\mathrm{v}}(r,t_*)$ need to be specified to determine the system. One should note, however, that there is no equation determining the time evolution of $f_{1,\mathrm{v}}$; hence $f_{1,\mathrm{v}}$ is free to take any value on any time slice, provided it satisfies the boundary conditions that both f_1 and $\partial_r f_1$ are continuous at each boundary, as shown in Section 2.4.2. Then the time evolution of v is determined.

The situation is somewhat simpler for the case in which the fluid in the interior and exterior regions is pressureless, since one may take $f_1 = 1$ everywhere and at all times. Hence, if one specifies the form for $v(r,t_*)$ at some time t_*, one can use (2.76) to evolve v in time (Lasenby et al. 1999). In this case, (2.76) becomes

$$\partial_t v + v\,\partial_r v = -\frac{M_0}{r} + \tfrac{1}{3}\Lambda r, \tag{2.78}$$

which may also be derived directly by substituting the definition of M in (1.14) into $L_t M = 0$.

In either case, with or without pressure, the exact choice of the initial profile $v(r,t_*)$ or $f_{1,\mathrm{v}}$ in the vacuum region has no physical effects on, for instance, the total redshift of a photon passing through the inhomogeneity (Lasenby et al. 1999), showing that the ambiguity in these functions is a gauge freedom and hence has no physical consequences.

2.5 Birkhoff's theorem

One of our motivations for considering the generalised Swiss cheese model is to illustrate that Birkhoff's theorem holds in the vacuum region, despite having time-evolving interior and

exterior regions. Although its usual interpretation has recently been brought into question for physical systems of this type (Zhang & Yi 2012), we first demonstrate that Birkhoff's theorem does indeed hold using a traditional wholly metric-based approach, and then proceed to show that it also holds directly at the level of the tetrad components by transforming into Schwarzschild-de-Sitter form. In particular, we note that the considerations in this Section do not depend on the radial distribution of matter in the interior or exterior regions or its state of motion, provided spherical symmetry holds. We also clarify the common misconception that the exterior matter distribution has no gravitational effect on the interior of a spherically symmetric system.

2.5.1 Metric-based approach

Our aim is to show that one may perform a transformation to new coordinates $\bar{t}$ and $\bar{r}$ that brings the line-element in the vacuum region into the standard Schwarzschild–de-Sitter form

$$ds^2 = \left(1 - \tfrac{2M_0}{\bar{r}} - \tfrac{1}{3}\Lambda\bar{r}^2\right) d\bar{t}^2 - \frac{d\bar{r}^2}{\left(1 - \tfrac{2M_0}{\bar{r}} - \tfrac{1}{3}\Lambda\bar{r}^2\right)} - \bar{r}^2 d\Omega^2. \tag{2.79}$$

It is most instructive to begin by considering the general form (1.10) of the line-element given in terms of the tetrad components. Since the angular part of (1.10) already has same form as in (2.79), this suggests that one should consider a coordinate transformation of the form

$$t = t(\bar{t}, \bar{r}), \qquad r = \bar{r}, \tag{2.80}$$

which is, in some sense, complementary to the coordinate transformation (2.21) considered previously. By analogy with our earlier discussion, however, although the radial coordinates coincide, we still label the new one as $\bar{r}$, since the partial derivatives $\partial/\partial r$ and $\partial/\partial\bar{r}$ will, in general, be different.

It is straightforward to show that if the coordinate transformation (2.80) satisfies the conditions

$$\frac{\partial t}{\partial \bar{t}} = f_1 g_1, \qquad \frac{\partial t}{\partial \bar{r}} = -\frac{f_1 g_2}{g_1^2 - g_2^2}, \tag{2.81}$$

then the line-element (1.10) takes the diagonal form

$$ds^2 = (g_1^2 - g_2^2)\, d\bar{t}^2 - \frac{d\bar{r}^2}{g_1^2 - g_2^2} - \bar{r}^2\, d\Omega^2. \tag{2.82}$$

In order for such a transformation to be possible, however, one requires the derivatives (2.81) to be consistent, i.e. they must satisfy $\partial^2 t/\partial\bar{t}\,\partial\bar{r} = \partial^2 t/\partial\bar{r}\,\partial\bar{t}$. Writing

$$\begin{aligned} \frac{\partial}{\partial \bar{t}} &= \frac{\partial t}{\partial \bar{t}}\frac{\partial}{\partial t} + \frac{\partial r}{\partial \bar{t}}\frac{\partial}{\partial r} = f_1 g_1 \frac{\partial}{\partial t}, \\ \frac{\partial}{\partial \bar{r}} &= \frac{\partial t}{\partial \bar{r}}\frac{\partial}{\partial t} + \frac{\partial r}{\partial \bar{r}}\frac{\partial}{\partial r} = -\frac{f_1 g_2}{g_1^2 - g_2^2}\frac{\partial}{\partial t} + \frac{\partial}{\partial r}, \end{aligned} \tag{2.83}$$

and using the general relation (2.75), one finds that the derivatives are consistent only in the case where $g_1^2 - g_2^2$ is a function of r alone. As shown in (2.74), this requirement is satisfied in the vacuum region and, moreover, the resulting line-element (2.82) then indeed takes the Schwarzschild–de-Sitter form (2.79), hence verifying Birkhoff's theorem.

2.5.2 Tetrad-based approach

When working at the level of the metric, one is insensitive to rotations of the local Lorentz frames. Indeed, although the coordinate transformation (2.80)–(2.81) brings the line-element into the Schwarzschild-de-Sitter form (2.79) in the vacuum region, the corresponding tetrad components are *not* of the standard 'diagonal' form (2.5) (together with the Newtonian gauge condition $f_2 = 0$ and after the inclusion of obvious additional terms resulting from a non-zero cosmological constant Λ).

Indeed, since the tetrad components transform as $\bar{e}_a{}^\mu = (\partial \bar{x}^\mu / \partial x^\nu) e_a{}^\nu$ under a general coordinate transformation, it is straightforward to show that

$$\bar{f}_1 = \frac{g_1}{g_1^2 - g_2^2}, \quad \bar{f}_2 = \frac{g_2}{g_1^2 - g_2^2}, \quad \bar{g}_1 = g_1, \quad \bar{g}_2 = g_2, \tag{2.84}$$

so that the new tetrad components do not even satisfy the Newtonian gauge condition $\bar{f}_2 = 0$. Nonetheless, the tetrad components can be transformed into the standard diagonal Schwarzschild form (2.5) by performing a (temporally- and radially-dependent) rotation of the local Lorentz frames, which automatically leaves the metric unchanged. Under such a transformation, the tetrad components become $\bar{\bar{e}}_a{}^\mu = \Lambda_a{}^b \bar{e}_b{}^\mu$, where

$$[\Lambda^a{}_b] = \begin{pmatrix} \cosh\psi & -\sinh\psi & 0 & 0 \\ -\sinh\psi & \cosh\psi & 0 & 0 \\ 0 & 0 & 1 & 0 \\ 0 & 0 & 0 & 1 \end{pmatrix} \tag{2.85}$$

and ψ denotes the rapidity of the radial boost at each event. Thus, one finds

$$\begin{aligned} \bar{\bar{f}}_1 &= (g_1 \cosh\psi + g_2 \sinh\psi)/(g_1^2 - g_2^2), \\ \bar{\bar{f}}_2 &= (g_1 \sinh\psi + g_2 \cosh\psi)/(g_1^2 - g_2^2), \\ \bar{\bar{g}}_1 &= g_1 \cosh\psi + g_2 \sinh\psi, \\ \bar{\bar{g}}_2 &= g_1 \sinh\psi + g_2 \cosh\psi. \end{aligned} \tag{2.86}$$

Hence, by choosing the rapidity ψ at each event such that $g_1 \sinh\psi + g_2 \cosh\psi = 0$, one immediately ensures that $\bar{\bar{f}}_2 = \bar{\bar{g}}_2 = 0$. Since $\cosh^2\psi - \sinh^2\psi = 1$, the required rapidity is

given by $\sinh\psi = \pm g_2/\sqrt{g_1^2 - g_2^2}$. Therefore, one further obtains

$$\bar{\bar{f}}_1 = \frac{1}{\sqrt{g_1^2 - g_2^2}}, \qquad \bar{\bar{g}}_1 = \sqrt{g_1^2 - g_2^2}, \tag{2.87}$$

where $g_1^2 - g_2^2$ is given by (2.74), and thus we recover the standard diagonal form of the tetrad for the Schwarzschild solution. Finally, it is worth noting that the speed of the boost in the radial direction is given at each point by $\tanh\psi = -g_2/g_1$.

2.5.3 Comparison with previous work

The validity of Birkhoff's theorem, or at least its usual interpretation, has recently been brought into question by Zhang & Yi (2012). To be clear, Birkhoff's theorem states that there exist coordinates for which the metric in a vacuum region surrounding any spherically-symmetric matter distribution takes the standard Schwarzschild (de-Sitter) form with parameter M_0 equal to the enclosed interior mass, even when the vacuum region is itself embedded in an exterior spherically-symmetric matter distribution. Indeed, we have just verified this in the previous Section, and shown further that the theorem also holds directly at the level of the tetrad components. An immediate corollary of Birkhoff's theorem is that, if the enclosed mass $M_0 = 0$, there exist coordinates for which the metric in the vacuum region takes the standard Minkowski (de-Sitter) form.

As pointed out by Zhang & Yi (2012), however, a common misinterpretation of Birkhoff's theorem is that the gravitational field anywhere inside a spherically-symmetric matter distribution is determined only by the enclosed mass. While this is true in Newtonian gravity, it does not hold in general relativity. This point is illustrated in Zhang & Yi (2012) by considering the metric corresponding to a static thin spherical shell of mass m_s and coordinate radius $r = r_\mathrm{s}$ surrounding a spherical central object of mass m_i centered on the origin. Since some aspects of the original calculation are unclear, we briefly re-examine this scenario here, in which the cosmological constant is assumed to vanish.

Following Zhang & Yi (2012), we begin by assuming a static, diagonal line-element of the form

$$ds^2 = A(r)\,dt^2 - B(r)\,dr^2 - r^2\,d\Omega^2, \tag{2.88}$$

where the functions $A(r)$ and $B(r)$ are arbitrary (note that our definitions of A and B are swapped relative to the line-element used in Zhang & Yi (2012)). The thin spherical shell is modelled by the artifice of first considering a shell of finite thickness with mass density $\rho(r)$, supporting tangential pressure $p(r)$ but no radial pressure component. Although not discussed by Zhang & Yi (2012), it is only by assuming the shell is comprised of such a peculiar 'fluid',

with zero radial stress but non-zero compressive stress in the tangential directions, that a static system is possible. In particular, if the radial stress did not vanish, then it would be necessary to match it to zero at the boundaries with the interior and exterior vacua.

Nonetheless, proceeding with the above model, the components of the energy-momentum tensor within the shell are $[T_{\mu\nu}] = \mathrm{diag}(\rho A, 0, pr^2, pr^2 \sin^2\theta)$, and the equations of motion yield

$$\frac{dA}{dr} = \frac{2AM}{r(r-2M)}, \tag{2.89}$$

$$B = \left(1 - \frac{2M}{r}\right)^{-1}, \tag{2.90}$$

$$p = \frac{M\rho}{2(r-2M)}, \tag{2.91}$$

where $M(r) = \int_0^r 4\pi\bar{r}^2\rho(\bar{r})\,d\bar{r}$ is the total mass enclosed within coordinate radius r. In particular, in vacuum regions, where $\rho(r) = 0$ and $M(r) =$ constant, the equation (2.89) may be integrated immediately to give

$$A(r) = C\left(1 - \frac{2M}{r}\right), \tag{2.92}$$

where C is a constant. Thus, coupled with the expression (2.90) for B, one sees that the metric in vacuum regions is of Schwarzschild form, but with a time coordinate rescaled by a constant factor $\sqrt{C}$ as compared to the proper time of a stationary observer at infinity.

The constant C must be determined by applying the appropriate boundary conditions in the presence of the thin spherical shell lying between the origin and infinity. In this case, $\rho(r)$ has a δ-function at $r = r_\mathrm{s}$ (corresponding to an infinitesimally thin shell). Thus, at this radius, M has a step and equations (2.89)–(2.91) show that p has a δ-function and B and dA/dr have a step. The last condition means that A must be continuous at $r = r_\mathrm{s}$. Thus, since we require $A \to 1$ at infinity, the appropriate constant C to use in the vacuum region interior to the shell must satisfy

$$C\left(1 - \frac{2m_\mathrm{i}}{r_\mathrm{s}}\right) = 1 - \frac{2(m_\mathrm{i} + m_\mathrm{s})}{r_\mathrm{s}}, \tag{2.93}$$

and so, in this region, the line-element is

$$ds^2 = \frac{r_\mathrm{s} - 2(m_\mathrm{i}+m_\mathrm{s})}{r_\mathrm{s} - 2m_\mathrm{i}}\left(1 - \frac{2m_\mathrm{i}}{r}\right)dt^2 - \frac{dr^2}{\left(1 - \frac{2m_\mathrm{i}}{r}\right)} - r^2\,d\Omega^2. \tag{2.94}$$

The form of the line-element, in particular the rate at which clocks run, in the vacuum region interior to the shell thus depends on both the mass m_s and location r_s of the shell, i.e. the gravitational field in this region depends on the matter distribution external to it. This is unsurprising, of course, since the presence of the shell puts the interior vacuum region into a

deeper potential well with respect to infinity than would be the case without the shell. Thus, one would expect clocks to run more slowly in this region with the shell place than without it. The same is clearly true if one considers a hollow cavity by setting $m_{\rm i} = 0$, although the spacetime inside the cavity is then Minkowski rather than Schwarzschild. Clearly, these considerations do not contradict Birkhoff's theorem or its corollary, however, since one can perform a simple constant rescaling of the time coordinate to recover the Schwarzschild line-element. Nonetheless, as pointed out by Zhang & Yi (2012), it would be incorrect to perform such a rescaling, or equivalently set $C = 1$ in the interior vacuum region, while leaving the line-element outside the shell unchanged, since this would lead to an unphysical discontinuity the time coordinate, and hence $A(r)$, across the shell. It is unclear, however, whether any of the works criticised in Zhang & Yi (2012) ever advocate carrying out this erroneous procedure.

A further example of the gravitational field at some radius in a spherically-symmetric matter distribution being determined by material external to that radius is provided by the system analysed in Nandra et al. (2013). As mentioned previously, this system corresponds to setting $b(t) = a(t)$ in the generalised Swiss cheese model discussed in Section 2.4, so that there is no vacuum region. In Nandra et al. (2013), this system is analysed separately using Newtonian gravity and general relativity. The former case, the Newtonian gravitational potential in the interior region is found to be independent of the properties of the exterior region, whereas the general-relativistic calculation shows that some of the tetrad components, and hence metric elements, in the interior do depend on the properties of the exterior region, such as its density $\rho_{\rm e}(t)$ and Hubble parameter $H_{\rm e}(t)$.

To conclude, we have verified Birkhoff's theorem, namely that a vacuum region in a spherically symmetric system is described by the Schwarzschild spacetime, at both the tetrad and metric level. However, as pointed out in Zhang & Yi (2012), a common mistake is to misinterpret the theorem to mean that the gravitational field in the vacuum in a spherically symmetric distribution is only affected by the interior mass, by analogy to Newtonian gravity. This subtle point is not often pointed out in literature.

2.6 Discussion and conclusions

We have presented a comparison of our tetrad-based methodology for solving the Einstein field equations for spherically-symmetric systems with the traditional Lemaître–Tolman–Bondi (LTB) model. Although the LTB model is widely used, it has a number of limitations. In particular, in its usual form it is restricted to pressureless systems. Moreover, the LTB model is typically expressed in comoving coordinates and thus provides a Lagrangian picture of the fluid evolution that can be difficult to interpret. Perhaps most importantly, however, even in the

absence of vacuum regions the LTB metric contains a residual gauge freedom that necessitates the imposition of arbitrary initial conditions to determine the system evolution. Hence, we have for some time adopted a different, tetrad-based method for solving the Einstein field equations for spherically-symmetric systems. The advantages of the tetrad-based approach are that it can straightforwardly accommodate pressure, has no gauge ambiguities (except in vacuum regions) and is expressed in terms of a 'physical' (non-comoving) radial coordinate. As a result, unlike the LTB model, the method has an intuitive physical interpretation, and the gauge choices employed result in equations that are essentially Newtonian in form.

In comparing our tetrad-based methodology with the LTB model, we have focussed particularly on the issues of gauge ambiguity and the use of comoving versus 'physical' coordinate systems. We have also clarified the correspondences, where they exist, between the two approaches. As an illustration, we applied both methods to the classic examples of the Schwarzschild and Friedmann–Robertson–Walker (FRW) spacetimes. In the former, we demonstrate that although the tetrad-based and LTB approaches both employ synchronous time coordinates and are based on trajectories of radially-infalling particles released from rest at infinity, the two methods lead to very different results corresponding to the use of Painlevé–Gullstrand and Lemaître coordinates, respectively. For the FRW spacetime, we find that the LTB approach leads one to work directly in terms of the scale factor, whereas the tetrad-based method leads naturally to a description in terms of the Hubble parameter, which is a measurable quantity. Moreover, considerable gauge-fixing was required in the LTB model to obtain a definite solution, but this was unnecessary in the tetrad-based approach.

We have previously applied our tetrad-based method to modelling the evolution of a finite-size, compensated, spherically-symmetric object with continuous radial density and velocity profiles that is embedded in an expanding background universe, assuming zero pressure throughout (Lasenby et al. 1999; Dabrowski et al. 1998). We have also previously used the approach to obtain solutions describing a point mass residing in an expanding universe containing a cosmological fluid with pressure (Nandra et al. 2012a), and later a finite spherical region of uniform interior density embedded in a background of uniform exterior density, where the pressure may be non-zero in both regions (Nandra et al. 2013). To illustrate further the use of our tetrad-based approach, we here extended the analysis in Nandra et al. (2013) to a generalised form of 'Swiss cheese' model, which consists of an interior spherical region surrounded by a spherical shell of vacuum that is embedded in an exterior background universe. In general, we allow the fluid in the interior and exterior regions to support pressure, and we do not demand that the interior region be compensated. We find that much of the analysis in Nandra et al. (2013), including the specification of boundary conditions, can be applied with little modification, but additional care is needed in determining the solution in the vacuum region, which requires some gauge-fixing,

as might be expected.

We paid particular attention to the form of the solution in the vacuum region and verified the validity of Birkhoff's theorem, the usual interpretation of which has recently been brought in question (Zhang & Yi 2012). We also showed that the theorem holds not only at the level of the metric, but also directly in terms of the tetrad components. We compared our findings with those in Zhang & Yi (2012) and re-examined their model system of a static, thin spherical mass surrounding a central point mass positioned at the origin. In particular, we verified that the form of the line-element in the vacuum region interior to the shell depends on both the mass and location of the shell, although this is unsurprising given that the shell puts the interior vacuum region into a deeper potential well with respect to infinity than would be the case in its absence. As pointed out in Zhang & Yi (2012), Birkhoff's theorem is often used to support the common belief that in a vacuum, the gravitational field is only affected by the interior mass. We have shown explicitly that this is incorrect.

Chapter 3

$R_h = ct$ Model

3.1 Introduction

The ΛCDM model serves as the basis for the current standard model of cosmology, which provides a good fit to a wide range of cosmological observations. As pointed out by Melia (2003), however, for the best-fit ΛCDM model, the present-day Hubble distance is broadly consistent with ct_0 to within observational uncertainties, where t_0 is the current cosmic epoch. In other words, observations suggest that the universe has expanded by an amount similar to what would have occurred had the expansion rate been constant or, equivalently, that the average acceleration of the universe up to the present epoch is consistent with zero; this is despite the fact that the combination of time-dependent radiation, matter and dark-energy densities $\rho_r(t)$, $\rho_m(t)$ and $\rho_{de}(t)$ should have produced periods of deceleration and acceleration. Another way to describe this finding (Melia 2009) is that, averaged over a Hubble time, the quantity p/ρ, where $\rho = \rho_r + \rho_m + \rho_{de}$ and $p = p_r + p_m + p_{de}$, yields $\langle p/\rho \rangle = -1/3$ to within the observational uncertainties.

In the ΛCDM model, this correspondence is a peculiar coincidence, made all the more striking by the fact that, for the best-fit model, this situation should occur only once in the history of the universe. The fact that we observe this correspondence at the present epoch is therefore most intriguing. Consequently, it was proposed by Melia (2007, 2009); Melia & Shevchuk (2012) that this correspondence is not coincidental, but should be satisfied at all cosmic times t. The physical argument originally presented for this viewpoint was based on applying Birkhoff's theorem and its corollary to a spherical subregion of a homogeneous and

isotropic matter distribution, from which it was claimed that one could identify a gravitational radius $R_\mathrm{h} = 2GM/c^2$, given in terms of the Misner–Sharp mass $M = (4\pi/3)R_\mathrm{h}^3(\rho/c^2)$ (Misner & Sharp 1964). Moreover, it is easily shown that R_h coincides with the Hubble radius in a spatially-flat universe containing any single fluid component. In particular, it was claimed that Weyl's postulate, which states that the world lines of fluid particles are orthogonal to a family of spatial hypersurfaces, requires R_h, and hence the Hubble radius, to be a 'proper' distance, i.e. one that is comoving with the cosmological fluid. Imposing this condition on the usual cosmological field equations for an FRW spacetime picks out a unique solution, for which $R_\mathrm{h}(t) = ct$ at all cosmic times. This is equivalent to vanishing total active mass, $\rho + 3p = 0$, at all epochs. The resulting cosmological model, known as the '$R_\mathrm{h} = ct$' model, has received considerable attention over the last few years, since it has been claimed to be favoured over the standard ΛCDM (and its variant wCDM with $w \neq -1$) by most observational data (Melia & Maier 2013; Wei et al. 2013, 2014a,b, 2015; Melia et al. 2015).

Recent observational data have, however, led to serious criticisms of the $R_\mathrm{h} = ct$ model. For example, the model requires the deceleration parameter $q(z) = 0$ at all times, but current data from supernovae and baryon acoustic oscillations strongly disagrees with $q_0 = 0$ at high significance (Bilicki & Seikel 2012), and robust model comparison methods strongly disfavour the $R_\mathrm{h} = ct$ model (Shafer 2015). In addition, recent cosmic microwave background (CMB) data from the *Planck* satellite rule out the equivalence of the age of the universe to $1/H_0$ at greater than 99 per cent confidence, favouring $R_\mathrm{h} = (1.05 \pm 0.02)\,ct$ at the current epoch (van Oirschot et al. 2015), which undermines a major motivation for the $R_\mathrm{h} = ct$ model; note that this result is equivalent to $q_0 = 0.05 \pm 0.02$ (van Oirschot et al. 2015). Finally, as we show below, in the spatially-flat $\Lambda = 0$ FRW spacetime assumed in the $R_\mathrm{h} = ct$ model, the comoving Hubble radius is constant in time. This contradicts the basic picture of perturbation generation and evolution according to inflationary cosmological models, in which the comoving Hubble radius decreases during inflation and then increases again afterwards. This enables the generation of 'superhorizon' modes that later re-enter the Hubble radius coherently as it grows. This leads in turn to the characteristic acoustic peak structure observed in the power spectrum of CMB anisotropies and to baryon acoustic oscillations; these well-established phenomena would be very difficult to explain if the comoving Hubble radius were constant.

In addition to objections based on observations, the validity of the theoretical argument underlying the $R_\mathrm{h} = ct$ model has also been criticised by a number of authors (van Oirschot et al. 2010; Lewis & van Oirschot 2012; Mitra 2014), and in particular the validity of the effective equation-of-state parameter $w = -1/3$ (Lewis 2013). These and other criticisms are claimed to have been addressed by Bikwa et al. (2012) and Melia (2012) (see also Melia (2015) and references therein), but the original physical arguments for the model given in Melia (2007,

2009); Melia & Shevchuk (2012) are sufficiently imponderable that it is difficult to draw definite conclusions.

In a recent paper (Melia 2016), however, Melia presents a much more explicit argument for the zero active mass condition $\rho + 3p = 0$, which he claims is a requirement of the symmetries of the FRW spacetime. In particular, it is claimed that assuming the general, spherically symmetric (but radially varying) metric, solving the Einstein field equations, and then imposing homogeneity and isotropy yields an extra condition, namely vanishing active mass, which is lost if one adopts the usual procedure of first imposing the conditions of homogeneity and isotropy on the metric and then solving the Einstein equations.

Having examined spherically-symmetric solutions in general relativity in the previous Chapter, including cosmological solutions, we take the opportunity in this Chapter to re-evaluate the theoretical arguments originally used to arrive at the $R_\mathrm{h} = ct$ model. We discuss the $R_\mathrm{h} = ct$ cosmology in Section 3.2 and describe the generic evolution of a number of cosmological 'horizons' in Section 3.3. This investigation allows us to reconsider critically the original theoretical arguments underlying the so-called $R_\mathrm{h} = ct$ cosmological model (Melia & Shevchuk 2012), which has recently received considerable attention. These considerations in turn elucidate the behaviour of a number of 'horizons' during the general-relativistic evolution of a spherically-symmetric self-gravitating matter distribution, which does not appear to have been widely discussed in the literature. Next, in Sections 3.4 and 3.5, we discuss Melia's theoretical argument for the zero active mass condition required by the $R_\mathrm{h} = ct$ model.

3.2 $R_\mathrm{h} = ct$ cosmology

In Melia (2007, 2009); Melia & Shevchuk (2012), one is first invited to imagine precisely the system illustrated in Figure 2.1, namely the generalised Swiss cheese model, with an observer located at the origin and assuming $\Lambda = 0$. By appealing to Birkhoff's theorem and its corollary, it is then pointed out correctly that the metric in the vacuum region may be written in the standard Schwarzschild form. It is further claimed, however, that the matter distribution in the exterior region therefore has no dynamical influence on the region contained within it. As outlined in Section 2.5.3, this does not necessarily hold in general relativity.

Nonetheless, this issue is not relevant to Melia's subsequent argument, since it later transpires that his appeal to Birkhoff's theorem is merely to justify that, in a standard homogeneous and isotropic cosmological model, one may determine the motion of a fluid particle at some coordinate radius r relative to an arbitrary origin by ignoring the gravitational effect of the fluid lying outside that radius, which does hold in this particular case. Thus, the scenario Melia considers is the standard homogeneous and isotropic cosmological model, and not the

generalised Swiss cheese model illustrated in Figure 2.1 that we are first invited to imagine. Indeed, it is clear that the latter is not a viable cosmological model in general. Aside from being inhomogeneous overall, the requirement that the pressure be continuous across the boundaries means that, even if one assumes that each non-vacuum region is homogeneous (i.e. with uniform density and pressure), they cannot be matched on the vacuum region unless the pressure vanishes everywhere; thus one could consider only dust models of this type.

Melia's main proposal begins with the introduction of the 'gravitational radius' $R_\mathrm{h}(t)$, which is defined by the requirement that

$$\frac{2M(R_\mathrm{h}(t),t)}{R_\mathrm{h}(t)} \equiv 1, \tag{3.1}$$

where, as previously, we adopt natural units $c = G = 1$ and $M(r,t) = \frac{4}{3}\pi\rho(t)r^3$ is the mass-energy contained with a sphere of physical radius r at time t. Indeed, substituting this form for $M(r,t)$ into (3.1), one immediately finds that $1/R_\mathrm{h}^2(t) = \frac{8}{3}\pi\rho(t)$. The key point in Melia's argument is the assertion that, in order to satisfy Weyl's postulate, the comoving gravitational radius $\hat{r}_\mathrm{h}(t) \equiv R_\mathrm{H}(t)/S(t)$ should be *independent* of t, where $S(t)$ is the scale factor defined in Section 2.2.2. In other words, each fluid particle has a *fixed* value of $\hat{r}_\mathrm{h}$.

Then, following Melia's assumption that $k = 0 = \Lambda$, the standard Friedmann equation (2.13) immediately allows one to make the identification $R_\mathrm{h}(t) = 1/H(t)$, which is the Hubble radius. Since $H(t) = \partial_t S(t)/S(t)$, the comoving gravitational (Hubble) radius in this case is given by

$$\hat{r}_\mathrm{h}(t) = \frac{1}{H(t)S(t)} = \frac{1}{\partial_t S(t)}. \tag{3.2}$$

The requirement that $\hat{r}_\mathrm{h}(t)$ is constant therefore implies $S(t) \propto t$ and so $R_\mathrm{h}(t) = 1/H(t) = t$ or, on momentarily abandoning natural units, one obtains the eponymous $R_\mathrm{h}(t) = ct$. It is worth noting that substituting $H(t) = 1/t$ into the dynamical cosmological field equation (2.14) yields Melia's so-called 'zero active mass' condition $\rho + 3p = 0$, which is equivalent to demanding that the overall cosmological fluid has the equation-of-state parameter $w = -\frac{1}{3}$ at all epochs.

The argument given in Melia & Shevchuk (2012) for supposing that $\hat{r}_\mathrm{H}(t) =$ constant is that, according to Weyl's postulate, any proper distance in an FRW spacetime must be the product of the scale factor $S(t)$ and some fixed co-moving radial coordinate, and that the definition of $R_\mathrm{h}(t)$ as a gravitational radius in (3.1) implies that it must be a proper distance. No real justification is given for this latter assertion. Indeed, we show in Section 3.3 below that the definition (3.1) does *not*, in fact, imply that $R_\mathrm{h}(t)$ is a proper distance and hence one does *not* require $\hat{r}_\mathrm{h}(t) =$ constant. Nonetheless, in trying to understand the motivation for Melia's original assertion, it is worth noting that such a conclusion might be reached from the following *erroneous* line of reasoning, which, although not articulated as such in Melia & Shevchuk (2012), has some resonances with the discussion given there.

Table 3.1: Evolution of the comoving radius $a(t)$, its velocity $\dot{a}(t)$, the mass-energy $M(t)$ enclosed within $a(t)$, the Schwarzschild radius (or radii) $R_{\rm S}(t)$ defined in (3.3) and the Hubble radius $R_{\rm H}(t) \equiv 1/H(t)$ for a selection of analytical spatially-flat ($k = 0$) expanding cosmological models, with cosmological constant Λ and fluid equation-of-state parameter w, whose evolution is determined by the Hubble parameter $H(t)$. The values of w considered correspond to dust ($w = 0$), radiation ($w = \frac{1}{3}$) and Melia's zero-active-mass condition ($w = -\frac{1}{3}$). Note that, for $\Lambda \neq 0$, the two positive solutions for $R_{\rm S}(t)$ are valid only if $1 - 9M^2(t)\sqrt{\Lambda} > 0$; otherwise there is no positive solution.

	$\Lambda = 0$			$\Lambda \neq 0$	
	$w = 0$	$w = \frac{1}{3}$	$w = -\frac{1}{3}$	$w = 0$	$w = \frac{1}{3}$
$H(t)$	$\frac{2}{3}t^{-1}$	$\frac{1}{2}t^{-1}$	t^{-1}	$\sqrt{\frac{\Lambda}{3}}\coth\left(\frac{\sqrt{3\Lambda}}{2}t\right)$	$\sqrt{\frac{\Lambda}{3}}\coth\left(\frac{2\sqrt{\Lambda}}{3}t\right)$
$a(t)$	$2M_0^{1/3}t^{2/3}$	$2M_0^{1/3}t^{1/2}$	$2M_0^{1/3}t$	$2M_0^{1/3}\sinh^{2/3}\left(\frac{\sqrt{3\Lambda}}{2}t\right)$	$2M_0^{1/3}\sinh^{1/2}\left(\frac{2\sqrt{\Lambda}}{3}t\right)$
$\dot{a}(t)$	$\frac{4}{3}M_0^{1/3}t^{-1/3}$	$M_0^{1/3}t^{-1/2}$	$2M_0^{1/3}$	$2\sqrt{\frac{\Lambda}{3}}M_0^{1/3}\frac{\cosh\left(\frac{\sqrt{3\Lambda}}{2}t\right)}{\sinh^{1/3}\left(\frac{\sqrt{3\Lambda}}{2}t\right)}$	$2\sqrt{\frac{\Lambda}{3}}M_0^{1/3}\frac{\cosh\left(\frac{2\sqrt{\Lambda}}{3}t\right)}{\sinh^{1/2}\left(\frac{2\sqrt{\Lambda}}{3}t\right)}$
$M(t)$	$\frac{16}{9}M_0$	$M_0t^{-1/2}$	$4M_0t$	$\frac{4}{3}M_0\Lambda$	$\frac{4M_0\Lambda}{3\sinh^{1/2}\left(\frac{2\sqrt{\Lambda}}{3}t\right)}$
$R_{\rm S}(t)$	$\frac{32}{9}M_0$	$2M_0t^{-1/2}$	$8M_0t$	$\frac{2}{\sqrt{\Lambda}}\cos\left[\frac{\pi}{3} \pm \frac{1}{3}\tan^{-1}\left(-\frac{\sqrt{1-9M^2(t)\Lambda}}{3M(t)\sqrt{\Lambda}}\right)\right]$	$\frac{2}{\sqrt{\Lambda}}\cos\left[\frac{\pi}{3} \pm \frac{1}{3}\tan^{-1}\left(-\frac{\sqrt{1-9M^2(t)\Lambda}}{3M(t)\sqrt{\Lambda}}\right)\right]$
$R_{\rm H}(t)$	$\frac{3}{2}t$	$2t$	t	$1/H(t)$	$1/H(t)$

In a homogeneous and isotropic model, consider a fluid particle located at a distance $R_\mathrm{h}(t_*)$ from an arbitrary origin at some cosmic time $t = t_*$. The definition (3.1) implies that $R_\mathrm{h}(t_*)$ is equal to the Schwarzschild radius of the mass of fluid contained with the radius $R_\mathrm{h}(t_*)$. Invoking (the corollary of) Birkhoff's theorem, the fluid external to this radius has no gravitational effect on the motion of the particle. Thus, as the universe evolves, one might suspect that it is impossible for the fluid particle to move to a radius larger than $R_\mathrm{h}(t_*)$, since to do so would require it to escape the Schwarzschild horizon. Conversely, if the particle were to move to a radius smaller than $R_\mathrm{h}(t_*)$, then the original mass of fluid would be wholly contained within its Schwarzschild radius. Invoking (the corollary of) Birkhoff's theorem once again, one might suspect that the fluid would therefore inevitably undergo gravitational collapse. To avoid these two scenarios, one could thus be led to suppose that $R_\mathrm{h}(t) \propto S(t)$ and hence $\hat{r}_\mathrm{h}(t) = \text{constant}$.

In the next Section, we show that the requirement $\hat{r}_\mathrm{h}(t) = \text{constant}$ does *not* follow from the definition (3.1) and that the two scenarios outlined above are not a cause for concern. In doing so, our investigations below also elucidate the behaviour of a number of 'horizons' during the general-relativistic evolution of a spherically-symmetric self-gravitating matter distribution; although straightforward and interesting, this behaviour does not appear to have been widely discussed in the literature.

3.3 Evolution of horizons

In a homogeneous and isotropic cosmological model, let us consider an imaginary spherical boundary of radius $a(t)$ that is comoving with the fluid and centred on some arbitrary origin. From the discussion in Section 2.4, the equation of motion for $a(t)$ is $L_t a(t) = \dot{a} = H(t)a(t)$ (since $f_1 = 1$ in this case), where $H(t)$ is the Hubble parameter characterising the evolution of the fluid. If $M(t)$ denotes the mass-energy contained within this sphere, we define the corresponding Schwarzschild radius $R_\mathrm{S}(t)$ as the solution of

$$1 - \frac{2M(t)}{R_\mathrm{S}(t)} - \tfrac{1}{3}\Lambda R_\mathrm{S}^2(t) \equiv 0, \tag{3.3}$$

which clearly reduces to $R_\mathrm{S}(t) \equiv 2M(t)$ if $\Lambda = 0$. We also define the Hubble radius $R_\mathrm{H}(t) \equiv 1/H(t)$; note that this coincides with Melia's gravitational radius $R_\mathrm{h}(t)$ in the case $k = 0 = \Lambda$, but differs from it in more general cosmological models (although such models were not considered by Melia).

We now consider the behaviour of $a(t)$, $R_\mathrm{S}(t)$ and $R_\mathrm{H}(t)$ for a selection of analytical spatially-flat ($k = 0$) expanding cosmological models, with cosmological constant Λ and fluid equation-of-state parameter w, whose evolution is determined by the Hubble parameter $H(t)$. We note that, in the spatially-flat ($k = 0$) case, $a(t)$ is the proper distance from the origin to

the spherical boundary under consideration, and that $\dot{a}$ is its rate of change with respect to the proper time of an observer comoving with the fluid.[a] The results are presented in Table 3.1. The values of w considered correspond to dust ($w = 0$), radiation ($w = \frac{1}{3}$) and Melia's zero-active-mass condition ($w = -\frac{1}{3}$). It is worth noting that it is only in the case $w = 0$ that the mass-energy $M(t)$ contained within the comoving radius $a(t)$ is constant; for other values of w the presence of non-zero pressure means that the fluid does work and hence $M(t)$ changes with time.

For $\Lambda = 0$, the behaviour of the quantities listed in the table is shown in Figure 3.1. For both the dust and radiation cases, one sees that $a(t)$, $R_{\mathrm{S}}(t)$ and $R_{\mathrm{H}}(t)$ cross at a single point that we denote by $t = t_*$, which coincides with $\dot{a}(t)$ dropping to 1 (or c in standard units). This behaviour is quite general and holds for any positive value of the parameter M_0 in Table 3.1. Thus, the comoving radius $a(t)$ initially lies outside the Hubble radius. Indeed, one may consider that $\dot{a}$ is allowed to be greater than c during this initial period due to the 'superhorizon' (or, more correctly, super-Hubble-radius) nature of $a(t)$. Note that from the Friedmann equation, we know that

$$\frac{1}{R_{\mathrm{H}}^2(t)} \equiv H^2(t) = \frac{8\pi\rho}{3} + \frac{\Lambda}{3}, \tag{3.4}$$

where we consider the general case with $\Lambda \neq 0$. Multiplying the above by a^2 gives us

$$\dot{a}^2 = \frac{2M}{a} + \frac{\Lambda a^2}{3}. \tag{3.5}$$

Hence we see that when $\dot{a} = 1$, $a = R_{\mathrm{H}}$ and also $a = R_{\mathrm{S}}$. This is precisely what we see in Figure 3.1. $a(t)$ enters the Hubble radius $R_{\mathrm{H}}(t)$ at precisely the same moment as it exits the Schwarzschild radius $R_{\mathrm{S}}(t)$; it is allowed to do the latter, since the fluid at the boundary is moving at speed c at this instant. Thus, one has two 'horizon crossings' taking place simultaneously and in opposite directions, which is not usually pointed out in the literature. Moreover, one sees that there is no reason for the Hubble radius to be comoving, which contradicts the central assumption of the $R_{\mathrm{h}} = ct$ model. It is also worth noting that in the case of dust, for which the pressure vanishes everywhere, one can consistently 'cut-off' the fluid at the boundary $a(t)$, and thereby consider a finite fluid ball surrounded by vacuum; the results for this case are precisely those given above.

In fact, we can consider the case with a finite, pressureless ball in order to verify that the physics is correct. Consider a sphere of radius $a(t)$ filled with dust, embedded in a vacuum.

[a] We further note that the proper distance is measurable in principle (albeit in a highly impractical manner!), by arranging for a 'cosmic conspiracy' in which comoving observers (who may identify themselves as such by the absence of a CMB dipole) along a radial line from $r = 0$ to $r = a$ lay down rulers at the same instant of their proper time t (which may be determined, for example, by requiring the CMB temperature they measure to have a particular value). Moreover, by arranging for such a conspiracy to be repeated at a later time $t + dt$, the 'velocity' $\dot{a}$ can be determined. Note, however, that when a is bigger than the current particle horizon, it would not be possible to arrange for such a conspiracy.

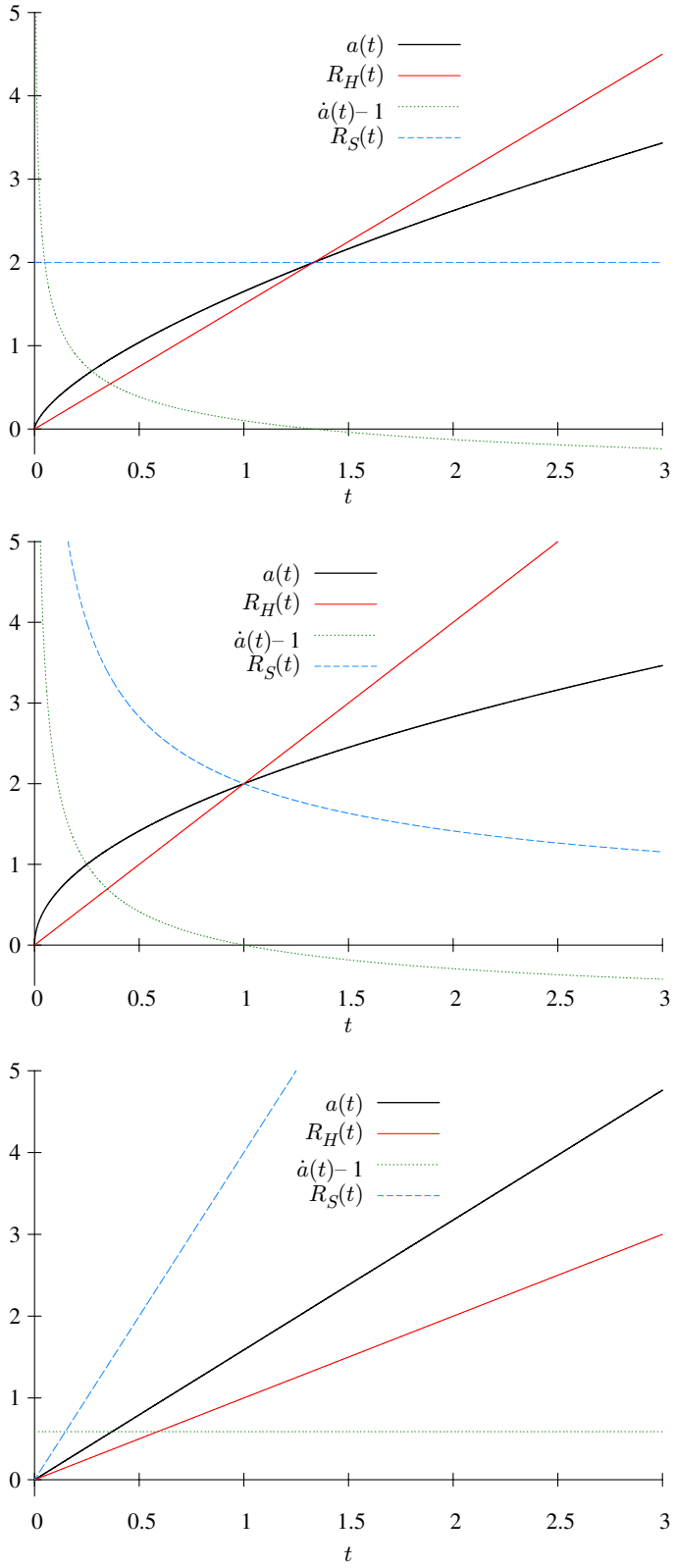

Figure 3.1: Behaviour of quantities listed in Table 3.1 for the case $\Lambda = 0$. Top: dust ($w = 0$ with $M_0 = \frac{9}{16}$), middle: radiation ($w = \frac{1}{3}$ with $M_0 = 1$), bottom: zero active mass ($w = -\frac{1}{3}$ with $M_0 = \frac{1}{2}$).

Its evolution must still follow that described in figure 3.1, such that it expands with time and eventually crosses R_S. Hence it is the time reversed equivalent of a collapsing ball of dust. In the latter case, the physical event horizon exists only once the boundary of the sphere crosses the point $r = 2M(t)$ (for the $\Lambda = 0$ case). Therefore, we can view the expanding sphere as a white hole, which has a horizon at R_S, where objects are only allowed to move out initially. Once the boundary of the sphere crosses the horizon, the physical characteristics of the horizon cease to exist, such that it becomes physically possible for objects to fall in through the horizon. It is noteworthy that in the case of a collapsing ball of dust, the region interior of the event horizon is a trapped surface, whereas in the case of a white hole, the region outside the horizon is an anti-trapped surface where light cones in the exterior region point outwards (d'Inverno 1992). To verify that the crossing of the fluid boundary over R_S is possible, we can calculate the speed at which a hypothetical observer on R_S would move as measured by a comoving observer on the boundary of the sphere, as it crosses R_S. One can show that the observed speed is given by $-g_2 + \frac{dR_S(t)}{dt}$, which is valid for any Λ and equation of state. As discussed above, when the crossing occurs, the fluid moves at speed c; hence the comoving observer sees R_S move at the speed of light when he/she crosses it, for the dust case. This is not problematic, as it is impossible to have an observer hover at R_S up until the point in time at which the ball crosses the horizon. In addition, the horizon vanishes when the edge of the fluid crosses it; hence the fluid is able to cross the horizon.

Note that when we have non-zero pressure, we can no longer 'cut-off' the fluid at the boundary $a(t)$; hence we cannot consider a case where the various lines have physical characteristics.

The bottom panel in Figure 3.1 shows the behaviour for the case $w = -\frac{1}{3}$, which corresponds to the zero active mass condition required by the $R_h = ct$ model. Clearly, in this case, the radii $a(t)$, $R_S(t)$ and $R_H(t)$ all depend linearly on t. If one chooses $M_0 = \frac{1}{8}$, then one obtains the special case in which $a(t) = R_S(t) = R_H(t)$ and $\dot{a}(t) = 1$ at all times. When $M_0 > \frac{1}{8}$, one has $\dot{a}(t) > 1$ and $a(t)$ lies inside the Schwarzschild radius and outside the Hubble radius at all times (this is illustrated in Figure 3.1, for which $M_0 = \frac{1}{2}$). Conversely, if $M_0 < \frac{1}{8}$, one has $\dot{a}(t) < 1$ and $a(t)$ lies outside the Schwarzschild radius and inside the Hubble radius for all t.

The behaviour of the quantities listed in Table 3.1 for $\Lambda \neq 0$ are illustrated in Figure 3.2. In both cases, the values of M_0 and Λ have been chosen so that, at least for some values of t, the condition $1 - 9M^2(t)\sqrt{\Lambda} > 0$ is satisfied and hence there exist two positive solutions for $R_S(t)$, which correspond to the Schwarzschild radius and the de Sitter radius, respectively.

In the case of dust (top panel), the mass-energy $M(t)$ enclosed within the spherical boundary $a(t)$ is constant, as expected, and thus so too are the two solutions for $R_S(t)$. One again sees that each solution for $R_S(t)$ intersects with $a(t)$ and $R_H(t)$ at a single point, and that at both these intersections one has $\dot{a}(t) = 1$, as we expect from equation (3.5). Thus, as in the case

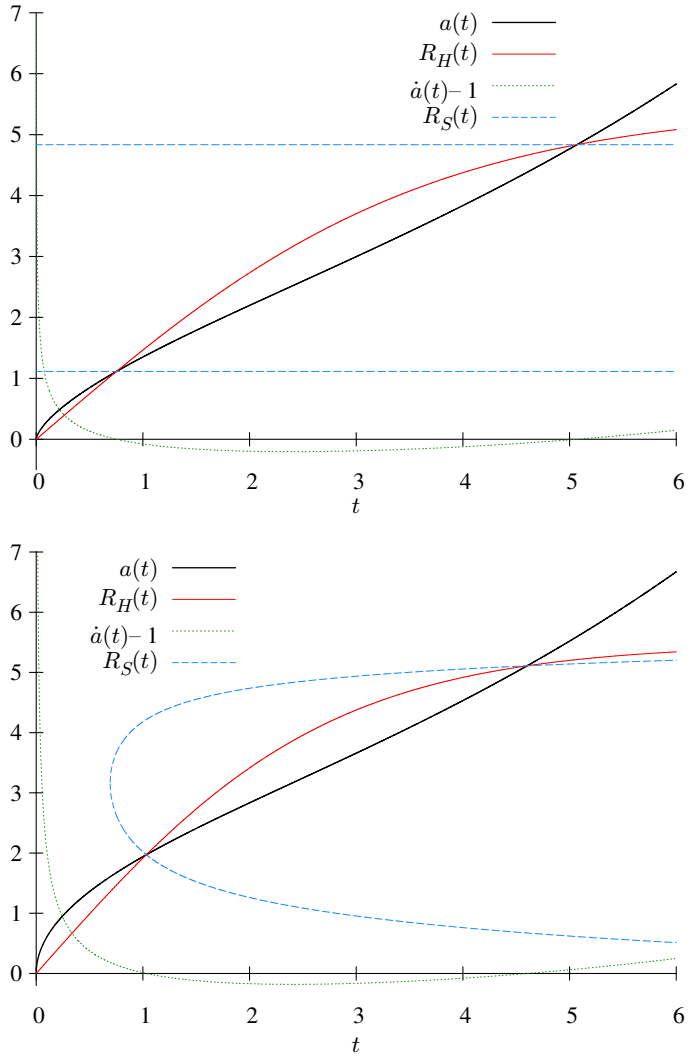

Figure 3.2: Behaviour of quantities listed in Table 3.1 for the case $\Lambda \neq 0$. Top: dust ($w = 0$), bottom: radiation ($w = \frac{1}{3}$); in both cases $M_0 = 4$ and $\Lambda = 0.1$.

$\Lambda = 0$, the comoving radius $a(t)$ initially lies outside the Hubble radius and enters it at precisely the same moment as it exits the Schwarzschild radius, at which point the fluid at the boundary $a(t)$ is moving at speed c. In the presence of non-zero Λ, however, the boundary $a(t)$ later exits the Hubble radius again, at precisely the same moment that it enters the de Sitter radius, at which point the fluid at the boundary is again moving with speed c. It is again worth noting in this dust case that the absence of pressure allows one consistently to 'cut-off' the fluid at the boundary $a(t)$, and thereby consider a finite fluid ball surrounded by vacuum with $\Lambda \neq 0$, and obtain identical results. In this case we again have a white hole, with a physical horizon at the Schwarzschild radius inside which objects are swept in, which ceases to exist at the moment in

time the edge of the fluid crosses it.

The same generic behaviour to that outlined above is also seen for radiation in the bottom panel of Figure 3.2. In this case, however, the non-zero pressure means that the fluid does work as it expands and so the mass-energy $M(t)$ contained within $a(t)$ decreases with time. Consequently, one initially has $1 - 9M^2(t)\sqrt{\Lambda} < 0$ and hence no positive solution for $R_S(t)$. As $M(t)$ decreases, however, one eventually has $1 - 9M^2(t)\sqrt{\Lambda} > 0$ and so obtains two positive solutions for $R_S(t)$, which again correspond to the Schwarzschild and de Sitter radii, respectively.

3.4 FRW metric and zero active mass

We now move on to discuss the arguments that Melia outlines in Melia (2016), where he presents a much more explicit argument for the zero active mass condition $\rho + 3p = 0$, which he claims is a requirement of the symmetries of the FRW spacetime.

Melia starts with the general spherically symmetric metric in a comoving coordinate system, which we denote by

$$ds^2 = A^2 dt^2 - B^2 dr^2 - R^2 d\Omega^2, \tag{3.6}$$

where A, B and R are in general functions of both r and t, and first considers the general case, where homogeneity is *not* assumed. Using the Einstein equations, assuming zero cosmological constant, one may derive the Euler and continuity equations

$$\frac{\partial p}{\partial r} = -\frac{1}{A}\frac{\partial A}{\partial r}(\rho + p), \tag{3.7}$$

$$\dot{\rho} = -(\rho + p)\left(2\frac{\dot{R}}{R} + \frac{\dot{B}}{B}\right), \tag{3.8}$$

where a dot denotes differentiation with respect to t. Incidentally, in his equation (13), Melia gives an incorrect form of the continuity equation, $\dot{\rho} = -3(\rho + p)(\dot{R}/R)$, which is valid only in the homogeneous case, but this error has no bearing on the rest of his argument.

Melia then imposes homogeneity and finds from equation (3.7) that A is independent of r, such that $A = A(t)$. Moreover, as usual, one may also write $B(r,t) = a(t)/\sqrt{1 - kr^2}$ and $R(r,t) = a(t)r$, where $a(t)$ is the scale factor and k is the spatial curvature constant. The Einstein equations then yield the corresponding Friedmann equation and acceleration equation,

$$\left(\frac{\dot{a}}{a}\right)^2 = \frac{8\pi}{3}\rho A^2 - \frac{k}{a^2}A^2, \tag{3.9}$$

$$\frac{\ddot{a}}{a} - \frac{\dot{a}}{a}\frac{d\ln A}{dt} = -\frac{4\pi}{3}A^2(\rho + 3p), \tag{3.10}$$

which Melia combines into the single equation

$$\frac{d}{dt}\left[\ln\left(\frac{\dot{a}^2}{A^2}\right)\right] = -\left(\frac{k}{a\dot{a}}A^2 + \frac{\dot{a}}{a}\right)\left(1 + \frac{3p}{\rho}\right). \tag{3.11}$$

Melia then writes $A(t)$ in the following form

$$A^2(t) = h\dot{a}^2 e^{I(t)}, \tag{3.12}$$

where h is a constant and $I(t)$ is a function defined by the above equation. Substituting (3.12) into the LHS of (3.11) and using (3.9), then gives

$$\frac{dI(t)}{dt} = \frac{8\pi}{3}\frac{a}{\dot{a}}A^2\left(\rho + 3p\right). \tag{3.13}$$

The flaw in his logic then lies in the following. He asserts that, in order for A to be a constant, as it is in the FRW metric, equation (3.12) requires *both* $\dot{a}^2$ and $e^{I(t)}$ to be constant in time. This *incorrect* assertion then leads one to conclude that $dI(t)/dt = 0$ at all times, and that by equation (3.13), $\rho + 3p = 0$ at all times. He therefore concludes that the FRW metric (for which $A = 1$) requires the zero active mass condition to be satisfied. This assumption is clearly wrong, however, as the RHS of equation (3.12) can be constant without $\dot{a}^2$ and $e^{I(t)}$ both being constant.

That equations (3.12) and (3.13) can be satisfied for $A =$ constant and $\rho + 3p \neq 0$ is easily illustrated by a simple example. Let us consider the conventional FRW metric, for which $A = 1$, and specifically the Einstein-de-Sitter (EdS) model (which Melia himself uses as an example to support his theory), for which $a(t) \propto t^{2/3}$, $\rho(t) = 1/(6\pi t^2)$ and $p(t) = 0$. We can use these expressions to evaluate the RHS of equation (3.13) and integrate to find that $e^{I(t)} \propto t^{2/3}$. Since $\dot{a} \propto t^{-1/3}$, the powers of t cancel out on the RHS of (3.12), showing that A is a constant, as required. It is worth noting that in the above analysis, we have *not* simply imposed $A = 1$ *a priori*, as in the usual procedure for deriving the cosmological field equations, but instead demonstrated that equations (3.12) and (3.13), derived by solving the Einstein equations for the general spherically-symmetric metric (3.6), admit solutions for which A is constant and $\rho + 3p \neq 0$. This counter-example alone thus disproves Melia's central claim.

It is worth making a few further points regarding his argument for zero active mass before moving on to the next part of his argument. First, the expression (3.13) that Melia presents is strange in that it contains A, which one may eliminate in favour of $I(t)$ using (3.12). In fact, one can derive the following two expressions for $I(t)$,

$$e^{I(t)} = \frac{3}{h(8\pi\rho a^2 - 3k)}, \tag{3.14}$$

$$e^{-I(t)} = -\frac{8\pi}{3}h\int_0^t a\dot{a}(\rho + 3p)\,dt', \tag{3.15}$$

which make no explicit reference to A. Given forms for ρ and a as functions of t, we can use either of these equations to compute $I(t)$, and then by using equation (3.12) can find the $A(t)$ implied. We adopt this route in the example studied in the next Section. Alternatively, one

could start from a fixed form of A, and work forwards from there. For example, if $A = 1$, then (3.9) and (3.10) reduce to the conventional cosmological field equations, and for any solution of them (i.e. for any standard cosmological model) either of the expressions (3.14) or (3.15) provides an explicit expression for $I(t)$, which when substituted into (3.12) yields unity on the LHS. Alternatively, if A is not equal to unity, then the solution for a of (3.11) will differ from that obtained from the usual cosmological field equations, for which $A = 1$, but this would result in a different expression for $I(t)$, sufficient to combine with $\dot{a}^2$ in (3.12) to recover the corresponding expression for A on the LHS.

3.5 Comoving and free-fall frames

Having shown above that having A = constant in (3.6) does not require zero active mass, we now address the second part of Melia's argument, in which he claims to provide a justification for requiring A to equal unity; this claim is also incorrect.

In the coordinates defined by (3.6), he first shows that the 4-velocity of an observer comoving with the fluid is

$$u^0 = 1/A, \qquad u^i = 0 \quad (i = 1, 2, 3), \tag{3.16}$$

where the condition $u^i = 0$ shows that r, θ and ϕ are comoving coordinates. He then points out correctly that a free-falling observer is comoving with the fluid, but goes on to suggest incorrectly that this implies that the proper time of a comoving observer must equal the coordinate time t and hence that $A = 1$. He further notes that if A were a function of t (which, according to his incorrect reasoning addressed above, would be necessary if $\rho + 3p \neq 0$), one might attempt to perform a gauge transformation of the form

$$d\tilde{t} = A dt, \tag{3.17}$$

which would reduce the metric back to the FRW form, with $g_{\tilde{t}\tilde{t}} = 1$, but he claims that this is not permitted because of the uniqueness of the comoving, free-falling frame.

These claims are easily demonstrated to be false. As we show below, the coordinate time t is allowed to be any function of the proper time of a comoving observer, τ. Therefore, a gauge transformation of the form given by (3.17) *is* allowed, and hence it is possible to have A to be dependent on t without any problems.

To illustrate this explicitly, let us consider a cosmology for which the evolution of the scale factor as a function of coordinate time t is that in Melia's own model, namely $a(t) = bt$, where b is a constant. Moreover, again following Melia, we will assume that $k = 0 = \Lambda$, but instead of his assumption concerning $p = -\frac{1}{3}\rho$, we take the cosmic fluid to have zero pressure, so that the underlying *physical* cosmology is the Einstein–de–Sitter (EdS) model.

Substituting $a(t) = bt$ into the continuity equation (3.8) for the case of a homogeneous universe, one finds

$$\rho = \frac{C}{t^3}, \tag{3.18}$$

where C is a constant. Substituting this form for the density into our equation for $e^{I(t)}$ in (3.14), we find that for $k = 0$,

$$e^{I(t)} = \frac{3t}{8\pi h C b^2}, \tag{3.19}$$

and using equation (3.12), we find that

$$A(t) = \sqrt{\frac{3t}{8\pi C}}, \tag{3.20}$$

which is clearly not constant.

It is straightforward to find the rest of the metric components, which are

$$B(r,t) = f'(r)bt, \tag{3.21}$$

$$R(r,t) = f(r)a(t) = f(r)bt, \tag{3.22}$$

where $f'(r) = df/dr$ and $f(r)$ is some function of r. With these expressions for A, B and R, we can use the Einstein equations to determine the corresponding stress-energy tensor of the cosmic fluid. As expected, it yields a fluid of density $\rho = C/t^3$, zero pressure, and 4-velocity given by

$$u^0 = 1/A = \sqrt{\frac{8\pi C}{3t}}, \qquad u^i = 0 \quad (i = 1, 2, 3). \tag{3.23}$$

This shows that we are in a frame comoving with the fluid, but there is no requirement that the proper time of a comoving observer must coincide with the coordinate time t.

Indeed, we can find the explicit relationship between t and τ from the first geodesic equation in (3.23). Solving

$$\frac{dt}{d\tau} = \sqrt{\frac{8\pi C}{3t}}, \tag{3.24}$$

subject to the boundary condition $t = \tau = 0$ at the big bang, one finds

$$t = \left(6\pi C \tau^2\right)^{1/3}. \tag{3.25}$$

We may verify that this relationship is correct by noting that it leads to the appropriate expression for the density as a function of the proper time of comoving observers in an EdS universe, namely

$$\rho = \frac{1}{6\pi\tau^2}. \tag{3.26}$$

Hence, the coordinate t here is simply proportional to $\tau^{2/3}$. Note that the specific relation between t and $\tau^{2/3}$ was determined by our choice in $a(t)$; any other choice for $a(t)$ would

also yield constant spatial components in the 4-velocity, and the frame would be declared 'comoving', but the t would not (in general) be the proper time of the comoving observer in that frame, and this occurs without any inconsistencies or restrictions.

This one counter-example is sufficient to prove that a gauge transformation of the form (3.17) is allowed, and A does not necessarily have to be constant. When $A = 1$, we are in the frame of the comoving/freely-falling observer, with the coordinate t equal to their proper time. When $A = A(t)$, the spatial coordinates still are those of the comoving/freely-falling observer, but the coordinate t is simply some function of their proper time, and this function is determined by the specific form of $A(t)$. In this case, one can simply use the gauge transformation given by (3.17) to bring us back to the conventional FRW metric with $A = 1$, in which the time coordinate is equal to the proper time of the comoving observer.

Finally, we address a related part of Melia's argument (Melia 2017), in which he claims that it is inconsistent with basic relativity theory to have $A = 1$ in a cosmological model with $\ddot{a} \neq 0$. He bases this claim on the fact that one can always distinguish between accelerated and inertial frames. In particular, Melia suggests that the accelerated universal expansion should produce a time dilation that is measurable relative to the passage of proper time in the (inertial) free-fall frame, and hence A cannot be unity. The flaw in Melia's argument is that the condition $\ddot{a} \neq 0$ represents a coordinate acceleration rather than a proper acceleration. Any observer comoving with the cosmological fluid follows a geodesic and is hence freely-falling and so does not experience any proper acceleration, and this is perfectly consistent with having $\ddot{a} \neq 0$.

3.6 Conclusions

The above investigations allowed us to re-examine critically the original theoretical arguments set out in Melia (2007, 2009); Melia & Shevchuk (2012) for the so-called $R_\mathrm{h} = ct$ cosmological model, which has recently received considerable attention. After pointing out a number of objections to the $R_\mathrm{h} = ct$ based on recent observational data, we consider in particular the central assumption underlying the original theoretical argument for the model, namely that the comoving Hubble distance should be constant. We demonstrate that this is *not* required, and so find no reliable theoretical basis for the $R_\mathrm{h} = ct$ model.

These considerations in turn elucidated the behaviour of a number of 'horizons' during the general-relativistic evolution of homogeneous and isotropic cosmological models. In particular, we considered the evolution of an imaginary spherical boundary of radius $a(t)$ that is comoving with the fluid and centred on some arbitrary origin. For a selection of analytical spatially-flat cosmological models, we compared $a(t)$ to the Schwarzschild and Hubble radii. In the case of vanishing cosmological constant, we find the generic behaviour (both for dust and radiation

models) that the comoving radius $a(t)$ initially lies outside the Hubble radius, but eventually enters it at precisely the same moment as it exits the Schwarzschild radius; it is allowed to do the latter, since the fluid at the boundary is moving at speed c at this instant. Thus, one has two 'horizon crossings' taking place simultaneously and in opposite directions. In the case $\Lambda \neq 0$, one can obtain two positive solutions for $R_S(t)$, which correspond to the Schwarzschild radius and the de Sitter radius, respectively. One again finds that the comoving radius $a(t)$ initially lies outside the Hubble radius and enters it at precisely the same moment as it exits the Schwarzschild radius, at which point the fluid at the boundary $a(t)$ is moving at speed c. In the presence of non-zero Λ, however, the boundary $a(t)$ later exits the Hubble radius again, at precisely the same moment that it enters the de Sitter radius, at which point the fluid at the boundary is again moving with speed c. This interesting behaviour is not usually pointed out in the literature.

In addition we address the claim in Melia (2016), in which he argues that the FRW cosmology demands the zero active mass condition. To summarize, Melia's first claim is that for A in (3.6) to be a constant, one requires $\rho + 3p = 0$. We have shown that this is false, and results simply from a false step in logic, and we have provided an example using the EdS cosmology that demonstrates this. Secondly, Melia claims that A (and hence Φ using Melia's own notation) needs to be constant, by arguing that the free-fall and comoving frames must coincide. We have shown that the two frames can coincide perfectly well even with A not constant; in this case, the coordinate time t is no longer the proper time of comoving observers, but a function of it arising via a simple gauge transformation.

Thus, contrary to the claims presented in Melia (2016), there is no extra information to be extracted from starting by substituting the general spherically-symmetric metric into the Einstein equations and then imposing homogeneity and isotropy, as compared to the usual route of first imposing homogeneity and isotropy on the metric and then employing the Einstein equations. Hence, the FRW spacetime is perfectly compatible with having $\rho + 3p \neq 0$.

We note that the contents of Sections 3.4 and 3.5 were published in a Letter (Kim et al. 2016). This was contested by Melia in Melia (2017), although this response largely just restates the original argument in Melia (2016) and does not address the specific concerns raised in Kim et al. (2016). We simply note here that in Sections 2.2.2 and 2.3.2, we have carried out the process of imposing homogeneity and isotropy on the solutions of the Einstein field equations for a general, spherically-symmetric system, obtained using our tetrad-based approach and the LTB model, respectively. In both cases, we arrive at the standard FRW metric and the usual cosmological field equations, without encountering any requirement for vanishing active mass.

In closing, it is also worth pointing out here that the many claims that the $R_h = ct$ model is favoured over ΛCDM by observational data should also be treated with caution. As discussed in

the Introduction, more recent observational data cast doubt on the model's central assumptions, but there exists a further issue related to how the $R_{\rm h} = ct$ and ΛCDM models have previously been compared. In the ΛCDM model, there is no requirement that $\rho + 3p = 0$. This condition is, however, broadly consistent with much of the observational data, as has been known for some time. Thus, if one merely imposes this additional condition *post-hoc* on the ΛCDM model, to arrive at the $R_{\rm h} = ct$ model, then any model selection approach will naturally favour the latter. Such analyses have content only if one has a physical reason *a priori* to impose the zero active mass condition. As we have shown, the argument presented in Melia (2016) for imposing this condition is not valid.

Chapter 4

An alternative approach to modelling a cosmic void and its effect on the cosmic microwave background

4.1 Introduction

It is of interest in cosmology to model non-linear structures such as clusters and voids (a cosmological term which refers to underdense regions between filaments that contain few galaxies), and determine the secondary temperature anisotropies that they induce in the cosmic microwave background (CMB). Recent attention has focussed in particular on voids, which arise naturally in ΛCDM cosmologies through the evolution of large scale structure, surrounded by filaments and clusters in the cosmic web (Colless et al. 2001; Tegmark et al. 2004; Sutter et al. 2012). Indeed, voids are of particular interest since their distribution is sensitive to the equation of state of dark energy (Pisani et al. 2015; Lavaux & Wandelt 2012). Moreover, the presence of our Galaxy within a large local void has been suggested as an alternative explanation for observations of the acceleration of the universal expansion, without invoking dark energy (Célérier 2012a,b; Bolejko & Célérier 2010; Bene & Csapo 2010; Kainulainen & Marra 2009; Marra et al. 2008, 2007; Alexander et al. 2009) although it is likely that only a small part of the observed acceleration could be due to such an effect (Geshnizjani et al. 2005; Siegel & Fry 2005; Zibin et al. 2008).

Individual clusters and voids are often modelled as spherically-symmetric, pressureless systems using the Lemaître–Tolman–Bondi (LTB) metric (Romano & Vallejo 2015; Tokutake

& Yoo 2016; Finelli et al. 2016; Brouzakis et al. 2007). The LTB model is usually expressed in comoving coordinates and thus provides a Lagrangian picture of the fluid evolution, as discussed in Section 2.3. Such models can accommodate an arbitrary, usually continuous, density profile for the central object, but do have some limitations. For example, the central object is usually only compensated at infinity, which can complicate the interpretation of observational effects, since observers comoving with the cosmological fluid are not in a region modelled by a homogeneous Friedmann–Robertson–Walker (FRW) cosmology. In principle, compensation at a finite radius can be achieved by an appropriate choice of initial radial density and velocity profiles, but in so doing care must be taken to avoid subsequent streamline crossing, since the presence of shock fronts would necessitate the inclusion of pressure to produce a realistic model. Finally, the LTB metric contains a residual gauge freedom that necessitates the imposition of arbitrary initial conditions to determine the system evolution.

Hence in this Chapter, we use the tetrad-based method, which has various advantages over the LTB method as discussed in Chapter 2, for modelling a void. Assuming a pressureless fluid throughout, the method has already been applied to to modelling the evolution of a finite-size, spherically-symmetric cluster, with continuous radial density and velocity profiles, that is embedded in an expanding background universe and compensated so that it does not exert any gravitational influence on the exterior universe (Lasenby et al. 1999; Dabrowski et al. 1998, 1999). In this approach, one considers an initial velocity profile from which the initial density profile is determined uniquely by the constraints that there are no decaying modes present and that the density distribution is compensated. Moreover, this compensation holds at all later times, and the velocity field evolves in a way that avoids streamline crossing.

In this Chapter, we apply this approach to modelling voids and calculate their effect on the CMB. As a particular example, we consider the Draco supervoid, for which the present day density and velocity profiles have been estimated by Finelli et al. (2016) (hereinafter FGKPS) from a projected underdensity in the WISE-2MASS galaxy survey and a CMB temperature decrement in the Planck data in the same direction. We consider a number of ways in which a similar void can be produced in our approach, and determine the resulting temperature decrements, with particular focus on the influence of the void velocity profile. We also compare our results with those derived previously using the LTB model.

The structure of this Chapter is as follows. In Section 4.2, we introduce the model we use for spherical perturbations that are consistent with having evolved from primordial fluctuations in the early universe. In Section 4.3, we discuss the LTB void model used by Finelli et al. (2016); Mackenzie et al. (2017); Marcos-Caballero et al. (2016); Zibin (2014); Nadathur et al. (2014) in their analyses of supervoids. We then compare CMB decrements caused by voids similar to the LTB model used to represent the Draco supervoid by FGKPS in Sections 4.5 and

4.6. Lastly we present our conclusions in Section 4.7.

4.2 Tetrad-based methodology and void model

Our tetrad-based approach is summarised in the Introduction. Assuming spherical symmetry and a pressureless fluid, one may adopt a gauge in which the non-zero tetrad components are given by ${e_0}^0 = 1$, ${e_0}^1 = g_2$, ${e_1}^1 = g_1$, ${e_2}^2 = 1/r$ and ${e_3}^3 = 1/(r\sin\theta)$, where $g_1(r,t)$ and $g_2(r,t)$ are unknown functions. In this gauge, assuming zero pressure, the metric coefficients derived from the tetrad components lead to the line-element

$$ds^2 = \left(1 - \frac{g_2^2}{g_1^2}\right) dt^2 + \frac{2g_2}{g_1^2}\, dt\, dr - \frac{1}{g_1^2}\, dr^2 - r^2 d\Omega^2. \tag{4.1}$$

The time coordinate t measures the proper time of observers comoving with the fluid, and the (non-comoving) radial coordinate r labels spheres of proper area $4\pi r^2$. It is straightforward to show that g_2 is the rate of change of the r coordinate of a fluid particle (or comoving observer) with respect to its proper time, and so can be physically interpreted as the fluid 3-velocity. As demonstrated below, the physical interpretation of g_1 is such that the total energy per unit mass of a fluid particle is $\frac{1}{2}(g_1^2 - 1)$ (after subtraction of the rest-mass energy).

4.2.1 Field equations

For a fluid with density $\rho(r,t)$, the total mass-energy, $M(r,t)$, contained in a sphere of radius r is given by

$$\frac{\partial M}{\partial r} = 4\pi r^2 \rho, \tag{4.2}$$

and the mass flow through a sphere of radius r per unit time is given by

$$\frac{\partial M}{\partial t} = -4\pi r^2 \rho g_2. \tag{4.3}$$

As mentioned above, the variable g_2 may be interpreted physically as the fluid 3-velocity in the coordinate frame and defines the integral curves of the conserved fluid current by

$$\frac{dr}{dt} = g_2. \tag{4.4}$$

These integral curves are also matter geodesics, since the fluid is pressureless. For functions of both r and t, one can therefore define the comoving derivative

$$\frac{d}{dt} = \frac{\partial}{\partial t} + g_2 \frac{\partial}{\partial r}, \tag{4.5}$$

which determines the rate of change of a quantity along a streamline with respect to the proper time of a comoving fluid element. From equations (4.2) and (4.3), one thus sees that M is

conserved along a streamline, such that

$$\frac{dM}{dt} = 0, \tag{4.6}$$

which prohibits the possibility of streamline crossing.

The continuity equation has the form

$$\frac{d\rho}{dt} = -\left(\frac{2g_2}{r} + H\right)\rho, \tag{4.7}$$

where we have defined the velocity gradient

$$H(r,t) \equiv \frac{\partial g_2}{\partial r}, \tag{4.8}$$

which is equivalent to the spin-connection coefficient F (1.12).

Euler's equation is given by

$$\frac{dg_2}{dt} = -\frac{M}{r^2} + \tfrac{1}{3}\Lambda r, \tag{4.9}$$

the integral of which along a streamline gives the Bernoulli equation,

$$\tfrac{1}{2}g_2^2 - \left(\frac{M}{r} + \tfrac{1}{6}\Lambda r^2\right) = \tfrac{1}{2}\left(g_1^2 - 1\right). \tag{4.10}$$

This provides the physical interpretation of g_1 discussed above. Indeed, by applying the comoving derivative (4.5) to (4.10), and using (4.9), one finds the useful result,

$$\frac{dg_1}{dt} = 0, \tag{4.11}$$

which demonstrates that g_1 is conserved along a streamline.

It is most natural to specify the initial data for the above set of equations in terms of the density and 3-velocity profiles, $\rho(r, t_i)$ and $g_2(r, t_i)$, at some initial time t_i. From these one can calculate $M(r, t_i)$ and $g_1(r, t_i)$, which are then conserved along the streamlines.

4.2.2 Streamline equations

The equations (4.4) and (4.10) can be solved analytically using elliptic integrals to obtain the position r at some time t of a fluid particle, given its position r_i at some initial time t_i. It is often simpler, however, instead to solve numerically the system of first-order ordinary differential equations (4.4) and (4.9), namely (Dabrowski et al. 1999):

$$\frac{dr}{dt} = g_2, \tag{4.12}$$

$$\frac{dg_2}{dt} = -\frac{M(r_i)}{r^2} + \frac{\Lambda}{3}r, \tag{4.13}$$

where r_i is the position of the fluid particle on some streamline at an initial time t_i. These equations can be integrated simultaneously to find the position and velocity of the given fluid particle at a later time t, using the fact that $M(r_i)$ is constant on a given streamline. The fluid density $\rho(r,t)$ and velocity gradient $H(r,t)$ are obtained by performing the numerical differentiation in equations (4.2) and (4.8). Hence, given some initial conditions for the density and velocity distributions, $\rho(r,t_i)$ and $g_2(r,t_i)$, the entire system is determined.

4.2.3 Initial conditions

We demand that the void has grown from primordial fluctuations in the early universe. At such early epochs, it is valid to linearise the field equations around a homogeneous cosmology, which yields two solutions: a growing mode and a decaying mode. By demanding that the decaying mode is absent, and assuming a flat-Λ background cosmology, one finds that the initial velocity and mass distributions are related by (Dabrowski et al. 1999)

$$g_2(t_i,r) = \frac{2r}{3H_i}\left(2H_i^2 - \frac{M_i}{r^3} - \frac{\Lambda}{6}\right). \tag{4.14}$$

This is equivalent to imposing the following relationship between the initial velocity and density distributions

$$\rho(t_i,r) = \frac{3H_i}{8\pi}\left(4H_i - \frac{2g_{2,i}}{r} - H - \frac{\Lambda}{3H_i}\right). \tag{4.15}$$

4.2.4 Photon equations

The photon trajectory can be parameterised using t, such that it is defined by $r(t)$ and $\phi(t)$, where $\phi(t)$ is the azimuthal angle in spherical coordinates. Without loss of generality, we may assume that the trajectory lies in the $\theta = \pi/2$ plane. The requirement that the trajectory is null leads to the conditions

$$\begin{aligned}\frac{dr}{dt} &= g_1\cos\chi + g_2,\\ \frac{d\phi}{dt} &= \frac{\sin\chi}{r},\end{aligned} \tag{4.16}$$

where χ is the angle, as measured by observers comoving with the fluid, between the photon path and centre of the void (which we set to lie at the origin $r = 0$). The geodesic equations then determine how χ evolves with time:

$$\frac{d\chi}{dt} = \sin\chi\left[\cos\chi\left(H - \frac{g_2}{r}\right) - \frac{g_1}{r}\right]. \tag{4.17}$$

These equations are sufficient to calculate the position of the photon along its trajectory, and are easier to integrate numerically than the usual second-order geodesic equations. The trajectory is determined by an initial set of data r_i, ϕ_i and χ_i. For most calculations, however, the data

are provided in the form of the observer's position and an angle on the sky χ, and the equations are then run backwards in time to take the photon back through the void.

The remaining content of the geodesic equations determines the evolution of the photon frequency ω, as measured by a comoving observer:

$$\frac{d\omega}{dt} = -\omega \left(H \cos^2 \chi + \frac{g_2}{r} \sin^2 \chi \right). \tag{4.18}$$

One can show from the above equations that the angular momentum of the photon, $L = -r^2 \omega \, d\phi/dt = -\omega r \sin \chi$, is conserved.

To calculate the effect of the void on a CMB photon, we first write

$$g_2(t, r) = r H_e(t) + \Delta(t, r), \tag{4.19}$$

where $H_e(t)$ is the Hubble function in the exterior Universe at time t, and Δ is thus the difference between the equivalent fluid velocity in the unperturbed Universe and in the void. One may then show that the physically measurable CMB temperature decrement due to the void is given by (Lasenby et al. 1999)

$$\frac{\Delta T}{T} = e^{-\epsilon} - 1 \approx -\epsilon, \tag{4.20}$$

where the small quantity ϵ is defined by

$$\epsilon = \int_{t_1}^{t_2} dt \left(\frac{\partial \Delta}{\partial r} \cos^2 \chi + \frac{\Delta}{r} \sin^2 \chi \right). \tag{4.21}$$

This integral is evaluated along the photon path between the time the photon enters the void (t_1) and the time it leaves (t_2). The function ϵ is small, since the contribution to the integral from near the void centre tends to cancel the contributions from further out. The main effect producing a non-zero ϵ is essentially the evolution of Δ with time.

4.2.5 Void model

Our void model is based on that used to model a cluster in Dabrowski et al. (1998). The nature of the void is determined by specifying the velocity distribution $g_2(r, t_i)$ at some initial time t_i in terms of four parameters H_i, R_i, a and m. Here, $H_i \equiv H_e(t_i)$ is the background Hubble parameter at $t = t_i$, R_i is the initial size of the perturbed region, and a is the velocity gradient at the origin (which determines the magnitude of the perturbation). For $r < R_i$, the fluid velocity is described by a polynomial in r of order $2m + 1$, and the first m radial derivatives are matched at the boundaries, $r = 0$ and $r = R_i$. For $r > R_i$, the fluid velocity is that of the background $g_2(r, t_i) = r H_i$. The initial density profile $\rho(r, t_i)$ is then determined using equation (4.15), such that the density is a polynomial of order $2m$. One can show that the resulting initial density profile is compensated, and hence remains compensated for all time. Consequently,

in the external region ($r > R_i$) the fluid evolves as a homogeneous FRW universe. Placing observers in this region allows for unambiguous calculations of the CMB perturbation caused by the void. Once the initial velocity and density profiles are defined, the evolution of the fluid is then completely determined.

A velocity gradient at the origin that is slightly greater than that of the unperturbed universe, so that $a > H_i$, leads to the formation of a void (and, conversely, setting $a < H_i$ would lead to the formation of a cluster). Also, the boundary conditions imply that when the value of m is greater than unity, the density gradient is zero at the origin, whereas this condition is not necessarily satisfied for $m = 1$; hence we choose $m \geq 2$ for a sensible density profile.

4.3 LTB model

Having discussed our own methodology for modelling voids, we now turn to an approach based on the LTB model, and establish the relations between quantities in the two models.

The LTB metric (Lemaître 1933; Tolman 1934; Bondi 1947) describes a spherically-symmetric pressureless system, and may be written in the form

$$ds^2 = d\hat{t}^2 - \frac{(\partial_{\hat{r}} R)^2}{1 + 2E(\hat{r})} - R^2 d\Omega^2, \tag{4.22}$$

where $\hat{r}$ is a comoving radial coordinate and the time coordinate $\hat{t}$ coincides with the proper time measured by observers comoving with the fluid. The function R depends, in general, on both $\hat{t}$ and $\hat{r}$, and the function $E(\hat{r})$ determines the so-called 'curvature profile' of the system, and may be specified arbitrarily, provided $E(\hat{r}) > -\frac{1}{2}$.

As discussed in Chapter 2, one may transform the line-element (4.1) used in our tetrad-based approach into the LTB line-element (4.22) via the coordinate transformation

$$t = \hat{t}, \quad r = R(\hat{r}, \hat{t}), \quad \text{where} \quad \frac{\partial R}{\partial \hat{t}} = g_2, \tag{4.23}$$

where this time $f_1 = 1$ as we assume a pressureless fluid. In so doing one makes the further identification $g_1^2 = 1 + 2E(\hat{r})$, which confirms the usual alternative interpretation of $E(\hat{r})$ as the energy per unit mass of a fluid particle (after subtracting its rest mass). One may also show that with pressureless fluid, partial derivatives in the two coordinate systems are related by

$$\frac{\partial}{\partial \hat{t}} = \frac{\partial}{\partial t} + g_2 \frac{\partial}{\partial r} = \frac{d}{dt}, \tag{4.24}$$

$$\frac{\partial}{\partial \hat{r}} = \frac{\partial R}{\partial \hat{r}} \frac{\partial}{\partial r}. \tag{4.25}$$

Since $\frac{d}{dt}$ is the convective derivative, the transformation (4.23) is naturally interpreted as moving from a Eulerian to a Lagrangian description of the fluid motion.

In LTB coordinates, one finds $\partial_{\hat{t}} M = 0$, so that $M = M(\hat{r})$, which is interpreted as the mass contained within the comoving radius $\hat{r}$. The remaining Einstein equations become

$$\partial_{\hat{r}} M(\hat{r}) = 4\pi R^2 \rho \, \partial_{\hat{r}} R, \tag{4.26}$$

$$(\partial_{\hat{t}} R)^2 = 2E(\hat{r}) + \frac{2M(\hat{r})}{R} + \tfrac{1}{3}\Lambda R^2. \tag{4.27}$$

The latter is the LTB equivalent of the Bernoulli equation (4.10), for which the solution $R(\hat{r}, \hat{t})$ can be written in integral form as

$$\hat{t} - \hat{t}_B(\hat{r}) = \int_0^{R(\hat{r},\hat{t})} \frac{dA}{\sqrt{2E(\hat{r}) + \frac{2M(\hat{r})}{A} + \frac{1}{3}\Lambda A^2}}, \tag{4.28}$$

where the function $\hat{t}_B(\hat{r})$ is known as the bang-time, which is interpreted as a Big-Bang singularity surface at which R vanishes, i.e. $R(\hat{r}, \hat{t}_B(\hat{r})) = 0$, and may be chosen arbitrarily.

In the LTB model, one is thus required to specify three arbitrary time-independent functions. The functions $E(\hat{r})$ and $\hat{t}_B(\hat{r})$ are usually interpreted as determining the nature of the system, and the remaining gauge freedom in redefining the radial coordinate is usually removed by specifying $M(\hat{r})$. In this case, (4.28) can then be solved for $R(\hat{r}, \hat{t})$, so that metric (4.22) is fully determined, and the corresponding density $\rho(\hat{r}, \hat{t})$ is found from (4.26). A common alternative gauge-fixing procedure is instead to specify $R(\hat{r}, \hat{t}_0)$, where $\hat{t}_0$ denotes the current epoch $\hat{t}_0$. In this case, (4.28) is then solved at $\hat{t}_0$ for $M(\hat{r})$, before proceeding as before. It is worth noting that, in order for no decaying mode to be present, one requires $\hat{t}_B(\hat{r})$ not to be spatially varying, and one may choose $\hat{t}_B = 0$ without loss of generality (Zibin 2008).

4.4 Modelling the Draco void

We now wish to compare our tetrad-based approach with the LTB model in in the context of modelling a specific void structure. Our main aim will be to show that in comparing void models with CMB data, both the underlying density and velocity profiles of the void are important, and should both be considered. We also wish to demonstrate, however, that the tetrad-based approach is simpler and more intuitive in some respects than the LTB model, although the latter does of course remain a valid approach. Indeed, when the issues related to density versus velocity profile are set aside, the quantitative differences that arise between the two methods in modelling the cosmic void considered below are only at the few per cent level.

The particular approach we consider is that adopted by Finelli et al. (2016) (hereinafter FGKPS). They used the LTB metric to model compensated voids and showed that a large void can lead to a significant temperature decrement in the CMB. Indeed, in the first version of their paper (Finelli et al. 2014), and following their identification of a projected underdensity in the

WISE-2MASS all-sky infrared galaxy catalogue aligned with the CMB Cold Spot direction, they originally stated that a supervoid of size $\sim$ 400 Mpc and depth (fractional overdensity) $\delta \sim -0.10$ can explain the Cold Spot temperature decrement of $\Delta T \sim 150\mu$K; they also stated that this decrement is mostly due to the Rees–Sciama (RS) effect (Finelli et al. 2014), rather than the linear integrated Sachs-Wolfe (ISW) effect. Nonetheless, it was later shown by Zibin (2014) and Nadathur et al. (2014), again using the LTB approach, that the ISW effect dominates and that a void of these proportions is not capable of producing such a large CMB decrement. In the later version of their paper, FGKPS accept that the Cold Spot decrement is difficult to explain by the presence of a single supervoid only, but drew attention to another sky area where a large underdensity in the projected WISE-2MASS galaxy map (which they call the Draco supervoid) can account for the CMB decrement observed in that direction.

In this Section, we therefore summarise the LTB approach used by FGKPS to describe the Draco supervoid and then in the following Section compare the results of this model with what is obtained using our own tetrad-based model.

4.4.1 Modelling the Draco void using an LTB approach

To model the Draco void, FGKPS choose the curvature profile to have the form

$$E(\hat{r}) = E_0 \hat{r}^2 \exp\left(-\frac{\hat{r}^2}{\hat{r}_0^2}\right). \tag{4.29}$$

FGKPS do not specify their choice for the bang-time $\hat{t}_B(\hat{r})$, but we presume that it is set to a constant (which one may take to be zero) so that their model contains no decaying mode. FGKPS also do not specify their gauge choice, but reference is made to an earlier work (Garcia-Bellido & Haugbølle 2008) in which they fix the gauge by setting $R(\hat{r}, \hat{t}_0) = \hat{r}$. From (4.26), this is equivalent to setting $M(\hat{r}) = \frac{4\pi}{3}\hat{r}^3 \rho(\hat{r}, \hat{t}_0)$, where $M(\hat{r})$ is determined from (4.28).

FGKPS also appear to fix the present-day density contrast, which as pointed out by Nadathur et al. (2014) could over-constrain their model, and we discuss this aspect further below. In particular, they assume the curvature profile (4.29) to correspond to a perturbation Φ in the synchronous gauge in a spatially-flat ΛCDM model. Treating the perturbation as linear gives rise to the present-day metric perturbation $\Phi(\hat{r}) = \Phi_0 \exp(-\hat{r}^2/\hat{r}_0^2)$. Taking the growing mode and using the Poisson equation, FGKPS obtain the present-day density contrast

$$\delta(\hat{r}) = -\delta_0 \left(1 - \frac{2\hat{r}^2}{3\hat{r}_0^2}\right) \exp\left(-\frac{\hat{r}^2}{\hat{r}_0^2}\right), \tag{4.30}$$

where $\delta(r,t) \equiv \frac{\delta\rho}{\rho}$, which is plotted in Fig. 4.1 and ensures that the void is compensated at infinity.

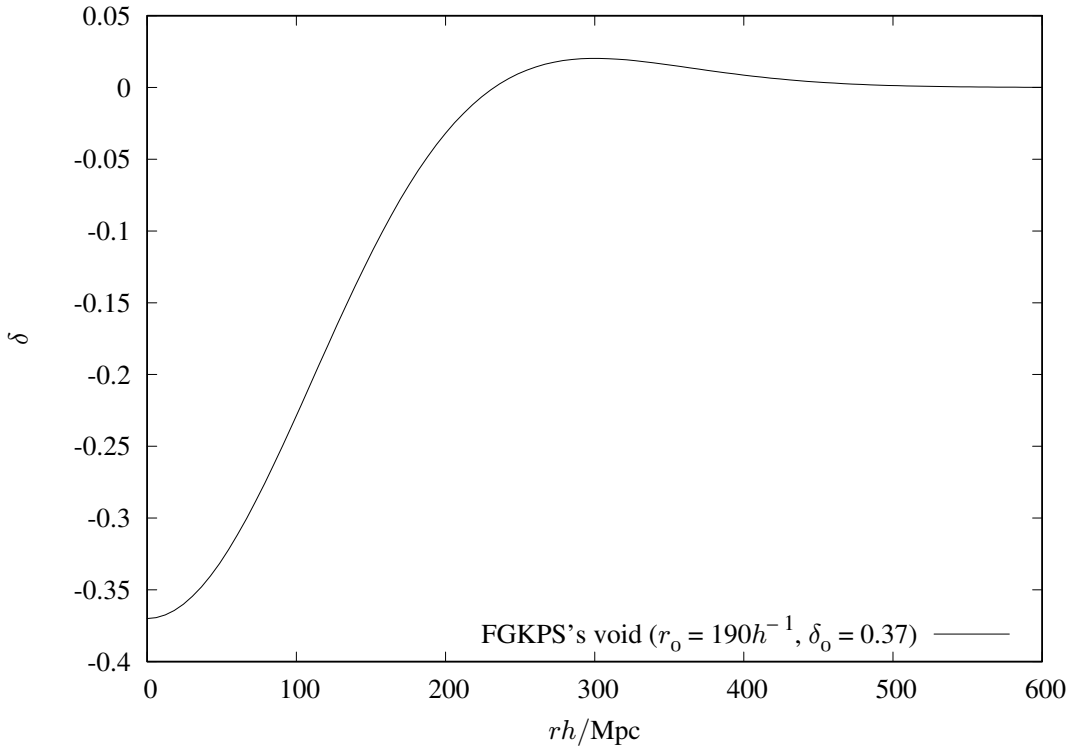

Figure 4.1: Present-day density contrast used by Finelli et al. (2016) to model the Draco supervoid.

This density contrast (projected onto the sky) and the CMB decrement produced by the RS and ISW effects calculated from the metric perturbation Φ are then used in a simultaneous χ^2 fit to the void in the WISE-2MASS galaxy catalogue and Planck CMB data to estimate the three parameters, δ_0, r_0 and z_0, where z_0 is defined as the redshift at the centre of the void. The best-fit values and 68 per cent confidence limits were found to be

$$\begin{aligned} \delta_0 &= 0.37^{+0.22}_{-0.12}, \\ r_0 &= 190^{+39}_{-27}\ \mathrm{Mpc}/h, \\ z_0 &= 0.15^{+0.04}_{-0.05}, \end{aligned} \tag{4.31}$$

where h is defined such that the current Hubble parameter is given by $H_0 = 100h\ \mathrm{km\,s^{-1}Mpc^{-1}}$.

4.4.2 Presence of decaying mode

If FGKPS do indeed specify both the gauge condition $R(\hat{r}, \hat{t}_0) = \hat{r}$ and the present-day density contrast (4.30), then it will not be possible, in general, to satisfy the constraint (4.28) with $\hat{t}_B(\hat{r})$ being equal to a constant (usually zero). Consequently, the void model would contain

some contribution from a decaying mode, and thus be incompatible with the standard picture of cosmological structure formation (Zibin 2008; Nadathur et al. 2014).

To demonstrate this possibility, we calculate the quantity

$$\hat{t}'(\hat{r}) = \int_0^{\hat{r}} \frac{dA}{\sqrt{2E(\hat{r}) + \frac{2M(\hat{r})}{A} + \frac{1}{3}\Lambda A^2}}, \tag{4.32}$$

in which $E(\hat{r})$ is given by (4.29) and

$$M(\hat{r}) = \frac{4\pi\hat{r}^3}{3}\bar{\rho}(\hat{t}_0)\,(1 + \delta(\hat{r}))\,, \tag{4.33}$$

where $\bar{\rho}(\hat{t}_0)$ is the present-day background FRW density and the present-day density contrast $\delta(\hat{r})$ is given by (4.30). If this specification were consistent with the absence of a decaying mode contribution, then $\hat{t}'(\hat{r})$ should be constant and equal to $\hat{t}_0$, which is 13.5 Gyr for the assumed background cosmology.

In addition, FGKPS do not specify the value of E_0 used to set the amplitude of their curvature profile in (4.29). We therefore try two different methods to determine the value of E_0. The first is to find the value of E_0 which minimises the rms variation of $\hat{t}'(\hat{r})$ over the range $0 < \hat{r} < 600$ Mpc. Using the best-fit values of δ_0 and $\hat{r}_0$ for the Draco supervoid given in (4.31), we find that the rms variation is minimised when $E_0\hat{r}_0^2 = 5.3 \times 10^{-4}$. The second method is to treat the perturbation as having linearly grown (as outlined in Zibin (2014)). This results in $E_0\hat{r}_0^2 = 4.78 \times 10^{-4}$. One would expect the nonlinear growth to deviate from this however, as the density contrast is fairly large.

The corresponding ratio $\hat{t}'(\hat{r})/\hat{t}_0$ is plotted in Fig. 4.2 for each value of E_0, and clearly neither is constant and equal to unity. Indeed, $\hat{t}'(\hat{r})$ exhibits a ~ 2 per cent variation about a mean value of ≈ 13.2 Gyr. We may thus conclude that the resulting LTB model must have some contribution from a decaying mode, although the difference between the imposed present-day density profile and one that contains no decaying mode contribution is only at the level of a few per cent. This is in agreement with level of inconsistency found by Nadathur et al. (2014), who instead estimated the value of E_0 in the FGKPS model by minimising the difference $\hat{t}'(\hat{r}) - \hat{t_0}$ at the single point $\hat{r} = 0$ (Nadathur, private communication). Our findings are also consistent with those of Zibin (2014), who finds that the present-day density profile imposed by FGKPS differs from that obtained from (4.26) in a self-consistent LTB model, although again the discrepancy is small. In the rest of the Chapter choose the value of E_0 found by minimising the rms variation in $\hat{t}'(\hat{r})$, namely $E_0\hat{r}_0^2 = 5.3 \times 10^{-4}$.

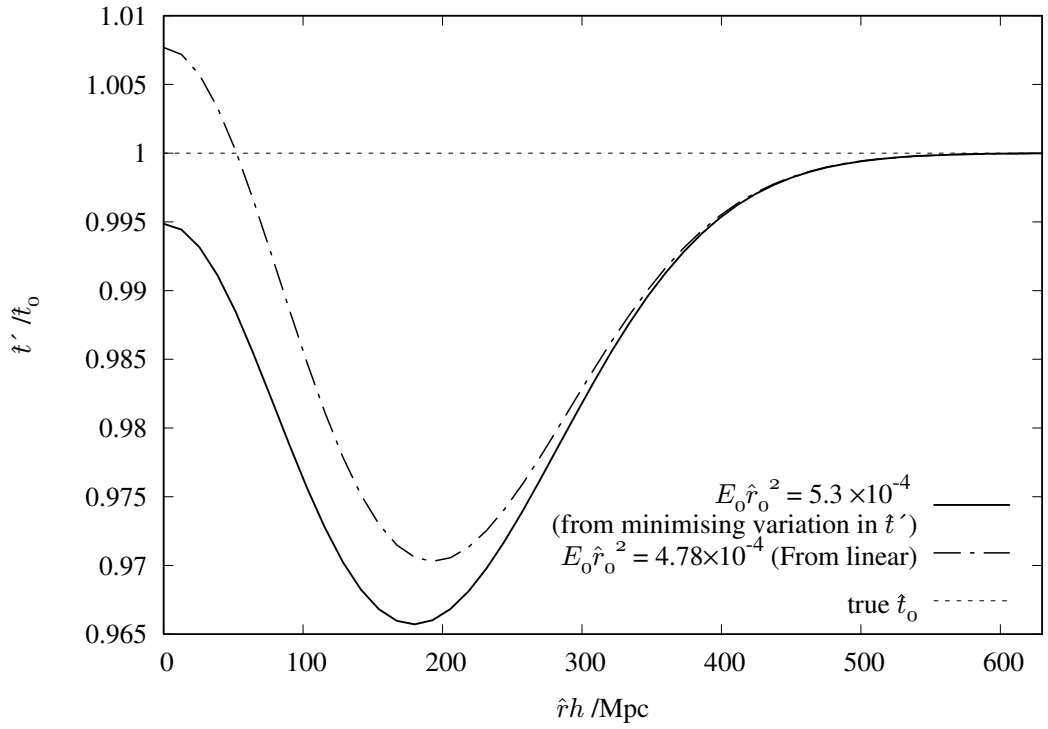

Figure 4.2: Plot of $\hat{t}'$ using different values of E_0, using parameters for the Draco supervoid (4.31). The variation is at its smallest when $E_0\hat{r}_0^2 = 5.3\times10^{-4}$. As $\hat{r}\to\infty$, $\hat{t}'\to\hat{t}_0$ for all values of E_0, as expected.

4.5 Reproducing the Draco void

The issues outlined in the previous Section arise, in part, from the subtleties associated with gauge-fixing in the LTB model, for which the physical interpretation in unintuitive. In this Section, we therefore instead model the Draco void using the tetrad-based approach described in Section 4.2, for which we believe the physical interpretation is clearer. Rather than simply fitting our model directly to the WISE-2MASS galaxy survey data and Planck CMB observations, however, we wish to focus on the different nature of the void characteristics in the LTB and tetrad-based approaches. Consequently, we will compare our model instead with the LTB model derived by FGKPS for the Draco void. In particular, we wish to determine the CMB temperature decrement produced by a void with present-day characteristics similar to those of the FGKPS void model for Draco, but modelled using our approach.

As mentioned in Section 4.2.5, in our approach the nature of the present-day void is determined by specifying the velocity distribution $g_2(r,t_i)$ at some initial time in terms of the four parameters H_i, R_i, a and m. We choose here to set these conditions at $z=10^3$, since the perturbations are safely within the linear regime at this epoch. The initial density distribution is

then determined by the requirement that the decaying mode is absent in the linearised limit, as discussed in Section 4.2.3. Following FGKPS, we assume a spatially-flat ΛCDM background cosmology with $\Omega_\Lambda = 0.7$, for which $H_i = 1.735 \times 10^6 h\,\mathrm{km\,s^{-1}Mpc^{-1}}$. To determine the appropriate values for the remaining parameters R_i, a and m, one has the choice of attempting to reproduce the present-day distribution in the FGKPS Draco void model of either: density, velocity, or both. We consider each of these in turn. As we will see, these options lead to very different CMB temperature decrements.

4.5.1 Reproducing the density profile

We begin by choosing the initial velocity perturbation parameters R_i, a and m such that the resulting present-day density profile of the void $\rho(r, t_0)$ is as similar as possible to that of the FGKPS Draco void model, which is plotted in Fig. 4.1.

This is achieved by performing a numerical optimisation in which the values of R_i, a and m are varied. For each set of parameter values, the resulting present-day density profile is evaluated at 40 equally-spaced points in the range $0 < r < 500$ Mpc and compared with the corresponding values in the FGKPS Draco void density profile. The optimal values of the parameters are those that minimise and sum of the squares of the differences in the two profiles. The resulting optimal present-day density profile is compared with the FGKPS density profile in Fig. 4.3. Given the very different underlying physical models, there is reasonably close agreement between the density profiles. In particular, we find that lower values of the parameter m are preferred, since they result in a smoother density profile in our model; we thus use $m = 2$ for the remainder of this Section.

Since our primary interest, however, is in the CMB temperature decrement produced by our void, it is worth recalling from Section 4.2.4 that the main contribution to this effect is the evolution of the difference Δ between the equivalent fluid velocity in the external universe and in the void, as the CMB photon traverses it. Consequently, it is of interest also to compare the velocity distribution of our void to that of the FGKPS void.

To determine the velocity distribution of the FGKPS void, we note from (4.23) that the LHS of (4.27) gives the square of the fluid velocity in the LTB model at any given epoch. Using the forms for $E(\hat{r})$ and $M(\hat{r})$ given in (4.29) and (4.33), respectively, and employing the gauge condition $R(\hat{r}, \hat{t}_0) = \hat{r}$, one thus obtains the velocity profile at the current epoch. The corresponding Δ profile is plotted Fig. 4.4 for two different values of the parameter E_0 that defines the amplitude of the LTB curvature profile (solid and dotted lines), together with the Δ profile from our void (crosses). The solid line corresponds to the value of E_0 determined in Section 4.4.2, whereas the dotted lines corresponds to a value of E_0 that is a factor of 5 smaller. Two points are worth noting from this figure. First, the Δ profile of the LTB void is sensitive to

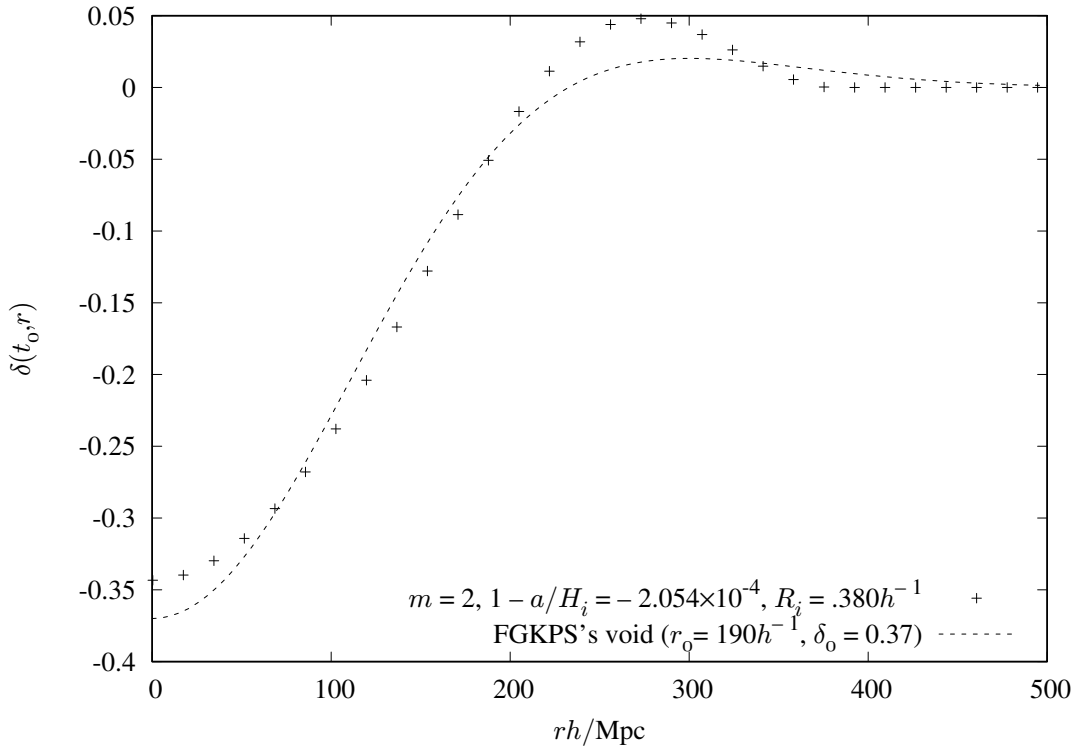

Figure 4.3: Void density profile at $t = t_0$ in our model (crosses), resulting from an initial velocity perturbation at $z = 10^3$ with parameters chosen to reproduce the FGKPS void density profile (dashed line) as closely as possible.

the value of E_0, although the maximum difference between the two LTB Δ profiles is only at the ~ 10 per cent level. Second, the velocity profile of our void differs substantially from that of the LTB void for either value of E_0, even though the density profiles of the two voids agree reasonably well (by construction), as shown in Fig. 4.3.

To determine the CMB temperature decrement produced by our void, we consider an observer comoving with the cosmic fluid in the external universe. The present-day distance of the observer from the void is chosen such that the centre of the void lies at a redshift $z_c = 0.15$. This corresponds to a comoving radial coordinate distance $\hat{r} = 434h^{-1}$ Mpc. Since FGKPS employ the gauge condition $R(\hat{r}, \hat{t}_0) = \hat{r}$ at t_0, this corresponds simply to a non-comoving radial coordinate distance of $r = 434h^{-1}$ Mpc at the current epoch. The resulting CMB temperature decrement $\Delta T(\theta)$ is plotted in Fig. 4.5, and is very similar to that obtained by FGKPS, both in terms of its angular profile and central value of $\Delta T \approx -25\ \mu$K. In Fig. 4.6, we also plot the variation of $\Delta T/T$, as measured by a comoving observer at each point along the path of a photon that passes through the centre of the void, which nicely demonstrates that the observer does indeed lie in the external universe, beyond the finite compensation radius of our void.

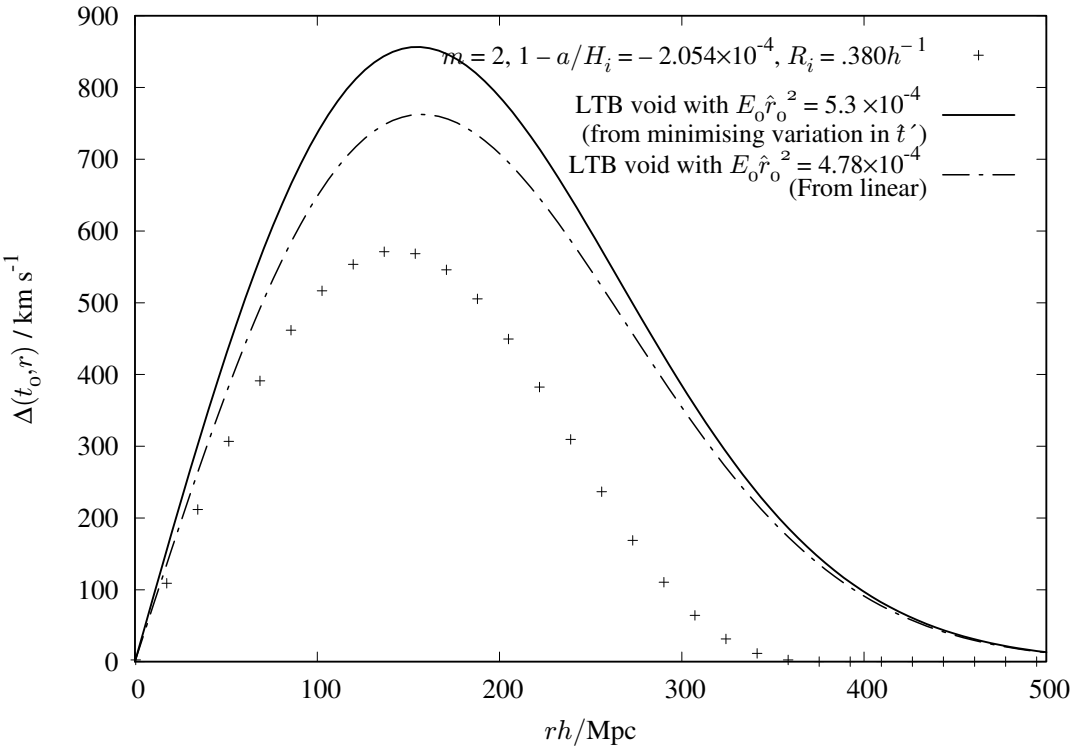

Figure 4.4: Difference $\Delta \equiv g_2 - rH_e$ at $t = t_0$ between the fluid velocity in the void and in the external universe for our void model (crosses) and the LTB void model of FGKPS for two different values of E_0 (solid and dotted lines).

4.5.2 Reproducing the velocity profile

Since the velocity profile of our void discussed above differs significantly from that of the FGKPS void, an alternative approach is instead to choose the initial velocity perturbation parameters R_i, a and m such that the resulting present-day velocity profiles of the two voids models are as close as possible. This is achieved by performing an analogous numerical optimisation to that used above.

The resulting present-day density and velocity difference Δ profiles are plotted in Fig. 4.7, and are compared to those of the FGKPS void model. In this case, one sees that the Δ profiles of the two void models are much closer than what was achieved in the previous subsection, although this comes at the cost of poorer agreement between the density profiles. In particular, the spatial extent of the density profile for our void is larger than in the previous case.

The larger spatial extent of our void model in this case requires us to take care in determining the CMB temperature decrement it produces, since placing the centre of the void at a redshift $z_c = 0.15$ from the observer is insufficient for the observer to reside in the external universe, beyond the finite compensation radius of the void. Nonetheless, this may be achieved by placing

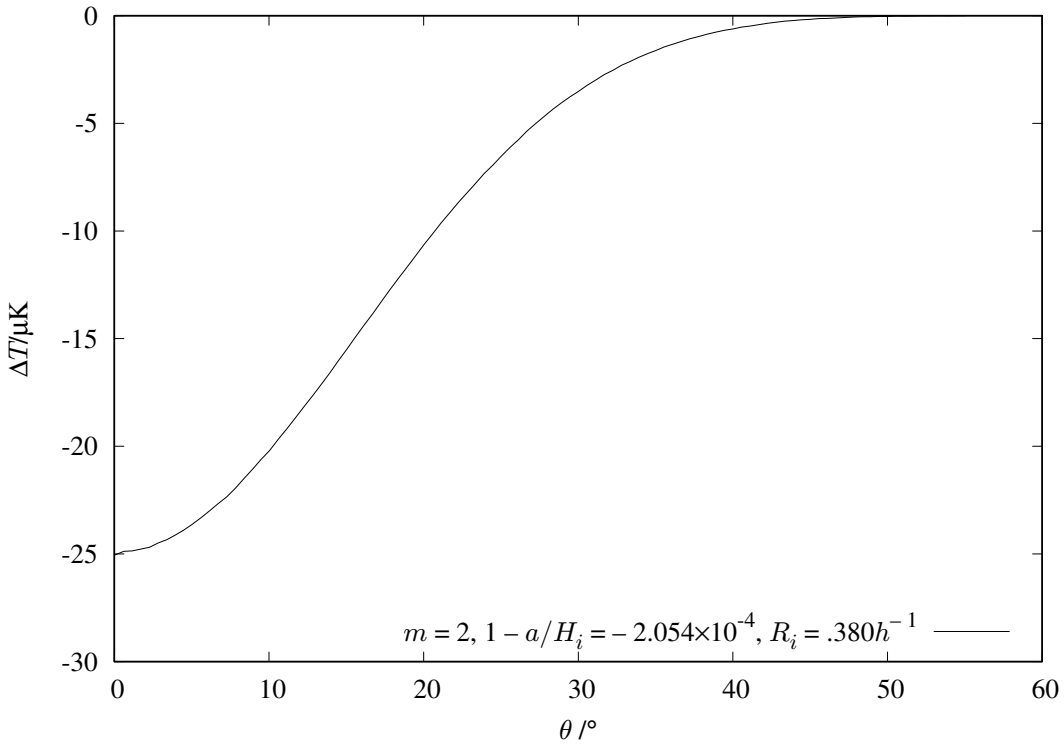

Figure 4.5: CMB temperature decrement for our void model that best reproduces the present-day density distribution of the FGKPS void. The background CMB temperature is taken to be 2.725K.

the centre of the void at a redshift of $z_c = 0.165$, which corresponds to the observer lying at a radial coordinate distance of $r = 476h^{-1}$ (= 600) Mpc. The corresponding CMB temperature decrement is plotted in Fig. 4.8. As expected, the angular profile of the decrement is larger than that shown in Fig. 4.5 for our previous void model. Most notable, however, is the central value of $\Delta T \approx -48$ μK, which is almost twice that obtained previously.

4.5.3 Reproducing the density and velocity profiles

The next obvious approach to consider is to choose the initial velocity perturbation parameters R_i, a and m such that the resulting present-day density *and* velocity profiles of our void model match those of the FGKPS void model as closely as possible. As before, this is achieved by performing a numerical optimisation similar to that used above. In this case, however, we employ a chi-squared approach in which the uncertainties on the mismatch are taken to be $\sigma_\delta = 0.01$ and $\sigma_v = 30\mathrm{km\,s^{-1}}$ for the density and velocity profiles, respectively, which ensures that the contribution to the best fit value of χ^2 in roughly similar for the density and velocity profiles. The value of m is fixed to be 2.

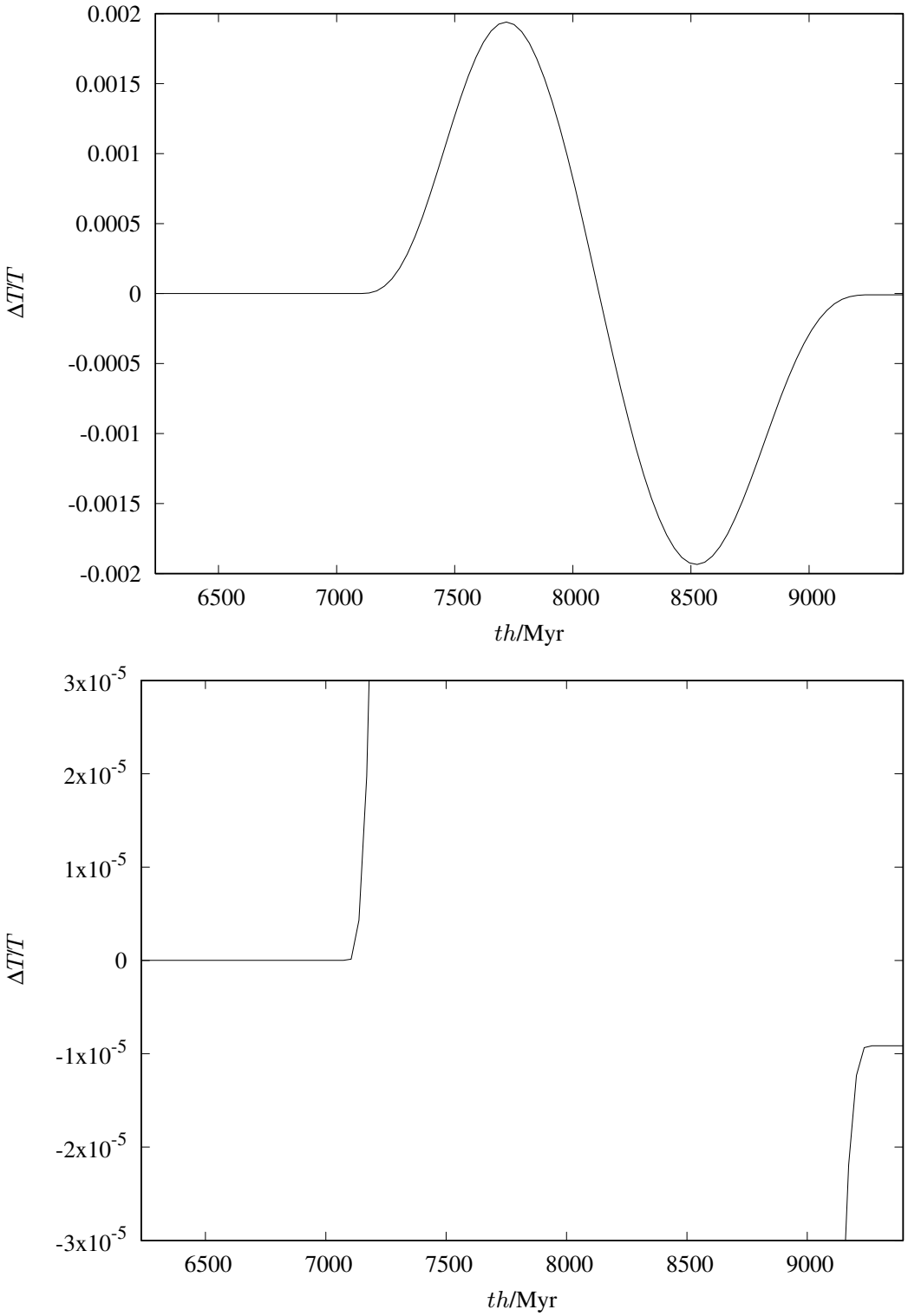

Figure 4.6: As in Fig. 4.5, but for the variation of $\Delta T/T$, as measured by a comoving observer at each point along the path of a photon that passes through the centre of the void. The lower panel is identical to the upper panel, but is plotted on an expanded $\Delta T/T$ scale to illustrate the final decrement of $\Delta T/T = -9.16 \times 10^{-6}$.

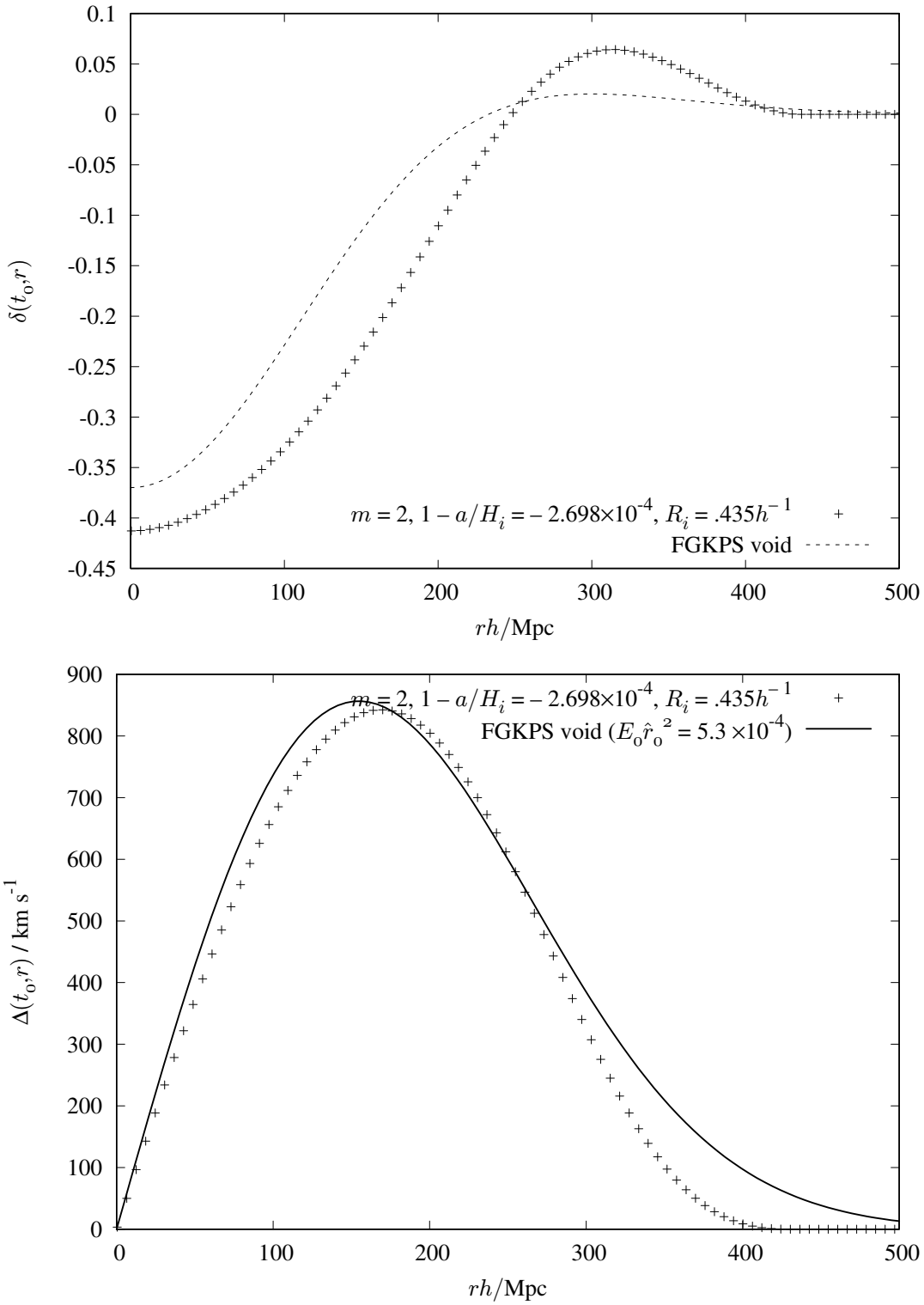

Figure 4.7: Void density profile (top) and velocity difference Δ profile (bottom) at $t = t_0$ in our model (crosses), resulting from an initial velocity perturbation at $z = 10^3$ with parameters chosen to reproduce the FGKPS void velocity profile (solid line, bottom panel) as closely as possible.

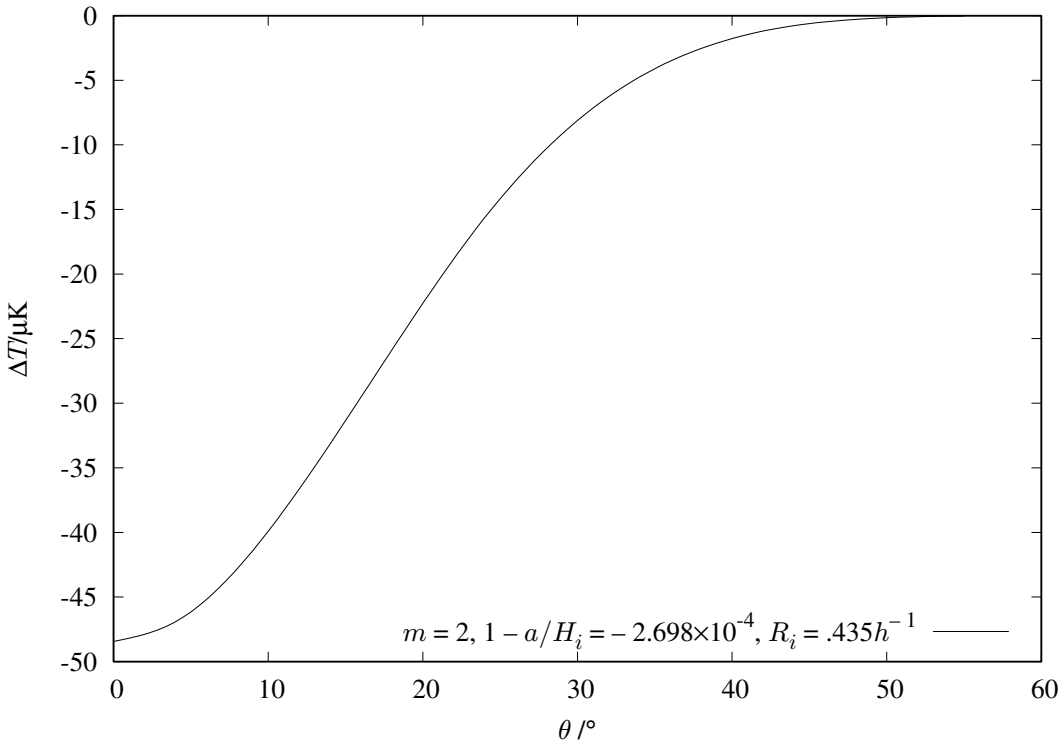

Figure 4.8: As in Fig. 4.5, but for our void model that best reproduces the present-day velocity distribution of the FGKPS void.

The resulting present-day density and velocity difference Δ profiles are plotted in Fig. 4.9, and are compared to those of the FGKPS void model. As one might expect, both profiles in our void agree reasonably well with those in the FGKPS void, but neither agrees as closely as in the case where the optimisation was performed for that profile alone. In particular, the spatial extent of the density profile is similar to that found when optimising the velocity profile alone, and somewhat larger than when optimising for the density profile alone.

As in the previous subsection, the larger spatial extent of our void model requires us to place the centre of the void at a redshift $z_c = 0.165$ from the observer, in order for the observer to be in the external universe. The resulting CMB temperature decrement is shown in Fig. 4.10, which is similar in both angular extent and depth to that plotted in Fig. 4.8.

4.5.4 Consistency with observations

Although we have focussed on comparing the different characteristics of the Draco void models produced by the LTB and tetrad-based approaches, respectively, it is important to determine whether the set of void models produced using our alternative methodology is consistent with observations. In Fig 4.11, we thus compare the projected density profiles and CMB

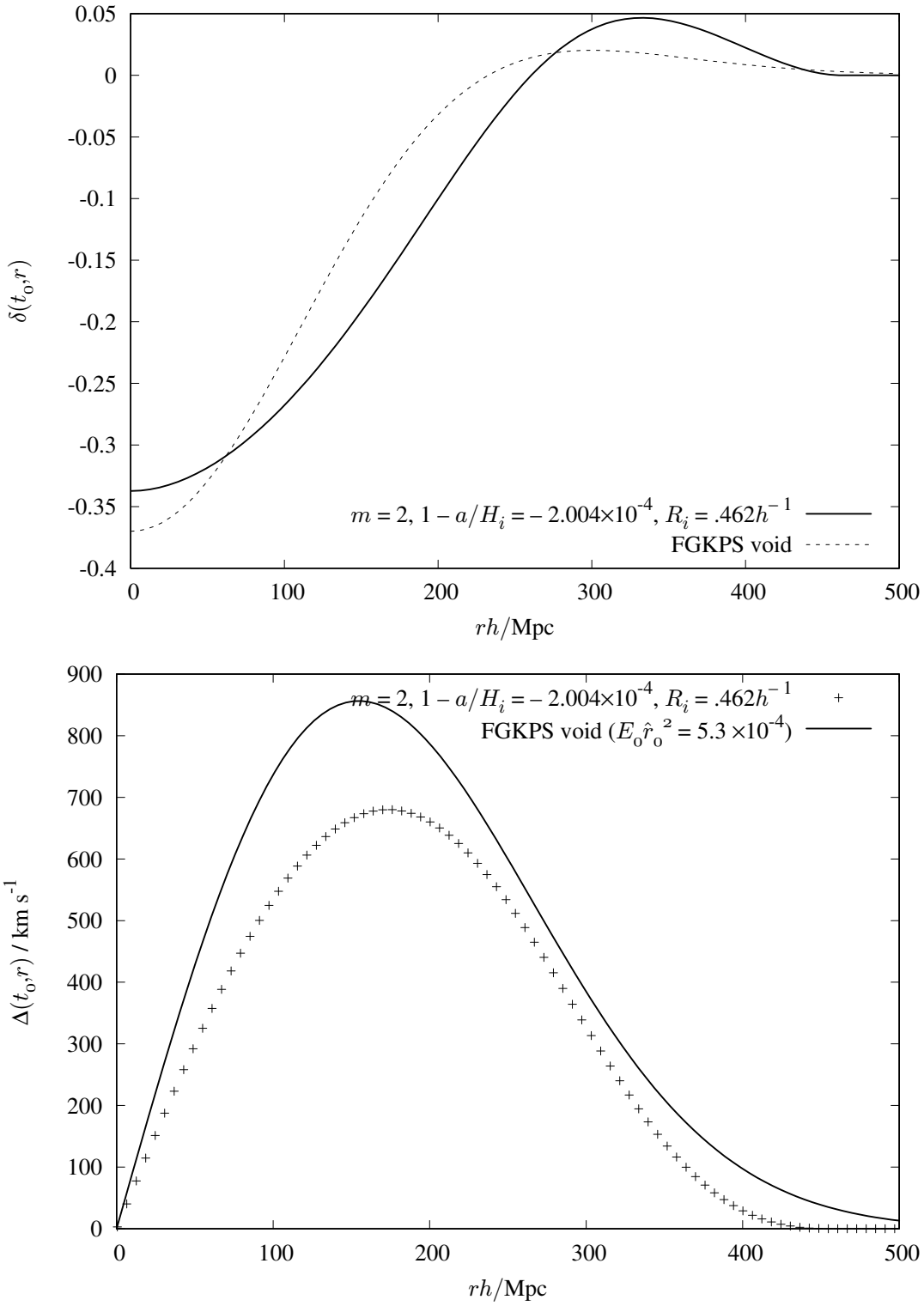

Figure 4.9: As in Fig. 4.7, but for an initial velocity perturbation at $z = 10^3$ with parameters chosen to reproduce the FGKPS void density and velocity profile (solid lines) as closely as possible.

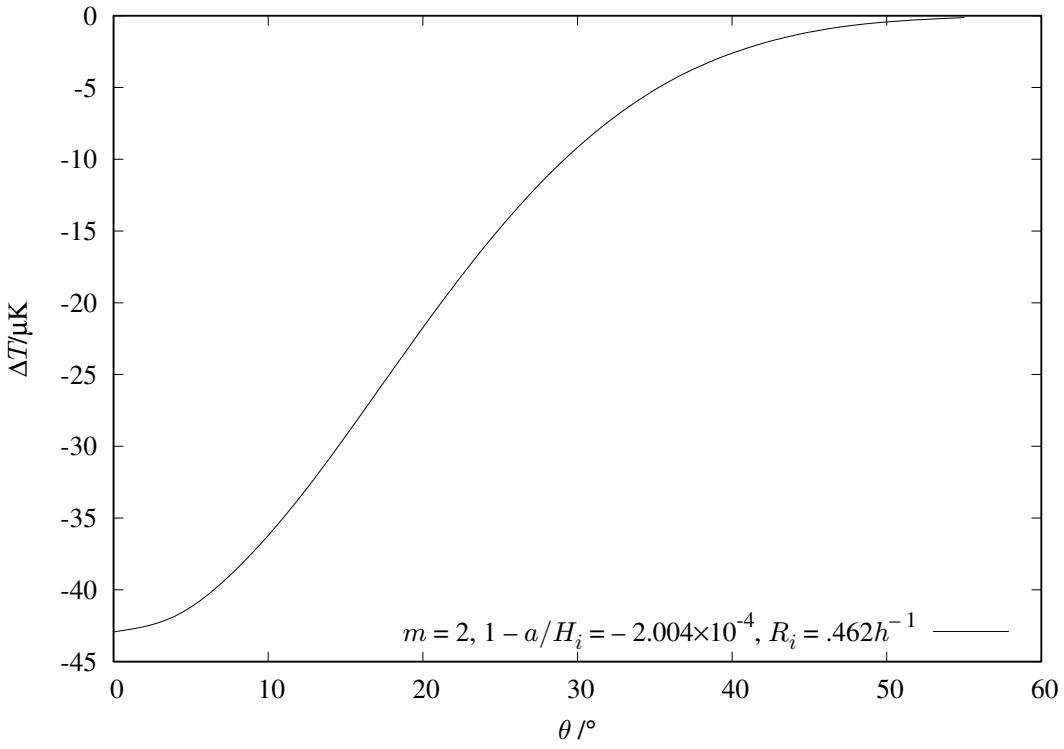

Figure 4.10: As in Fig. 4.5, but for our void model that best reproduces the present-day density and velocity distributions of the FGKPS void.

temperature decrements of our three void models considered in subsections 4.5.1–4.5.3 with the WISE-2MASS galaxy catalogue and the Planck CMB data. The data points are taken directly from FGKPS. We see that all three void models are consistent with the WISE-2MASS data. The CMB temperature decrement of our first void model is consistent with the Planck data on all scales, but our second and third void models are consistent with the Planck data only on larger scales, and yield too large a decrement on angular scales below $\sim 20°$.

Although the LTB void model of FGKPS and our three void models are each consistent with the galaxy counts and broadly consistent with CMB observations in the direction of Draco (at least on angular scales $\geq 20°$), it is clear that there remain considerable differences between the models, which result from the different parameterisations that they employ. Indeed, the above investigations show that relatively slight differences in the parameterisation can lead to large changes in the relationship between density and velocity profiles, and very different CMB temperature decrements. Moreover, all of the models considered are consistent with having grown from primordial perturbations in the early universe. One must therefore be careful in drawing conclusions regarding the physical characteristics of voids from data that constrain just their project density distribution and CMB temperature decrement.

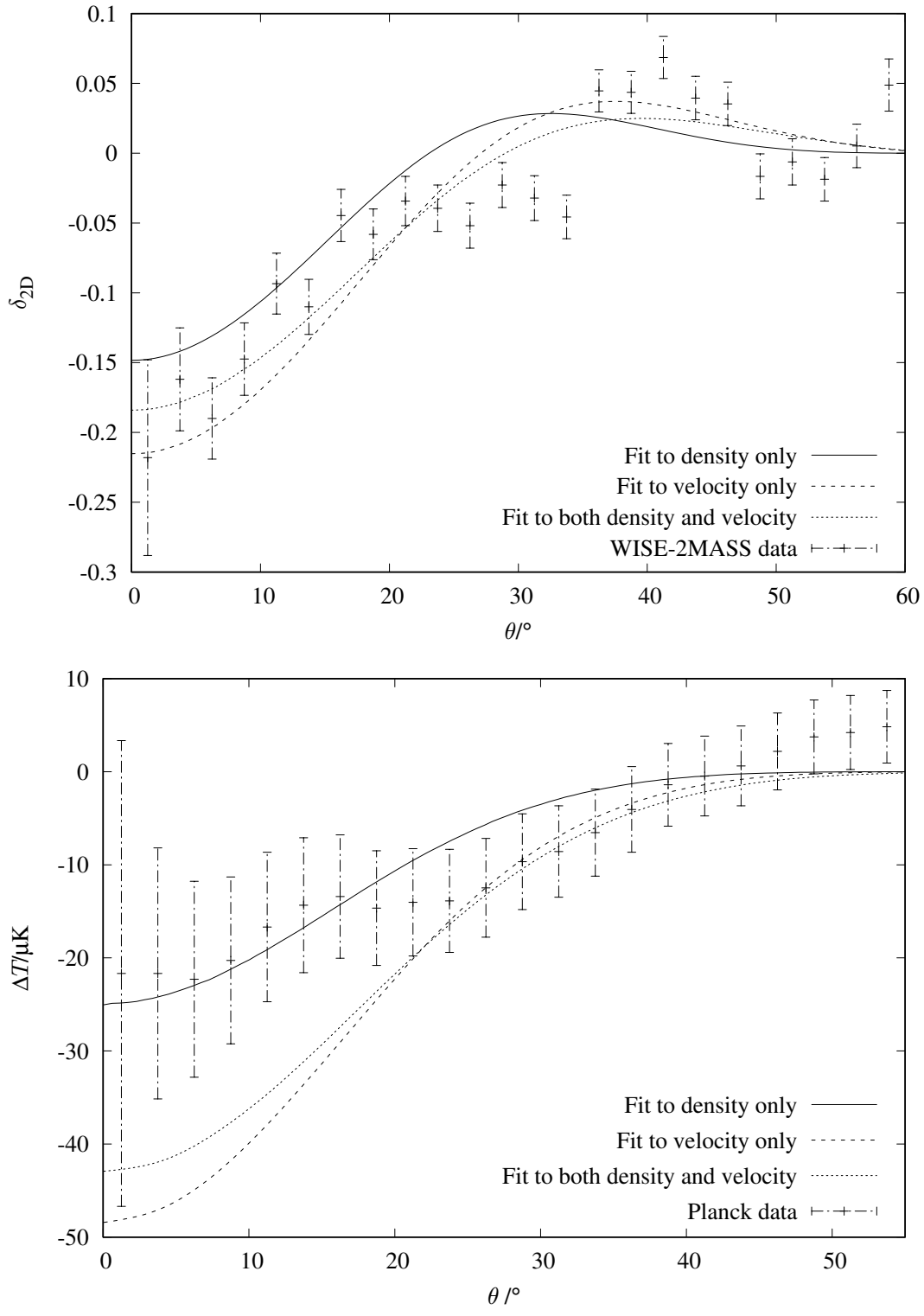

Figure 4.11: Void projected density profiles (top) and corresponding CMB temperature decrements (bottom) for our three models, compared to data from WISE-2MASS and Planck respectively. Data points are taken from FGKPS.

4.6 De-evolving the Draco void

In developing the void models investigated thus far, we have been careful to ensure consistency with the void having grown from a primordial perturbation in the early universe. This requirement is, of course, crucial in producing a physically realistic void model. Nonetheless, in this Section, we investigate the consequences of neglecting this requirement, with the purpose of demonstrating how tailoring a void to have given characteristics at the present epoch results, in general, in a physically unacceptable model.

To this end, we therefore begin by choosing the parameters R_i, a and m in our velocity perturbation at $z = 10^3$ to produce a velocity profile today that is as close as possible to that of the FGKPS void model. We then choose *different* values, say a_ρ and m_ρ, for these parameters, again at $z = 10^3$, to produce a density profile that mimics that of the FGKPS void as closely as possible. We keep the value of R_i the same in each case, so that the size of the perturbed region is consistent. We also use the same value of H_i, which ensures that the density profile remains compensated.

The resulting density and velocity profiles at the current epoch are shown in Fig. 4.12. The background Hubble parameter and the spatial extent of the perturbation are taken as $H_i = 70\ \mathrm{km\,s^{-1}Mpc^{-1}}$ and $R_i = 479h^{-1}$ Mpc, respectively. The remaining parameter values that best reproduce the FGKPS void density profile are $1 - a_\rho/H_i = -0.0342$ and $m_\rho = 2$, whereas those that best reproduce the FGKPS void velocity profile (bottom) are $1 - a/H_i = -0.0836$ and $m = 2$.

To determine the resulting CMB temperature decrement, the large spatial extent of the void means that one must again place the centre of the void at a redshift larger than $z_c = 0.15$ from the observer for the latter to reside in the external universe. We find that this can be achieved by placing the observer at a radial coordinate distance of $483h^{-1}$ Mpc, which corresponds to $z_c \sim 0.167$. The resulting CMB temperature decrement is plotted in Fig. 4.13. Interestingly, the depth of the decrement is much smaller than found for our previous void models, with a central value of just $\Delta T \approx -9.7\ \mu$K.

One may demonstrate that this void model is physically unrealistic, however, by considering the void with the present-day density and velocity profiles plotted in Fig. 4.12 and evolving it *backwards* in time. The value of the t parameter corresponding to the current epoch is 13.5 Gyr. The density contrast at a selection of earlier times is shown in Fig. 4.14. One sees that the density contrast diverges at early epochs. This occurs because the void model contains a decaying mode, which grows as one moves backwards in time. Consequently, this void model is not consistent with having grown from a primordial perturbation. This behaviour is, in fact, quite generic unless one takes care to exclude the decaying mode by choosing the initial density

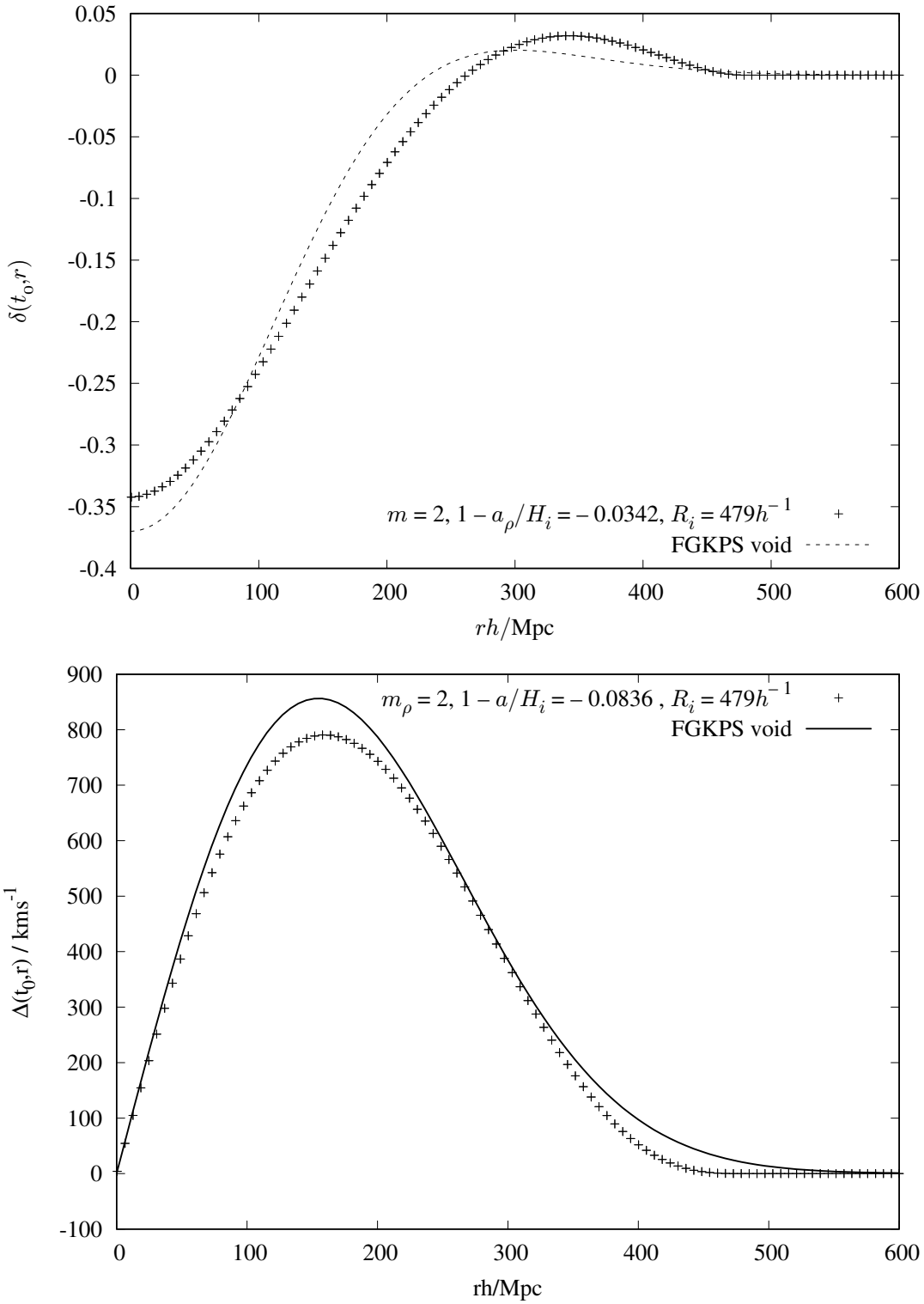

Figure 4.12: As in Fig. 4.9, but for two initial velocity perturbations at $z = 10^3$ chosen separately to reproduce the FGKPS void density and velocity profile (solid lines), respectively, as closely as possible, and without requiring the void to be consistent with having grown from a primordial perturbation.

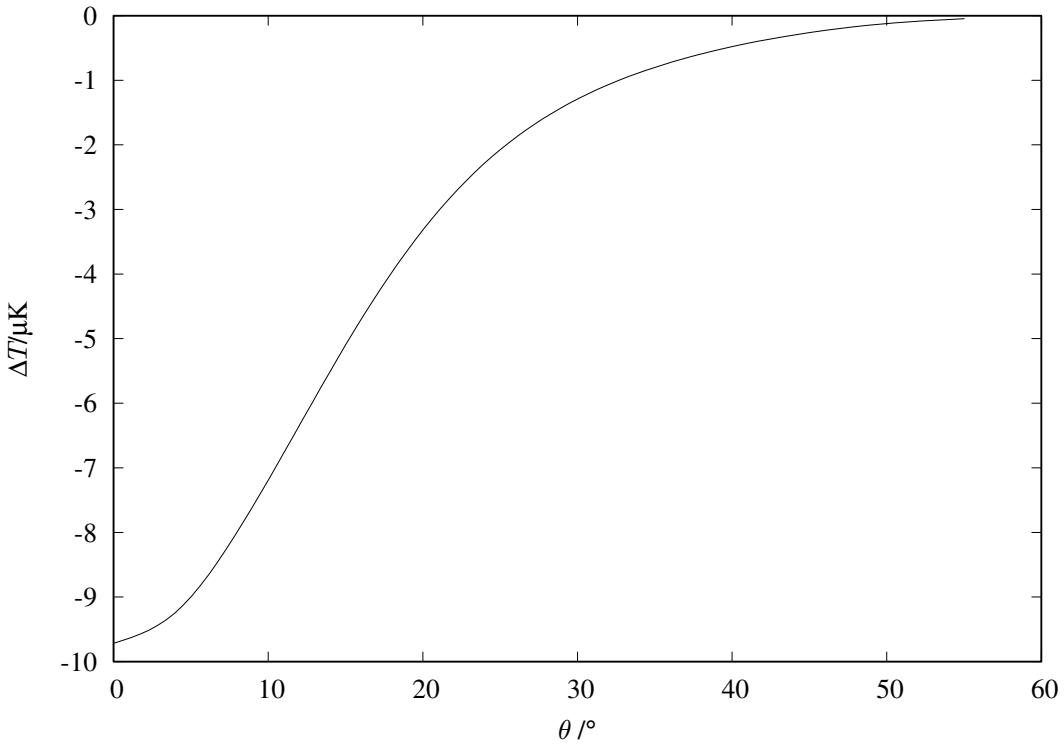

Figure 4.13: CMB temperature decrement produced by the void with the present-day density and velocity profiles plotted in Fig. 4.12.

and velocity profiles in the early universe to obey the condition (4.15).

4.7 Conclusions

We apply our tetrad-based approach for constructing spherically-symmetric solutions in general relativity to modelling voids and the secondary anisotropies that they induce in the CMB. We compare our approach to the usual LTB method, and demonstrate that the two methods represent a Eulerian and Lagrangian description, respectively, of the dynamics of a pressureless cosmological fluid.

In particular, we use our approach to construct models for the void observed in the direction of Draco in the WISE-2MASS galaxy survey, and a corresponding CMB temperature decrement in the Planck data in the same direction, and compare our void models with that produced by Finelli et al. (2016) using the LTB formalism. We find that the present-day characteristics of the void, summarised by its current density and velocity profiles, are not well constrained by the existing data, such that a large range of different void models are broadly consistent with the observations. In particular, we note that models derived from different parameterisations

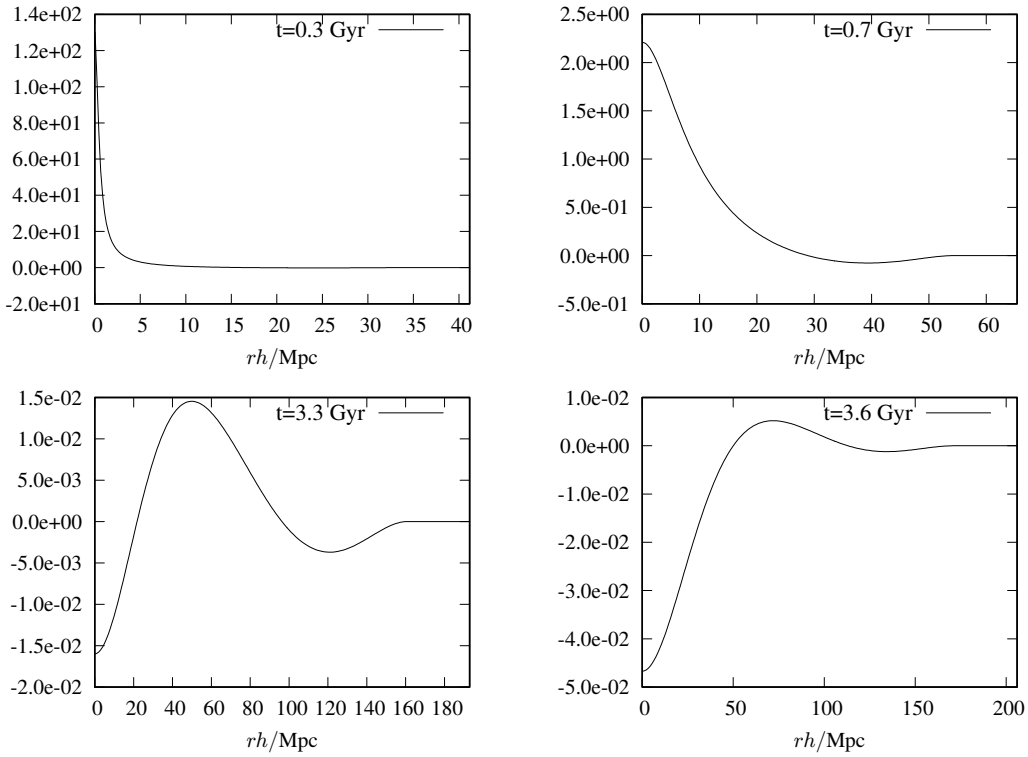

Figure 4.14: The density contrast at a selection of earlier epochs for the void with the present-day (t = 13.5 Gyr) density and velocity profiles plotted in Fig. 4.12.

of the void typically lead to very different density and/or velocity profiles. CMB temperature decrements are especially sensitive to the velocity profile; however it is often overlooked in LTB models of voids.

Finally, we demonstrate the importance of ensuring that void models are consistent with having evolved from primordial perturbations in the early universe, and hence contain no contribution from a decaying mode. In particular, we show that constructing a void model such that it has given density and velocity profiles at the present epoch will, in general, lead to unphysical singularities in the void model at earlier epochs.

Chapter 5

Effect of pressure on the evolution of perturbations

5.1 Introduction

In earlier Chapters, we modelled a generalised Swiss Cheese model with non-zero pressure and uniform density in the interior and exterior regions, and a fluid with a continuous density but zero pressure. A natural progression is to consider a fluid with continuous density, but with non-zero pressure, to see the effects that pressure has on a structure with a more realistic density profile.

Pressure effects are especially relevant when studying the early Universe. In the current understanding, perturbations created at the end of inflation act as seeds which grow into large scale structures that we see today. The overdense regions gravitationally attract matter, but this effect is countered by the outward pressure in the primordial plasma, leading to oscillatory behaviour that we term baryon acoustic oscillations (BAO) (Sakharov 1966; Eisenstein et al. 2005; Bassett & Hlozek 2010). These acoustic peaks are not only imprinted on the CMB, but are also seen in the power spectra from galaxy surveys, and serve as a useful 'standard ruler' at various redshifts as galaxies have a preferred scale at which they cluster.

Most analytic treatments of early cosmological perturbations use a planar decomposition, and use approximations for each scale (Hu & Sugiyama 1995; Hu & Sugiyama 1996; Eisenstein & Hu 1998; Montanari & Durrer 2011). As photons and baryons are tightly coupled together before recombination, they are often considered as a single, tightly coupled photon-baryon fluid.

The evolution equations are then decomposed into Fourier modes, and studied in the limits of small or large scales (Meszaros 1974; Groth & Peebles 1975; Hu & Sugiyama 1996). More recently, Slepian & Eisenstein (2016) analytically solve for the growth of a mixture of baryonic matter and photons for a transfer function that is valid at all scales, by using the approximation that the density of the mixture of fluids is constant inside the sound horizon.

In this Chapter, instead of having a mixture of fluids with varying equation of state, we instead focus on a fluid with a fixed equation of state parameter, w. Having w fixed enables us to find a fully analytic, 'spherical' wave solution of a linearised equation for perturbations, that is valid for all scales, with no approximations other than linearity. We believe that this approach is novel and of interest especially in considering the initial stages of the formation of acoustic waves.

We then employ a numerical method to solve the exact field equations and explore the behaviour in the non-linear regime. This numerical method has the advantage that it can be extended to any size of perturbation to, for example, study the non-linear evolution of a large structure, which could be compared with the pressureless approach presented in Chapter 4. In addition we compare the effects of non-linearity on the evolution of perturbations. Previous work on non-linearity often disagree on its effects on BAO. For example Cooray & Sheth (2002); Eisenstein et al. (2007) argue that systematic effects on the acoustic scale due to non-linearity are small, whereas Guzik et al. (2007); Smith et al. (2007); Angulo et al. (2008); Crocce & Scoccimarro (2008) show that more significant shifts are seen.

The structure of this Chapter is as follows. In Section 5.2 we derive the equations we use to propagate the fluid. In Section 5.3, we present the analytic solution in the linear regime, using radiation, dust and a fluid with $w = -2/3$ as examples. Next we present the numerical approach for evolving perturbations in Section 5.4. We compare the differences of the evolution of perturbations in the non-linear and linear regimes using both the analytic and numerical approaches in Section 5.5, and also examine the behaviour of perturbations when pressures are negative.

5.2 Field equations

We now express the equations in terms of physical variables that we can evolve in time. First, we can use the $L_t\rho$ equation in (1.13) and rearrange to obtain an equation for $\frac{\partial \rho}{\partial t}$.

To obtain $\frac{\partial v}{\partial t}$, where v refers to the fluid velocity and is equivalent to g_2, we use the $L_t M$ equation in (1.13). Then we can eliminate $M(t, r)$ using equation (1.14), and get rid of the $\frac{\partial g_1}{\partial r}$ using the $L_t g_1$ equation. Then we can rearrange to obtain an expression for $\frac{\partial v}{\partial t}$.

Therefore, we end up with two coupled equations for the evolution of the fluid,

$$\frac{\partial \rho}{\partial t} = -\frac{1}{f_1}\left(\frac{\partial v}{\partial r}(\rho + p) + v\frac{\partial \rho}{\partial r} + \frac{2v}{r}(\rho + p)\right), \tag{5.1}$$

$$\frac{\partial v}{\partial t} = \frac{1}{f_1}\left(-4\pi r p + \frac{1}{3}\Lambda r - v\frac{\partial v}{\partial r} + g_1 G - \frac{M}{r^2}\right) \tag{5.2}$$

To fully constrain the fluid, we can either define the density at all t and r, and then find the respective pressure and velocity profiles, assuming a mixture of baryonic gas and dark matter, giving rise to an effective equation of state as done in the generalised Swiss Cheese model in Chapter 2 and in the top-hat density model in Nandra et al. (2013). An alternative method is to assume that the fluid has some fixed equation of state parameter w, such that

$$p = w\rho. \tag{5.3}$$

In this Chapter, we choose the latter method, which has the advantage that analytic solutions can be found for linearised cases, as we shall see in Section 5.3. Then with appropriate initial conditions, the system is now wholly constrained.

5.3 Analytic approach

In the equations in (5.1) and (5.2), we can substitute for f_1, G, and g_1 by using (1.13) and (1.14) in order to express everything in terms of physical variables, which yields

$$\frac{\partial \rho}{\partial t} = \frac{1}{4\pi v r^2}\left[\frac{\partial v}{\partial r} + \left(\frac{v}{\rho + p}\right)\frac{\partial \rho}{\partial r} + \frac{2v}{r}\right]\frac{\partial M}{\partial t}, \tag{5.4}$$

$$\frac{\partial v}{\partial t} = \frac{1}{12\pi v r^4}\frac{\partial M}{\partial t}\left[\frac{1}{\rho + p}\left\{3r^2(1 + v^2) - 6Mr - \Lambda r^4\right\}\frac{\partial p}{\partial r} + 12\pi r^3 p - \Lambda r^3 + 3v\frac{\partial v}{\partial r}r^2 + 3M\right]. \tag{5.5}$$

Now we impose the equation of state, $p = w\rho$, in both equations, and replace ρ with M using the $L_r\rho$ equation. This yields two equations, which we can rearrange to obtain expressions for $\frac{\partial^2 M}{\partial t \partial r}$ and $\frac{\partial v}{\partial t}$:

$$\frac{\partial^2 M}{\partial t \partial r} = \dot{M}\left[\frac{v'}{v} + \frac{1}{1 + w}\left(\frac{2w}{r} + \frac{M''}{M'}\right)\right], \tag{5.6}$$

$$\frac{\partial v}{\partial t} = \frac{\dot{M}}{3v\left(M'\right)^2 r^2(w + 1)^2}\Big[-\Lambda M'' r^4 w + \Lambda M' r^3(w - 1) + 3v' M' v r^2(1 + w) + 3M'' v^2 r^2 w$$
$$- 6v^2 M' r w + 3\left(M'\right)^2 r w(1 + w) - 6MM'' r w + 3M'' r^2 w + 15MM' w - 6M' r w + 3MM'\Big], \tag{5.7}$$

where we have dropped the t dependencies for brevity, and dot and prime indicate partial differentiation with respect to t and r respectively.

Equation (5.6) can be integrated directly to give

$$\frac{\partial M}{\partial t} = A(t) r^{\frac{2w}{w+1}} v \left(\frac{\partial M}{\partial r}\right)^{(w+1)^{-1}}. \tag{5.8}$$

The factor $A(t)$ can be found by using the boundary condition that as $r \to \infty$, the fluid tends to the cosmological solution, i.e. that $M \to \frac{4}{3}\pi\rho_\infty(t) r^3$, $\frac{\mathrm{d}}{\mathrm{d}t}\rho_\infty(t) = -3(w+1)H(t)\rho_\infty(t)$ and $v \to rH(t)$. Hence we find that

$$A(t) = -(4\pi\rho_\infty)^{\frac{w}{w+1}}(w+1). \tag{5.9}$$

Substituting this back into equation (5.8) tells us v:

$$v = -\frac{\dot{M}}{w+1}\left(M'\right)^{-(w+1)^{-1}} (4\pi\rho_\infty(t) r^2)^{-\frac{w}{w+1}}. \tag{5.10}$$

This can then be plugged back into equation (5.7), to obtain an equation that only has M as a variable (once we plug in some expression for ρ_∞, which depends on the specific cosmology under consideration).

$$\begin{aligned}
&w(w+1)^2(\pi\rho_\infty)^{\frac{3w}{w+1}} M'' 16^{\frac{w}{w+1}} M'^{\frac{-1-2w}{w+1}} \left(-2r^{\frac{w-1}{w+1}} M - \tfrac{1}{3} r^{\frac{2+4w}{w+1}} \Lambda + r^{\frac{2w}{w+1}}\right) \\
&+ 2(\pi\rho_\infty)^{\frac{w}{w+1}} \dot{M} M'^{\frac{-2-w}{w+1}} \left(-2r^{\frac{-1-3w}{w+1}} w\dot{M} + r^{-\frac{2w}{w+1}} \dot{M}'(w+1)\right) \\
&+ \tfrac{1}{3} 16^{\frac{w}{w+1}} \Lambda (\pi\rho_\infty)^{\frac{3w}{w+1}} M'^{-\frac{w}{w+1}} (w-1)(w+1)^2 r^{\frac{3w+1}{w+1}} \\
&+ 5(\pi\rho_\infty)^{\frac{3w}{w+1}} (w+1)^2 16^{\frac{w}{w+1}} M'^{-\frac{w}{w+1}} \left(-\tfrac{2}{5} r^{\frac{w-1}{w+1}} w + r^{-2(w+1)^{-1}} (w+\tfrac{1}{5}) M\right) \\
&+ 16^{\frac{w}{w+1}} (\pi\rho_\infty)^{\frac{3w}{w+1}} w(w+1)^3 r^{\frac{w-1}{w+1}} M'^{(w+1)^{-1}} \\
&+ \pi^{\frac{w}{w+1}} r^{-\frac{2w}{w+1}} \left[(-\ddot{M}(w+1)\rho_\infty^{\frac{w}{w+1}} + \dot{\rho_\infty}\rho_\infty^{-(w+1)^{-1}} w\dot{M})(w+1) M'^{-(w+1)^{-1}} + (w-1)\dot{M}^2 M'^{\frac{-3-2w}{w+1}} M'' \rho_\infty^{\frac{w}{w+1}}\right] \\
&= 0.
\end{aligned} \tag{5.11}$$

Hence equation (5.11) can be solved to find the form for $M(t,r)$ for some fluid with an equation of state w, and the corresponding velocity profile can be found by using the expression given in (5.10).

5.3.1 Dust

We now consider the case for dust, where $w = 0$, with a $\Lambda = 0$ cosmology for simplicity.

Consider a small perturbation in the matter distribution, such that

$$M(t,r) = M_0(t,r)\left(1 + \epsilon\delta_M(t,r)\right), \tag{5.12}$$

where $M_0 = \frac{4\pi r^3}{3}\rho_\infty(t)$ is the matter distribution for a homogeneous universe, and $\epsilon \ll 1$. Note that $\delta_M(t,r)$ is different from the density contrast $\delta \equiv \frac{\delta\rho}{\rho}$ that we considered earlier. One can easily convert between these two by using

$$\delta = \epsilon\left(\delta_M + \frac{1}{3}r\frac{d\delta_M}{dr}\right). \tag{5.13}$$

For dust, the background density is given by $\rho_\infty(t) = \frac{1}{6\pi t^2}$. We substitute M in equation (5.11) with (5.12), and perform a series expansion in ϵ. To first order in ϵ, the matter perturbation must satisfy

$$12\,\frac{\partial^2\delta_M}{\partial t\partial r}rt + 9\,\frac{\partial^2\delta_M}{\partial t^2}t^2 + 4\,\frac{\partial^2\delta_M}{\partial r^2}r^2 + 6\,r\frac{\partial\delta_M}{\partial r} + 12\,\frac{\partial\delta_M}{\partial t}t - 6\,\delta_M = 0. \tag{5.14}$$

Consider dropping the r dependency in $\delta_M(t,r)$. Note that the above equation (5.14) assumes that as $r \to \infty$, the background density tends to the cosmological value, $\rho_\infty(t) = \frac{1}{6\pi t^2}$. Hence, we consider a finite region in which $\delta_M(t,r)$ is spatially homogeneous, where locally, $\delta_M(t,r) = \delta_M(t)$ is satisfied, and as r increases, the density tapers off to the background value. Note that for dust, as pressures are zero, discontinuities in density are allowed hence the it does not have to vary smoothly to the cosmological value. In this local homogeneous region, equation (5.14) above reduces to

$$3\,\frac{\mathrm{d}^2\delta_M(t)}{\mathrm{d}t^2}t^2 + 4\,\frac{\mathrm{d}\delta_M(t)}{\mathrm{d}t}t - 2\,\delta_M(t) = 0, \tag{5.15}$$

such that $\delta_M(t)$ has modes going as $t^{2/3}$ and t^{-1}, corresponding to growing and decaying modes for an inhomogeneity with uniform density for pure dust, as expected.

It turns out that equation (5.14) has an exact solution,

$$\delta_M(t,r) = F\left(\frac{r}{t^{2/3}}\right)t^{2/3} + G\left(\frac{r}{t^{2/3}}\right)\frac{1}{t}, \tag{5.16}$$

for some arbitrary functions F and G.

We can find the corresponding velocity profile by using equation (5.10). By again assuming a small perturbation in M given by (5.12), and using the form for δ_M given by (5.16), we find that to first order in ϵ, the velocity profile is given by

$$v = \frac{2r}{3t} - \left[\frac{2r}{9}F\left(\frac{r}{t^{2/3}}\right)\frac{1}{t^{1/3}} - \frac{r}{3}G\left(\frac{r}{t^{2/3}}\right)\frac{1}{t^2}\right]\epsilon + \mathrm{O}(\epsilon^2), \tag{5.17}$$

where the first term corresponds to the cosmological flow.

5.3.2 Radiation

Now we consider the case for radiation, where $w = 1/3$, again in a $\Lambda = 0$ cosmology. Following the same procedure as carried out previously for dust, we consider a small perturbation in M as given by equation (5.12), but with a background density of $\rho_\infty(t) = \frac{3}{32\pi t^2}$ corresponding to pure radiation. To first order in ϵ, the matter perturbation satisfies the following:

$$12r^2\frac{\partial^2\delta_M}{\partial t\partial r}t+12\frac{\partial^2\delta_M}{\partial t^2}rt^2+3\frac{\partial^2\delta_M}{\partial r^2}r^3-4\frac{\partial^2\delta_M}{\partial r^2}rt^2+6r\frac{\partial\delta_M}{\partial t}t-16\frac{\partial\delta_M}{\partial r}t^2-6r\delta_M=0. \quad (5.18)$$

Consider dropping the r dependency in $\delta_M(t,r)$. Note that the above equation (5.18) assumes that as $r \to \infty$, the background density tends to the cosmological value, $\rho_\infty(t) = \frac{3}{32\pi t^2}$. Hence, we consider a finite region in which $\delta_M(t,r)$ is spatially homogeneous, where locally, $\delta_M(t,r) = \delta_M(t)$ is satisfied, and as r increases, the density tapers off smoothly to the background value. Note that for radiation, unlike for dust, all variations in density must be continuous as pressures are non-zero and therefore we require the density to vary smoothly to the background value. In this local region where the density is homogeneous, equation (5.18) reduces to

$$2t^2\frac{d^2\delta_M(t)}{dt^2}+t\frac{d\delta_M(t)}{dt}-\delta_M(t)=0, \quad (5.19)$$

such that $\delta_M(t)$ has modes going as t and $t^{-1/2}$, corresponding to growing and decaying modes for an inhomogeneity with uniform density for a pure radiation fluid, as expected.

It turns out that if we transform into the coordinates

$$u=\frac{r}{\sqrt{t}}+\frac{2\sqrt{t}}{\sqrt{3}}, \quad v=\frac{r}{\sqrt{t}}-\frac{2\sqrt{t}}{\sqrt{3}}, \quad (5.20)$$

the solution to the PDE in equation (5.18) becomes

$$\delta_M(u,v)=\frac{1}{8(u+v)^2}\left(\frac{4}{u^2-v^2}\left(F(u)-G(v)\right)-\frac{1}{u}F'(u)-\frac{1}{v}G'(v)\right) \quad (5.21)$$

for some arbitrary functions F and G. Note that this is an *exact* solution of the linearised PDE given by (5.18).

We can understand the physical basis for the coordinate transformation as follows. In a radiation dominated universe, the scale factor $R(t)$ obeys

$$R=R_0\left(\frac{t}{t_0}\right)^{1/2}. \quad (5.22)$$

Written in terms of conformal coordinates,

$$\chi=\frac{r}{R}, \qquad \eta=\int\frac{dt}{R}, \quad (5.23)$$

the coordinate transformation given by (5.20) becomes

$$u = \frac{R_0}{t_0^{1/2}}\left(\chi + \frac{1}{\sqrt{3}}\eta\right), \quad v = \frac{R_0}{t_0^{1/2}}\left(\chi - \frac{1}{\sqrt{3}}\eta\right). \tag{5.24}$$

Hence, up to a multiplicative constant, the coordinates u and v are those of incoming and outgoing waves moving at sound speed $\sqrt{w} = 1/\sqrt{3}$ in conformal space, which makes sense as this is the speed at which the radiation perturbations should move.

There are several conditions that the functions F and G must satisfy for (5.21) to be physically valid. Firstly, one can express F and G as a series expansion in u and v, which are both small at early times near the origin. By plugging this in equation (5.21), we can then express this in terms of r and t, and expand in small r. It turns out that in order for the solution to be regular at $r = 0$, the functions F and G must satisfy

$$F(x) = G(-x), \tag{5.25}$$

where we use x to indicate a general argument. Note this implies the even parts in the functions F and G are equal, and odd parts of F and G are equal but have opposite signs. In addition, performing a series expansion near the origin shows that if F is even, such that F and G have the same functional form, then we result in a growing mode, and when F is odd (such that $F(x) = -G(x)$), we obtain a decaying mode.

Lastly, one must choose a function G such that $G'(v)/v$ is not singular when $v \to 0$, which corresponds to when $r \to \frac{2t}{\sqrt{3}}$.

We can choose a growing or a decaying mode by choosing the appropriate functions for F and G. The behaviour of the resulting δ_M at small r and t then determines whether it behaves like a 'growing' or 'decaying' mode. An example of a growing mode is given by choosing

$$F(u) = A\mathrm{e}^{-\frac{u^2}{2\sigma^2}}, \quad G(v) = A\mathrm{e}^{-\frac{v^2}{2\sigma^2}}, \tag{5.26}$$

which yields

$$\delta_M(t, r) = \frac{At}{32\,\sigma^2 r^3}\left(\left(r + \frac{\sqrt{3}}{2}\sigma^2\right)\mathrm{e}^{-\frac{\left(2\sqrt{3}t+3r\right)^2}{18t\sigma^2}} + \left(r - \frac{\sqrt{3}}{2}\sigma^2\right)\mathrm{e}^{-\frac{\left(2\sqrt{3}t-3r\right)^2}{18t\sigma^2}}\right). \tag{5.27}$$

This is illustrated in figure 5.1. Firstly we can see that it is a growing mode, which we can indeed verify by performing a series expansion near the origin, which shows that δ_M behaves like $\delta_M \sim \frac{A}{36\sigma^6}\, t\, \mathrm{e}^{-\frac{2t}{3\sigma^2}} + \mathrm{O}(r)$. At later times, the growing mode behaviour is overtaken by the wavelike nature of the solution, and a Gaussian pulse is seen to spread outwards, moving at coordinate speed greater than 1 (where we use units such that $c = 1$). However in conformal coordinates the wave moves out at a speed of $\frac{1}{\sqrt{3}}$. In fact, by performing coordinate transformation, we can show that we expect the wave to move at a coordinate speed of

$$v_\mathrm{s} = \frac{d\chi}{d\eta} + rH(t) = \sqrt{w} + rH(t) \tag{5.28}$$

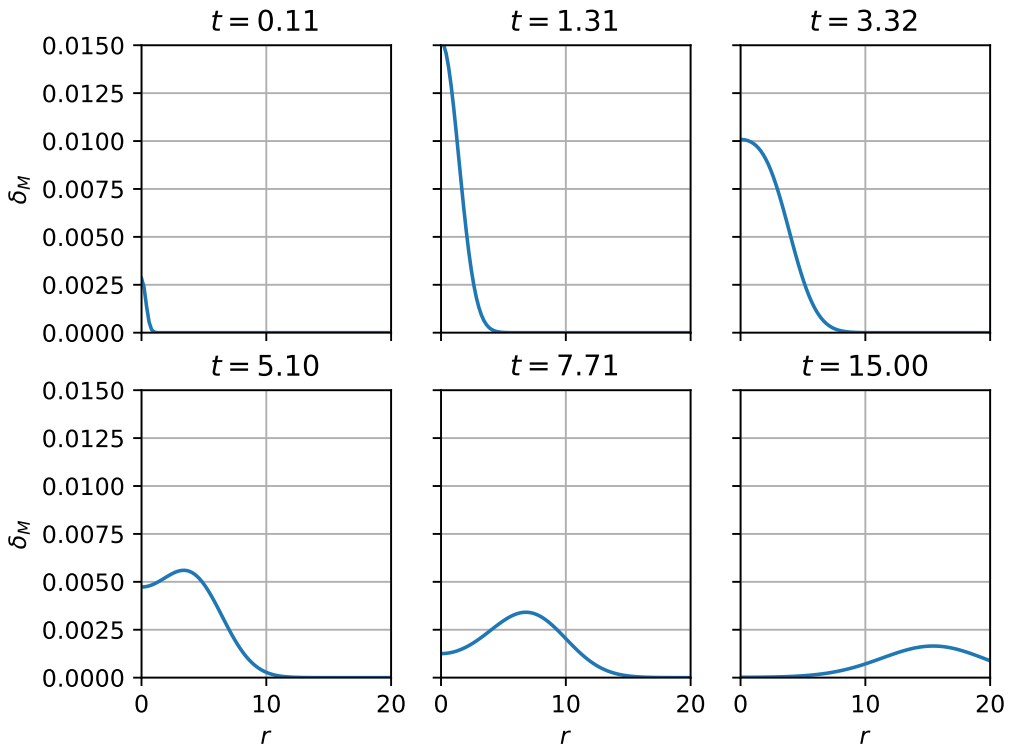

Figure 5.1: Growth of a small matter perturbation given by choosing even functions for F and G, given by (5.26), with parameters $A = \sigma = 1$. One can see that the growing mode behaviour dominates at small t. At later times the wavelike nature dominates and one can see from above that the perturbation propagates away at a coordinate speed that is slightly larger than c (which is equal to unity in our units). The absolute units of r and t are arbitrary.

for a fluid with some equation of state w, as we expect the fluid to propagate at a sound speed of $\sqrt{w}$ in conformal coordinates.

A decaying mode can be found by, for example, choosing

$$F(u) = Au^3 \exp\left(-\frac{u^2}{2\sigma^2}\right), \quad G(v) = -Av^3 \exp\left(-\frac{v^2}{2\sigma^2}\right) \tag{5.29}$$

(note that choosing $F(u) = Au \exp\left(-\frac{u^2}{2\sigma^2}\right)$ results in $G'(v)/v$ being singular at $v = 0$, hence is not a valid choice for F), which yields

$$\delta_M = \frac{\sqrt{3}A}{96\sqrt{t}\sigma^2 r^3}\Big[\left\{\left(\tfrac{4}{3}\sigma^2t^3 + r^4 + 4r^2t^2\right)\sqrt{3} + \left(\tfrac{3}{2}\sigma^2 + 6t\right)r^3 + \tfrac{8}{3}t^3 r\right\} \mathrm{e}^{-\frac{(2\sqrt{3}t+3r)^2}{18t\sigma^2}} - \left\{\left(\tfrac{4}{3}\sigma^2t^3 + r^4 + 4r^2t^2\right)\sqrt{3} - (\tfrac{3}{2}\sigma^2 + 6t)r^3 - \tfrac{8}{3}t^3 r\right\} \mathrm{e}^{-\frac{(2\sqrt{3}t-3r)^2}{18t\sigma^2}}\Big]. \tag{5.30}$$

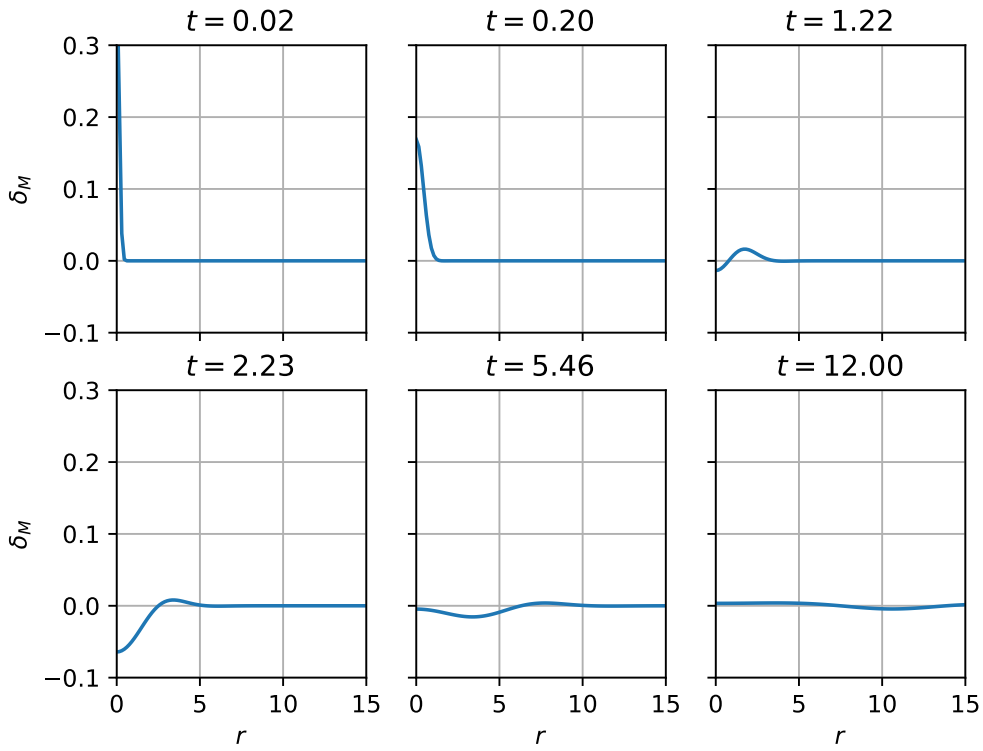

Figure 5.2: Evolution of matter perturbation given by choosing an odd function for F and G, as given by equation (5.29), with parameters $A = \sigma = 1$. At small t the decaying mode behaviour is dominant. At later times, the wavelike takes over, as seen in the growing mode.

Near the origin it behaves $\delta_M = \frac{A(81\sigma^6+324\,t\sigma^4-432\,\sigma^2t^2+64\,t^3)\sqrt{3}}{2592\,\sigma^6\sqrt{t}}\mathrm{e}^{-\frac{2t}{3\sigma^2}} + \mathrm{O}(r^2)$. Hence at small t, it goes as $t^{-1/2}$ as expected, and one can verify this behaviour from figure 5.2 that it does indeed start as a singularity at small t which decays away. At later times, the wavelike nature dominates as seen in the growing mode, and propagates away. For a realistic modelling of a perturbation, one must make sure that there are no components corresponding to the decaying mode.

These solutions are very interesting in the context of baryon acoustic oscillations. In the early universe, the Universe is radiation-dominated and the small perturbations propagate as waves. This oscillatory behaviour is often illustrated by using plane wave solutions for a specific wavevector k. The exact spherical waves that we have shown make it easier to envision these fluctuations that propagate at some speed which falls with time as the universe moves from ionized to neutral, and then stalls as the equation of state falls to near zero, at a characteristic radius (Sakharov 1966; Eisenstein et al. 2005; Bassett & Hlozek 2010). Recently Slepian

& Eisenstein (2016) analytically find the transfer function that encapsulates the growth of a mixture of baryonic matter and photon, that is valid at all scales. The advantage of this method is that a mixture of fluids with a varying effective equation of state can be considered, but it cannot produce an exact spherical solution as considered in this section and is limited to the approximation that the density of fluids is constant inside the sound horizon.

5.3.3 Negative pressure: $w = -2/3$ fluid

Here we consider a fluid with negative pressure - specifically, with $w = -2/3$, again in a $\Lambda = 0$ cosmology. Following the same procedure as carried out for dust and radiation, equation (5.11) becomes

$$12r^2\frac{\partial^2\delta_M}{\partial t\partial r}t+3\frac{\partial^2\delta_M}{\partial t^2}rt^2+12\frac{\partial^2\delta_M}{\partial r^2}r^3+2\frac{\partial^2\delta_M}{\partial r^2}rt^2+24r\frac{\partial\delta_M}{\partial t}t+54\frac{\partial\delta_M}{\partial r}r^2+8\frac{\partial\delta_M}{\partial r}t^2+30r\delta_M = 0, \tag{5.31}$$

where we have used the background density for an EdS universe, $\rho_\infty(t) = \frac{1}{6\pi(w+1)^2t^2} = \frac{3}{2\pi t^2}$.

Consider dropping the r dependency in $\delta_M(t,r)$. Note that the above equation (5.31) assumes that as $r \to \infty$, the background density tends to the cosmological value, $\rho_\infty(t) = \frac{3}{32\pi t^2}$. Hence, we consider a finite region in which $\delta_M(t,r)$ is spatially homogeneous, where locally, $\delta_M(t,r) = \delta_M(t)$ is satisfied, and as r increases, the density tapers off smoothly to the background value. Note that for this fluid, as pressures are non-zero, all variations in density must be continuous, as was the case for radiation. In this local region where the density is homogeneous, the equation above reduces to

$$\frac{d^2\delta_M(t)}{\mathrm{d}t^2}t^2 + 8\frac{d\delta_M(t)}{dt}t + 10\delta_M(t) = 0, \tag{5.32}$$

such that $\delta_M(t)$ has modes going as t^{-2} and t^{-5}, such that there are no growing modes.

Trying the following substitution

$$u = \frac{r}{t^2} - \sqrt{\frac{2}{3}}\frac{i}{t}, \quad v = \frac{r}{t^2} + \sqrt{\frac{2}{3}}\frac{i}{t} \tag{5.33}$$

gives us the solution

$$\delta(u,v) = -\frac{(u-v)^3}{8(u+v)^2}\left[-\frac{1}{u}\frac{\mathrm{d}F(u)}{\mathrm{d}u} + \frac{1}{v}\frac{\mathrm{d}G(v)}{\mathrm{d}v} + 4\left(F(u)+G(v)\right)\right]. \tag{5.34}$$

for some arbitrary functions F and G.

One can note that, as for radiation, the new coordinates u and v satisfy

$$u \propto \chi + \sqrt{w}\eta, \quad v \propto \chi - \sqrt{w}\eta, \tag{5.35}$$

such that they are, up to a multiplicative constant, those of incoming and outgoing 'waves' moving at speed $\sqrt{w} = \sqrt{\frac{2}{3}}i$ in conformal space, where the sound speed here is now imaginary.

By performing a series expansion in small r, one can show that in order for δ_M to be regular at the origin, the functions F and G must satisfy

$$F(x) = -G(-x) \tag{5.36}$$

and the even parts of F and G must be wholly imaginary for δ_M to be real. One can also show by examining the behaviour at small t and r that it is impossible to choose a stable 'growing mode' i.e. one where δ_M is small as $t \to 0$, and is well behaved at some finite t, at least for perturbations at sub-horizon scales which we are considering here. The interesting consequence of this is discussed further below in Section 5.5.2.

5.4 Numerical approach

In this Section, we examine how we can solve the system exactly (i.e. not using linear approximations), by using a numerical approach. The motivation for solving the system numerically is to enable comparisons with behaviour of perturbations in the linear regime. It is also useful to have a numerical framework for evolving perturbations until later times when often perturbations become non-linear, to be able to calculate the effect of the inhomogeneity on a photon, to e.g. quantify the ISW effect, in a system with pressure. In addition, non-linear effects are normally ignored when studying the imprint of BAOs on late-time matter power spectrum (Montanari & Durrer 2011), which may account for up to 5% error in the estimation of the location of peaks in the matter power spectrum (Montanari & Durrer 2011).

Unlike in the case with dust, we cannot reduce the fluid equations (5.1) and (5.2) to a set of first order differential equations that we can simply evolve with time. Hence, to evolve the PDEs, we use the finite difference method, over a finite spatial domain. The finite difference scheme is a method to numerically solve PDEs that involves discretising the spatial and temporal domain into a finite grid.

We can find M by integrating ρ spatially, using the $L_r M$ equation. However, more accurate results can be obtained by instead evolving M, alongside ρ and v, by using the $L_t M$ equation to obtain an expression for $\frac{\partial M}{\partial t}$, and replacing $\partial M/\partial r$ with ρ using the $L_r M$ equation. Finally we impose the equation of state to replace p with ρ in all three PDEs. Hence the system of

PDEs that we aim to solve are made of three coupled equations,

$$\frac{\partial \rho}{\partial t} = -\frac{1}{f_1}\left[\left(\frac{\partial v}{\partial r} + \frac{2v}{r}\right)(1+w)\,\rho + v\frac{\partial \rho}{\partial r}\right],$$
$$\frac{\partial v}{\partial t} = \frac{1}{f_1}\left(-4\pi r w \rho + \frac{1}{3}\Lambda r - v\frac{\partial v}{\partial r} + g_1 G - \frac{M}{r^2}\right),$$
$$\frac{\partial M}{\partial t} = -\frac{1}{f_1}4\pi v r^2 (w+1). \tag{5.37}$$

(5.38)

Once we have the density and velocity profiles at some time $t = t_*$, we can find $\frac{\partial \rho}{\partial r}$ and $\frac{\partial v}{\partial r}$ on this time slice using simple differencing.

Next, we can obtain g_1 by using equation (1.14). As we know g_1, we can then find G using the $L_r p$ equation,

$$G = -\frac{g_1 \frac{\partial p}{\partial r}}{\rho + p}. \tag{5.39}$$

Next we find an expression for f_1. By rearranging the $L_t \rho$ equation, we can find that

$$f_1 = -\left[\left(\frac{2v}{r} + F\right)(\rho + p) + v\frac{\partial \rho}{\partial r}\right]\left(\frac{\partial \rho}{\partial t}\right)^{-1}. \tag{5.40}$$

We can eliminate p using the equation of state, and v by using equation (5.10), to find the following:

$$f_1 = \left(\frac{\rho}{\rho_\infty}\right)^{\frac{w}{w+1}}. \tag{5.41}$$

Hence we have a method for obtaining all the variables needed to evaluate the evolution equations (5.38) at some time. However, before embarking on solving the system of equations numerically, we first need to choose the appropriate initial and boundary conditions. The initial conditions are specified by choosing the density and velocity profiles, $\rho(t_i, r)$ and $v(t_i, r)$ at the initial time t_i, from which the mass profile, $M(t_i, r)$ can be determined. To model a realistic perturbation, we choose a density profile and the corresponding velocity profile that are given by those in Section 5.3. For example, to model a radiation fluid, we choose the density profile for a growing mode, such as one given by equation (5.27), taking care to convert δ_M to the density contrast, δ, first.

We now consider the appropriate boundary conditions at either ends of the spatial boundary, $r = 0$ and $r = r_{\max}$. First we found that starting the spatial grid from $r = 0$ causes instabilities at the origin which propagate over time. To mitigate this, we shift all cells spatially by half of a grid width, such that the first cell spans the range of r from $\Delta r/2$ to $3\Delta r/2$, where Δr is the width of one cell.

To impose the correct boundary conditions at the origin, we examine the behaviour of the quantities at small r. First we perform a power expansion for M. As long as ρ is not singular at the origin, the dominant behaviour near the origin should be $\propto r^3$; hence we can express M as

$$M = f_3(t)r^3 + f_4(t)r^4 + f_5(t)r^5 + f_6(t)r^6 + f_7(t)r^7 + O(r^8). \tag{5.42}$$

We can use this expression in equation (5.11) and again expand in r. Each term in r must obey the equation, and one can easily show that all the terms with even powers of r in (5.42) are zero, such that

$$M = f_3(t)r^3 + f_5(t)r^5 + f_7(t)r^7 + O(r^9). \tag{5.43}$$

Hence it follows from the $L_r M$ equation that ρ must also be an even function near the origin; i.e.

$$\rho = \frac{1}{4\pi}\left(3f_3(t) + 5f_5(t)r^2 + 7f_7(t)r^4\right) + O(r^6) \tag{5.44}$$

Similarly, we can then find the behaviour of v at small r by substituting M with (5.42) in equation (5.10) and expanding in r. It turns out that v must be an odd function around small r. For example, for radiation, v is given by

$$v = -2^{\frac{3}{4}}\sqrt{t}\left(\frac{\dot{f_3}(t)}{4f_3(t)^{\frac{3}{4}}}r + \frac{4\dot{f_5}(t)f_3(t) - 5\dot{f_3}(t)f_5(t)}{16f_3(t)^{\frac{7}{4}}}r^3\right) + O(r^5). \tag{5.45}$$

We use these conditions to determine an 'extra' point at the inner boundary, hence enabling us to calculate spatial derivatives of the variables at the innermost point accurately.

At the outer boundary, we use the last four cells at the boundary to perform a series expansion to third order to predict the value of the variables at a grid point that is one step beyond the boundary, which again we can use to calculate spatial derivatives with sufficient accuracy for our system of first-order PDEs.

Hence we have three coupled first-order partial differential equations that we evolve in time. Our initial method for the time evolution was to use Euler's method, where one evaluates all of the variables at one time slice in order to find the time derivatives of the variables one is evolving, and use these to march forward by one time step. Unfortunately we encountered numerical instabilities with this method. Another option is to use the Lax-Friedrichs method, which is also of order one but more stable. However this method produced a spurious solution; hence we employ the 4th order Runge-Kutta integration technique. This involves evaluating the variables and hence the time derivatives at several points in the time interval to obtain the most accurate increment over the time step.

Lastly, we note that the finite difference method is subject to the Courant-Friedrichs-Lewy condition (Courant et al. 1928), namely that it is necessary for the ratio $\Delta r/\Delta t$ to remain higher than the fluid velocity for convergence. The condition ensures that the scheme has enough

time for the information from one element to propagate to the next mesh point. We ensure this condition is met by choosing the spatial and temporal grid sizes such that their ratio $\Delta r/\Delta t$ is higher than the largest fluid velocity in the system at all time slices.

5.5 Results

5.5.1 Linear and non-linear waves: radiation

In this Section, we examine the behaviour of perturbations in the linear regime and the non-linear regime, using a pure radiation fluid with $\Lambda = 0$ as an example. First, we focus on the linear regime. We start off with a small perturbation of amplitude $\delta_0 \sim 0.017$, where the initial density perturbation at $t_i = 0.02$ is given by the pure growing mode in equation (5.27). The corresponding initial velocity perturbation is found using (5.10). The perturbation is evolved using the numerical approach and we compare this to the prediction from the linear analytic solution, in figure 5.3. One can see that when the perturbation is very small, the analytic solution of the linearised equations and the numerical approach agree very well.

Next we examine the behaviour in the non-linear regime. In this regime, we expect the analytic approach to be inaccurate, as it is a solution for linearised field equations. We start with a perturbation of amplitude $\delta_0 \sim 1.2$, with a profile consisting of a purely growing mode, again given by equation (5.27). Interestingly, one can see from figure 5.4 that the linear approach greatly underestimates the growth of the perturbation at early times.

Next we examine how the wave speeds change in the non-linear regime. In the linear regime, we expect the waves to propagate at sound speed $\sqrt{w}\ v_s = \sqrt{w} + rH(t)$ (from equation (5.28)) in our 'physical' coordinates. However we expect this relation to break down when the oscillations are non-linear.

In fact we find that non-linear radiation waves travel faster than in the linear regime. Figure 5.5 we compare the speed of the non-linear wave compared to the expected speed for a linear wave. The speed was found by measuring the speed of the peak of the wave, for different magnitudes of a Gaussian perturbation. The background density was kept the same at the time of measurement.

It is of interest to compare these with ocean waves, to see if we can see analogous effects. It is known that waves on shallow water surfaces can be modelled using the Korteweg-de Vries (KdV) equation (Thorne & Blandford 2017). A soliton is a non-linear solitary wave pulse that maintains its shape as it travels. The KdV equation can be solved for a soliton and it is found that the soliton travels at a speed given by (Thorne & Blandford 2017)

$$v = \sqrt{g h_0}\left(1 + \frac{\xi_0}{2h_o}\right), \tag{5.46}$$

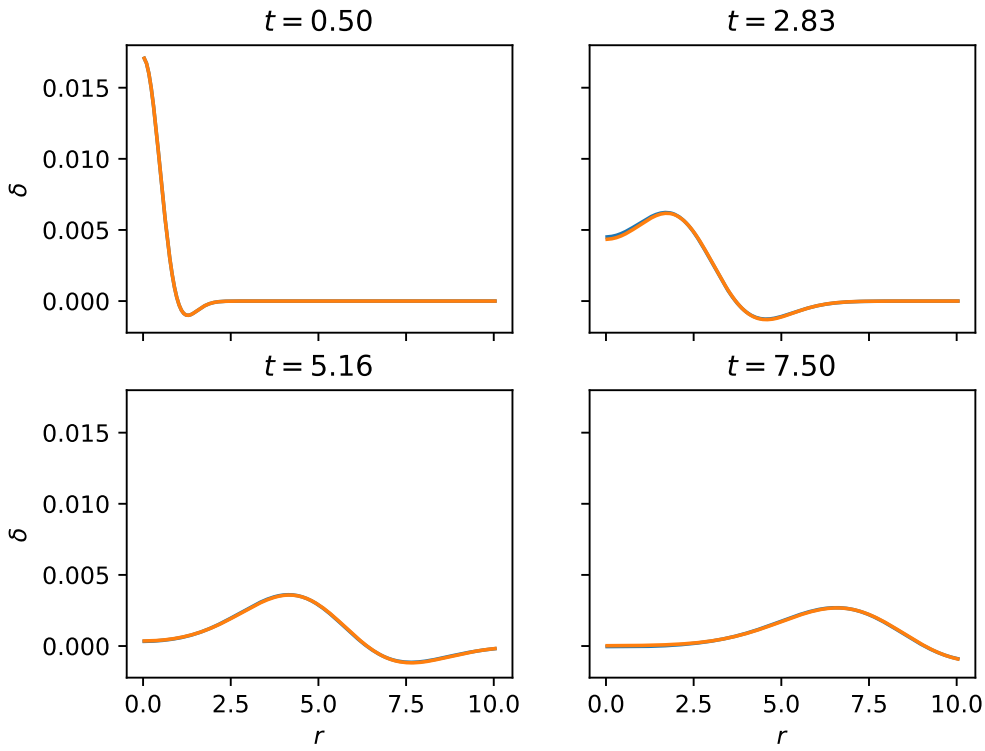

Figure 5.3: Evolution of a perturbation of a pure radiation fluid in the linear regime, using the analytic (orange) and numerical approach (blue). The initial conditions consist of a purely growing mode given by equation (5.27), with parameters $A = 1.0$, $\sigma = 1.0$ and $\epsilon = 0.3$. The two methods agree almost exactly.

where h_0 is the depth of the undisturbed water, ξ_0 is the wave amplitude and g is the gravitational acceleration. The first term is the wave speed of a linear wave, and the second term is the non-linear correction, which is proportional to the wave amplitude. Interestingly, the non-linear correction in the wave speed of radiation perturbations has a linear relationship with the amplitude (density contrast), similar to non-linear waves in water.

It would be interesting in the future to extend the results above to examine the effect on the acoustic signature due to non-linearity.

5.5.2 Fluids with negative pressure

Negative pressure is often under consideration in cosmology. As dark energy causes accelerated expansion, it is a common practice to model dark energy as a fluid with a constant or varying equation of state that is allowed to be negative (Chevallier & Polarski 2001; Linder 2003; Jassal et al. 2005; Feng & Lu 2012), whereby the negative pressure leads to repulsive gravitational

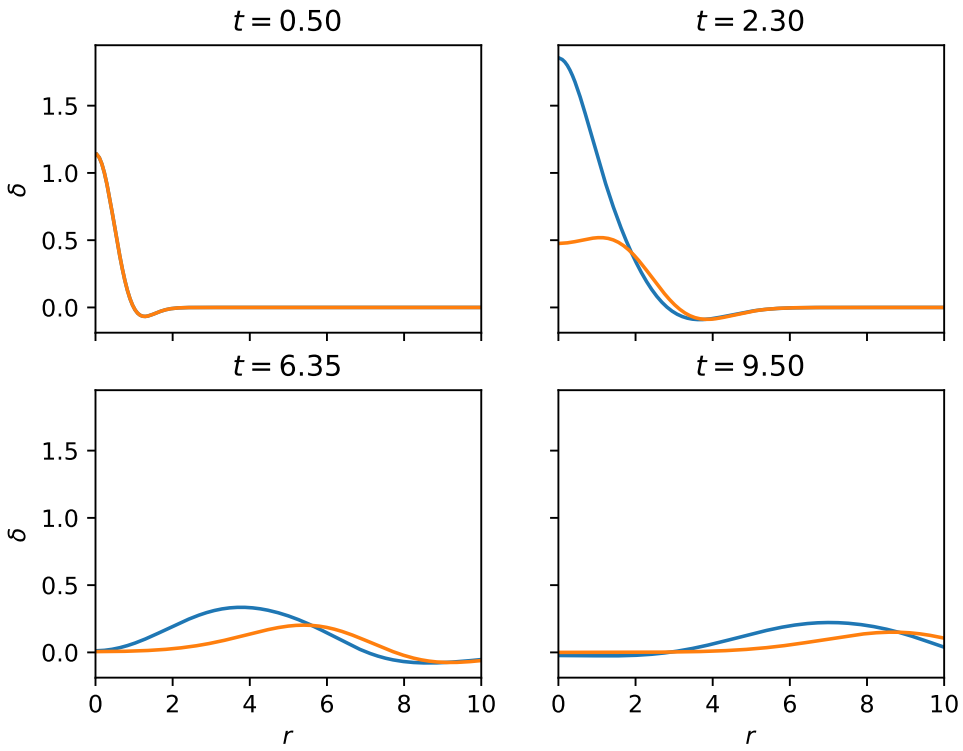

Figure 5.4: Evolution of a perturbation of a pure radiation fluid in the non-linear regime, obtained via the analytic approach (orange) and the numerical approach (blue). In this case, the linearised predictions underestimate the growth of the perturbation at early times. Used a purely growing mode given by equation (5.27), with parameters $A = 100.0$, $\sigma = 1.0$ and $\epsilon = 0.2$.

force. Often a mixture of baryonic matter and dark energy can be represented as a single fluid with an effective equation of state parameter $w < 0$. More exotic examples include cosmic strings and domain walls, which have an effective equation of state $p = -1/3\rho$ and $p = -2/3\rho$, respectively. It has been argued that these could support the formation of structure in the Universe (Vilenkin & Shellard 2000; Fabris & Goncalves 2000).

Therefore in the following subsection, we explore the behaviour of fluids when the equation of state parameter $w < 0$. We find that the behaviour varies depending not only on the value of w but also the scale of the perturbation.

5.5.2.1 Case 1: $-1 < w < 0$

When $w < 0$, we have an interesting fluid that has negative pressure. In a fluid, the effect of pressure is two-fold; firstly, it contributes to the energy density of the fluid and hence to the gravitational effects along with mass. Secondly, the pressure gradient exerts a force that causes

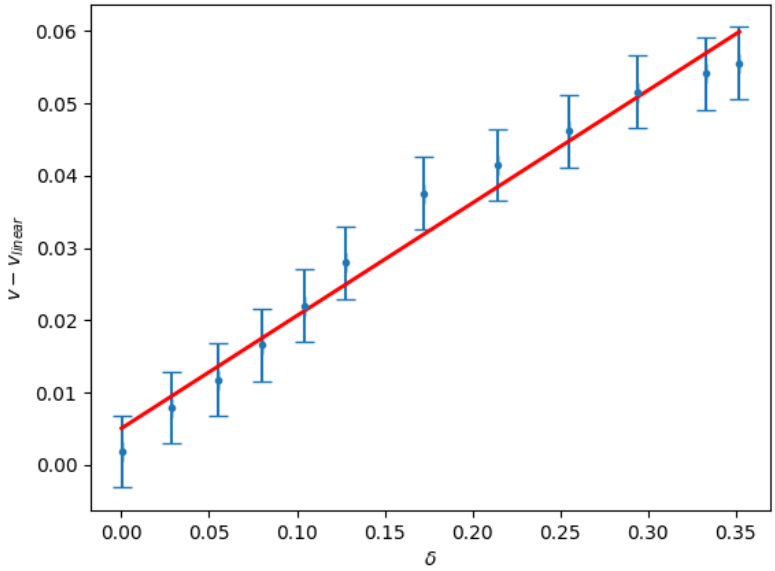

Figure 5.5: The difference between speed of non-linear waves and the expected speed for a linear wave, in units of c, starting from a Gaussian perturbation in density at the initial time. Linear regression shows a straight line fit with gradient = 0.156 ± 0.008, intercept = 0.005 ± 0.002.

the motion of a fluid particle to deviate from a geodesic. In a normal fluid with $w > 0$, such as radiation, the pressure gradient opposes the effect of a gravitational force. Hence, when the perturbation is within the horizon, these competing forces result in an oscillation, as we have seen in radiation. When the perturbation is outside the horizon, pressure effectively no longer has an effect, as the causal physical processes cannot occur. Therefore the perturbations are 'frozen in' and simply grow with time, which is indeed what we see in our set up.

However when $w < 0$, firstly the negative pressure reduces rather than adds to the gravitational force, and secondly, the pressure gradient enhances the effect due to gravity; therefore we expect to not see any oscillations. In fact, it is known that when a fluid has negative pressure such that $-1 < w < 0$, we expect a large growth of density perturbations at small wavelengths, as pressure gradient and gravity both act to increase the magnitude of any perturbations (Fabris & Martin 1997). Fabris & Martin (1997) demonstrate using a linear treatment that when the wavelength of a perturbation is within the horizon, instead of oscillatory behaviour, it behaves exponentially, such that it does not grow in a stable manner. We test this behaviour, using an initial Gaussian perturbation in the density, and simply a cosmological flow for the velocity,

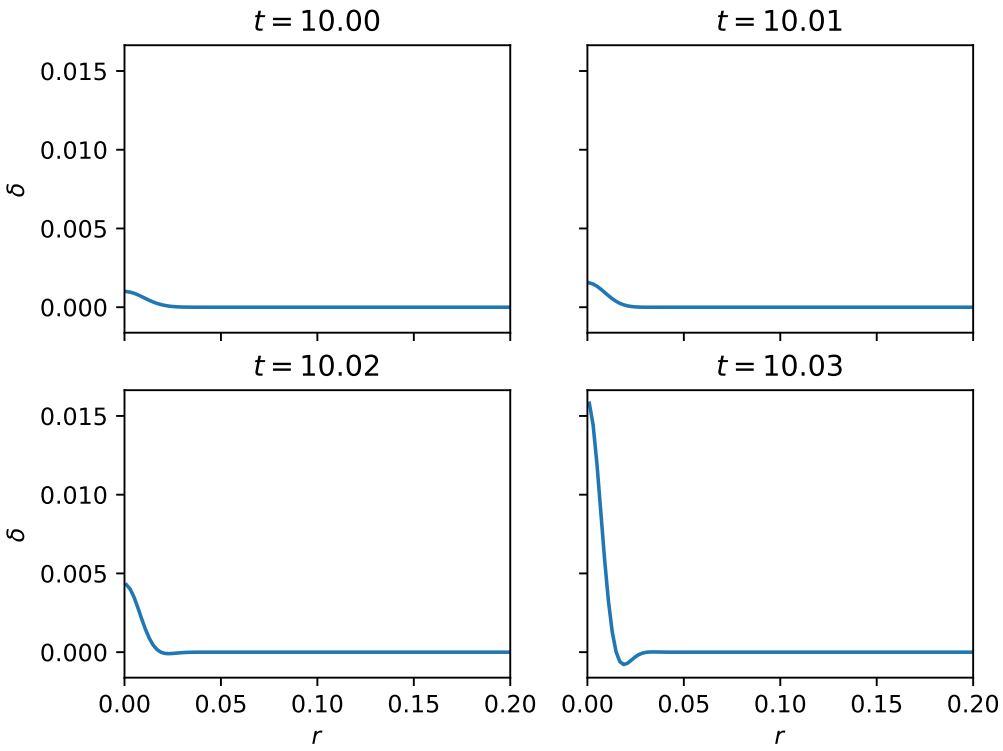

Figure 5.6: Evolution of a fluid with $w = -1/3$, consisting of a small scale perturbation whose initial conditions are given by a Gaussian perturbation in density (equations (5.47)), with parameters $\delta_0 = 0.001$ and $\sigma = 0.01$, from initial time $t_i = 10$. Gravity and negative pressure effects both lead to rapid growth of any perturbations.

such that

$$\begin{aligned} \delta(t_i, r) &= \delta_0 \mathrm{e}^{-\frac{r^2}{2\sigma^2}}, \\ v(t_i, r) &= r H_i, \end{aligned} \tag{5.47}$$

with $w = -1/3$. At the initial time $t_i = 10$, the Jeans length is given by $\lambda_J = c_s\sqrt{\frac{\pi}{\rho}} \approx 29.6$, where the sound speed, c_s, is given by $c_s^2 = |w|$. The perturbation indeed displays instabilities, as shown in figure 5.6, consistent with exponential growth.

However when the wavelength is large such that it greatly exceeds the Jeans length, Fabris & Martin (1997) show that in the linear regime, when $w < 0$, the perturbation contains two modes, which behave as

$$\delta = A_1|\eta|^2 + A_2|\eta|^{2\frac{-1+3w}{1+3w}} \tag{5.48}$$

where η is conformal time, and A_1 and A_2 are constants. Expressed in terms of t, this becomes

$$\delta = B_1 t^{\frac{2+6w}{3+3w}} + B_2 t^{\frac{-2+6w}{3+3w}} \tag{5.49}$$

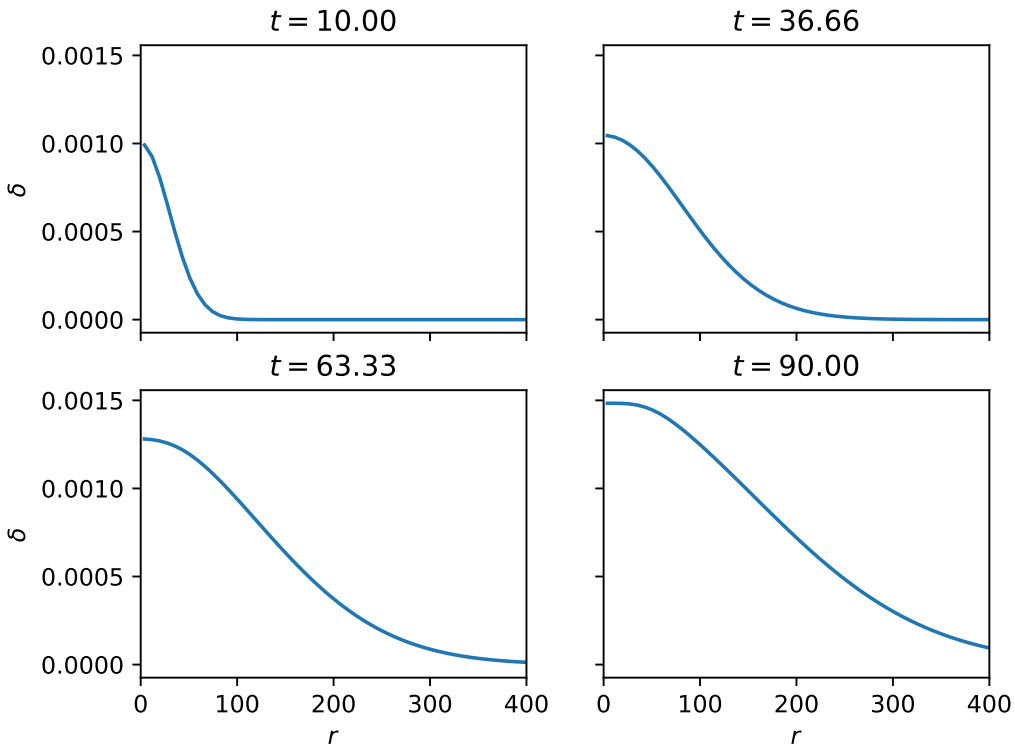

Figure 5.7: Evolution of a fluid with $w = -1/6$, consisting of a large scale perturbation whose initial conditions are given by a Gaussian perturbation in density (equations (5.47)), with parameters $\delta_0 = 0.001$ and $\sigma = 30$, from initial time $t_i = 10$. The wavelength of the perturbation exceeds the Jeans length, $\lambda_J = 26.2$.

where B_1 and B_2 are constants. One can show that when $-1/3 < w < 0$, the first term is a growing mode, which behaves in the same way as when $w > 0$. For example, when $w = -1/6$, the two modes above can be expressed as $\delta = At^{2/5} + Bt^{-6/5}$. One can indeed see the growing mode behaviour in figure 5.7, where the perturbation grows and is well behaved.

Physically, at large scales the pressure gradient has no time to influence the perturbation. Hence only the gravitational terms have an influence. To understand this physically, one can derive the relativistic form of Poisson's equation, by considering the weak field limit, $g_{\mu\nu} \approx \eta_{\mu\nu} + h_{\mu\nu}$, and using the 00−component of Einstein's equations, to find

$$\nabla^2 \Phi = 4\pi \left(\rho + 3p\right) . \tag{5.50}$$

where Φ is the gravitational potential. Hence, when $-1/3 < w < 0$, $\rho + 3p > 0$, and the negative pressure reduces the magnitude of gravitational force but it is still attractive. Hence we can conclude that at large scales, gravity 'wins' over the pressure, supporting the growth of the perturbation.

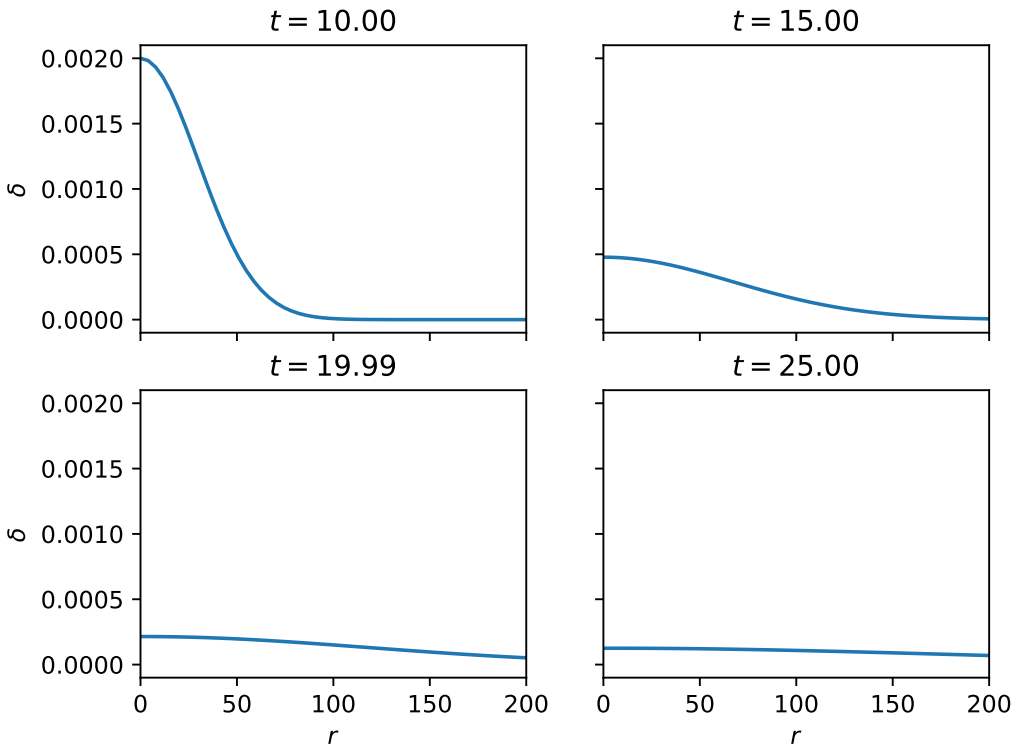

Figure 5.8: Evolution of a fluid with $w = -2/3$, consisting of a large scale perturbation whose initial conditions are given by a Gaussian perturbation in density (equations (5.47)), with parameters $\delta_0 = 0.002$ and $\sigma = 30$, from initial time $t_i = 10$. The wavelength of the perturbation exceeds the Jeans length, $\lambda_J = 20.9$.

When $w < -1/3$, the behaviour is different. One can show that both terms in equation (5.48) become decaying modes for these fluids. Indeed, we can see this behaviour in figure 5.8, where we use a fluid with $w = -2/3$ as an example. Therefore we conclude that all perturbations decay away when $w < -1/3$ and the fluid does not support growth of structure at large scales. Physically, $\rho + 3p < 0$ in this case, and as one can see from equation (5.50), the negative pressure 'wins' over the mass, causing an overall repulsive gravitational effect. This result is also consistent with the fact that one cannot find a well-behaved 'growing mode' using the analytic approach, as discussed in Section 5.3.3.

5.5.2.2 Case 2: $w = -1$

Let us now consider the case when w is exactly equal to -1. Going back to the $L_r p$ equation, we see that

$$g_1 \frac{\partial p}{\partial r} = -G(\rho + p) = 0 \tag{5.51}$$

Hence the LHS must equal zero. As g_1 cannot be zero at all space and time, we conclude that $\frac{\partial p}{\partial r} = 0$, and that the fluid cannot support any perturbations in pressure and hence density. We can interpret this 'fluid' with $w = -1$ as essentially a universe with pure cosmological constant only, which cannot contain perturbations.

5.5.2.3 Case 3: $w < -1$

Next we consider the regime where the equation of state parameter $w < -1$, also known as 'phantom energy'. Phantom energy is a candidate for dark energy. It is well known that phantom energy violates the weak energy condition (Carroll et al. 2003). It has been argued that phantom energy suffers from vacuum instability, as it has negative kinetic energy and hence negative mass; this implies it is possible for it to decay into a large number of negative and positive mass particles whilst conserving energy. Nevertheless, it may be possible to have a phenomenologically viable model of phantom energy if, for example, one considers it as an effective field theory valid until a certain momentum cut-off (Carroll et al. 2003).

It is noteworthy therefore that current observations do not rule out a phantom dark energy, especially if w is allowed to vary in time. The present-day value of w for dark energy assuming a perfect fluid and a flat universe has been found to be $w = -1.006 \pm 0.045$ by Planck in 2015 (Planck Collaboration et al. 2016).

For a universe composed only of a fluid with equation of state parameter w only, the density is related to the scale factor, a, by

$$\rho \propto a^{-3(1+w)}. \tag{5.52}$$

Hence when $w < -1$ we have an interesting and counter-intuitive fluid, where the energy density *increases* as the universe expands.

In our set-up where we only consider the fluid dynamics of the system, a fluid with $w < -1$ has the same behaviour as that which has $-1 < w < -1/3$, such that instabilities occur at small scales and perturbations are smoothed out at large scales, as seen in figure 5.9. Hence the fluid cannot support structure growth at all scales.

Note that in an EdS universe with a fluid with equation of state parameter w, one can show using the Friedmann equations that the scale factor behaves as

$$a \propto t^{\frac{2}{3(1+w)}}, \tag{5.53}$$

assuming that $a \to 0$ as $t \to 0$ and $w \neq -1$. Hence the Hubble parameter behaves as

$$H(t) = \frac{2}{(3+3w)t} \tag{5.54}$$

such that when $w < -1$, one must have $t < 0$ for an expanding Universe ($H(t) > 0$). Therefore we choose $t < 0$ in figure 5.9.

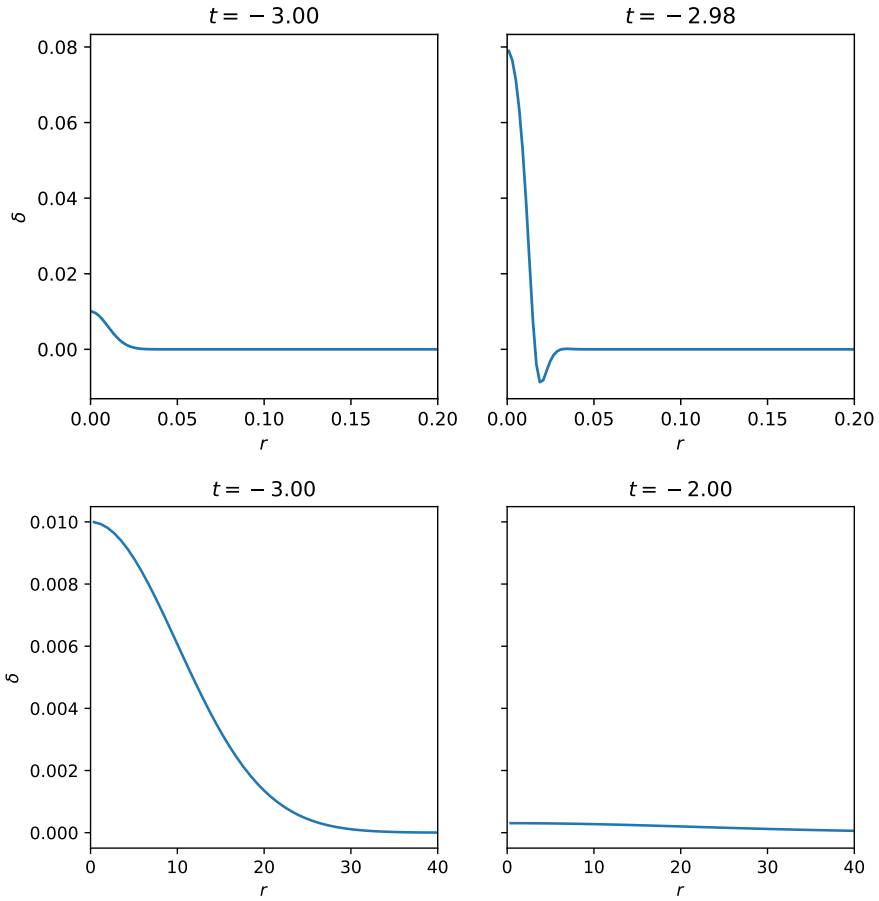

Figure 5.9: Evolution of a fluid in the phantom energy regime with $w = -4/3$, for a perturbation with $\lambda \ll \lambda_J$ (top) and $\lambda \gg \lambda_J$ (bottom), where $\lambda_J = 8.9$. The initial conditions for both are given by a Gaussian perturbation in density (equations (5.47)), with parameters $\delta_0 = 0.01$.

5.6 Conclusion

We develop both an analytic and a numerical approach for solving the field equations for a fluid with a fixed equation of state. We find an exact analytic solution for linearised equations, which we believe is novel. The analytical approach we used yields a relationship between the velocity and density, which can be used to select the appropriate growing modes that can be used as an initial condition for evolving clusters and voids. Applying this to radiation as an example, we find oscillatory behaviour at sub-horizon scales, which helps visualise the initial stages of what becomes the BAO.

We then develop a numerical method for solving the PDEs, which we use to compare behaviour of radiation waves in the non-linear and linear regimes. We find that non-linear oscillations travel faster than linear waves, which is interestingly analogous to non-linear waves

in ocean waves. We also show that linear approximations underestimate the growth of perturbations in the non-linear regime. In the future this numerical method could be extended to study a perturbation of any size, such as the evolution of a cluster or a void, as done in Chapter 4 for a pressureless system.

We also examine fluids with a negative equation of state parameter. We find that at small scales, when perturbations are inside the horizon, they grow exponentially. At larger scales, fluids behave differently depending on the value of w. When $-1/3 < w < 0$, large scale perturbations can grow in a stable manner. However when $w < -1/3$, the pressure's repulsive gravitational effect 'wins' over the attractive gravitational effect of matter, and the fluid cannot support the growth of structure at large scales. This is supported by the exact analytic solution we find for $w = -2/3$, for which only decaying modes can be found.

Chapter 6

Effect of pressure on photon propagation

In our calculations so far in this thesis, we have ignored the effects of pressure on a photon. Photon geodesics are often considered in cosmology, for example when finding the redshift-distance relation for a particular cosmology or when calculating the ISW effect due to an inhomogeneity, but often pressure effects are ignored (Romano & Vallejo 2015; Nadathur et al. 2014). In this Chapter, we explore how pressure can affect the photon path and momentum, by first carrying out a full analysis including pressure, using the spherical top-hat model used in Nandra et al. (2013) as an example in Section 6.3. We show that interestingly, pressure can be found fully analytically in the top-hat model. We finally show in Section 6.5 using an example that we can indeed ignore the effects of pressure on photon propagation without compromising accuracy, and present our conclusions in 6.6.

6.1 The model

We consider a spherical massive object of mass $M(r,t)$ with uniform density $\rho_i(t)$ and radius $a(t)$, embedded in an expanding universe with uniform exterior density $\rho_e(t)$. The interior 'bubble' and exterior universe have expansion rates characterised by the Hubble parameters $H_i(t)$ and $H_e(t)$, respectively. The model is shown in figure 6.1.

The total mass enclosed within a sphere of radius r is defined as $M(r,t)$. From now on, dependencies on both (r,t) will normally be suppressed, unless they are on r or t alone. Clearly,

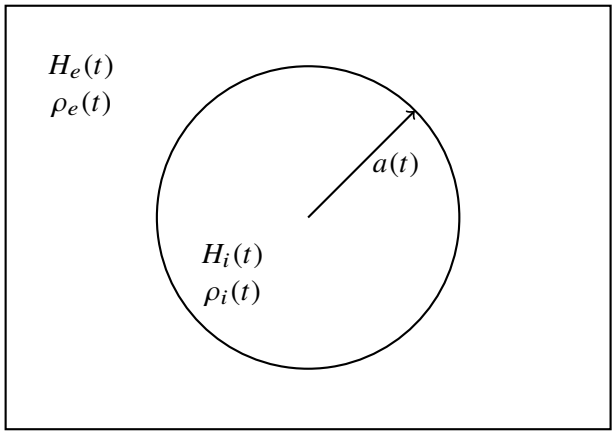

Figure 6.1: Our inhomogeneous model, with a spherical region of uniform density $\rho_i(t)$ and radius $a(t)$, embedded in an exterior region with uniform density $\rho_e(t)$. The rate of expansion in the interior and exterior are characterized by the Hubble parameters, $H_i(t)$ and $H_e(t)$, respectively.

the expression for M is given by

$$M = \begin{cases} \frac{4}{3}\pi\rho_i(t)r^3, & r \leq a(t), \\ \frac{4}{3}\pi\rho_e(t)r^3 + m(t), & r > a(t), \end{cases} \tag{6.1}$$

where $m(t) \equiv \frac{4}{3}\pi(\rho_i(t) - \rho_e(t))a(t)^3$.

The exterior Hubble parameter, $H_e(t)$, is taken to represent the expanding outer universe. However, the interior Hubble parameter, $H_i(t)$, can be chosen to be of any value or sign, to represent an expanding or collapsing inner object. Thus, our model imposes density and velocity profiles for the interior and exterior regions and the general-relativistic dynamical equations determine the required pressure profile in each region.

6.2 Summary of results from Nandra, Lasenby & Hobson (2013)

Nandra et al. (2013) derived the metric for the spherical system shown in figure 6.1, using the tetrad-based formalism. In this Section, we present the results from that paper which are used in this thesis. From now on, we use v instead of g_2, as g_2 can be interpreted as the fluid velocity. The subscripts $_e$ and $_i$ will be used to indicate the exterior and interior regions, respectively. Differentiation with respect to cosmic time t with be denoted by a prime.

In NLH3, the equations in (1.13) and (1.12) were solved to find the tetrad components for interior and exterior regions. One also assumes that f_1 and g_2 are continuous along the boundary of the object, and that at large r, the metric tends to the usual FRW cosmology. The results are summarised below.

In the exterior region, we have the following expressions:

$$f_{1,e} = -\frac{3H_e(t)\,(\rho_e(t)+p_e)}{\rho_e'(t)}, \tag{6.2}$$

$$g_{1,e} = \sqrt{1-\frac{2m(t)}{r}+\left(H_e(t)^2-\tfrac{8}{3}\pi\rho_e(t)-\tfrac{1}{3}\Lambda\right)r^2+\frac{9H_e^2(t)m'(t)}{16\pi^2\rho_e'^2(t)r^4}\left(\tfrac{8}{3}\pi\rho_e'(t)r^3+m'(t)\right)}, \tag{6.3}$$

and

$$v_e = rH_e(t)+\frac{3m'(t)H_e(t)}{4\pi r^2\rho_e'(t)}. \tag{6.4}$$

In the interior region, we have

$$f_{1,i} = -\frac{3H_i(t)\,(\rho_i(t)+p_i)}{\rho_i'(t)}, \tag{6.5}$$

$$g_{1,i} = \sqrt{1+r^2\left(H_i^2(t)-\tfrac{8}{3}\pi\rho_i(t)-\tfrac{1}{3}\Lambda\right)}, \tag{6.6}$$

and

$$v_i = rH_i(t). \tag{6.7}$$

The time derivatives of densities and $a(t)$ are given by

$$\rho_e'(t) = -3H_e(t)\,(\rho_e(t)+p_\infty(t))\,, \tag{6.8}$$

$$\rho_i'(t) = \frac{H_i(t)\rho_e'(t)}{H_e(t)}\left(\frac{\rho_i(t)+p_b(t)}{\rho_e(t)+p_b(t)}\right), \tag{6.9}$$

and

$$a'(t) = \frac{aH_i(t)\rho_e(t)}{\rho_e(t)+p_b(t)}, \tag{6.10}$$

where $p_b(t)\equiv p(a(t),t)$, the pressure at the boundary between the interior and exterior regions, and $p_\infty(t)$ is the pressure as $r\to\infty$, which is the pressure of the external cosmological model.

The pressure gradient of a spherically-symmetric system is given by the generalised Oppenheimer-Volkov equation, which was derived in NLH3 using some of the equations given in (1.13):

$$\frac{\partial p}{\partial r} = -\left(\frac{\rho+p}{r}\right)\frac{M+4\pi r^3p-\frac{1}{3}\Lambda r^3+r^2v\partial_r v-4\pi r^4(\rho+p)(\partial_t M)^{-1}v\partial_t v}{(1+v^2)r-2M-\frac{1}{3}\Lambda r^3}. \tag{6.11}$$

For large r, we expect the external universe to tend to the usual FRW solutions. Thus, for large r, we have the boundary conditions

$$\begin{aligned} f_1 &\to 1,\\ g_1 &\to \sqrt{1-\frac{kr^2}{R^2(t)}},\\ g_2 &\to rH_e(t). \end{aligned} \tag{6.12}$$

where $R(t)$ is the scale factor for the exterior universe and $k = -1, 0, 1$ for an open, flat or closed exterior universe, respectively (Nandra et al. 2013). Imposing these boundary conditions for f_1 and g_1 on equations (6.2) and (6.3) gives us the cosmological field equations,

$$H_e^2(t) - \tfrac{8}{3}\pi\rho_e(t) - \tfrac{1}{3}\Lambda = -\frac{k}{R^2(t)}, \tag{6.13}$$

$$H_e'(t) = \tfrac{1}{3}\Lambda - H_e^2(t) - \tfrac{4}{3}\pi\left(\rho_e(t) + 3p_\infty(t)\right), \tag{6.14}$$

Using the definition of $m(t)$, and equations for $\rho_i'(t)$ and $a'(t)$ given by (6.9) and (6.10), we can derive an alternative expression for the external fluid velocity.

$$v_e = rH_e(t) - \frac{a^3(t)}{r^2}\left(H_e(t) - H_i(t)\right). \tag{6.15}$$

Similarly, we can derive the following expression for g_1, where we momentarily drop t dependencies:

$$g_{1,e}^2 = 1 - \frac{2m}{r} + (H_e^2 - \tfrac{8}{3}\pi\rho_e - \tfrac{1}{3}\Lambda)r^2 + \frac{a^3}{r}(H_i - H_e)\left[2H_e + \frac{a^3}{r^3}(H_i - H_e)\right]. \tag{6.16}$$

As noted in NLH3, the system is completely determined by the interior and exterior Hubble parameters, $H_i(t)$ and $H_e(t)$, the pressure at infinity, $p_\infty(t)$, and the radius $a_* \equiv a(t_*)$ and density $\rho_* \equiv \rho_i(t_*)$ of the interior object at some reference time t_*.

6.3 Expressions for pressure

We now attempt to derive expressions for pressure in this model. In this Section only, we suppress t dependencies as well as dependencies on both (r, t) for brevity.

First we can find the expression for p_i. The general Oppenheimer-Volkov equation (6.11) can be combined with equations (6.1) and (6.7), to yield

$$\frac{\partial p_i}{\partial r} = \frac{(\rho_i + p_i)\, r\left[3H_iH_i'(\rho_i + p_i) - \rho_i'\left(H_i^2 + \frac{4}{3}\pi(\rho_i + 3p_i) - \frac{1}{3}\Lambda\right)\right]}{\rho_i'\left[1 + r^2(H_i^2 - \frac{8}{3}\pi\rho_i - \frac{1}{3}\Lambda)\right]}. \tag{6.17}$$

Recalling that $p_i = p_i(r, t)$ and ρ_i is independent of r, we can solve the equation above analytically to find

$$p_i = \frac{-\rho_i g_{1,i}\,(b + cp_b) + bg_{1,b}\,(\rho_i + p_b)}{g_{1,i}\,(b + cp_b) - cg_{1,b}\,(\rho_i + p_b)} \tag{6.18}$$

where $g_{1,i}$ is given by equation (6.6), and we have defined the functions $g_{1,b}(t)$, $b(t)$ and $c(t)$ by

$$\begin{aligned} g_{1,b} &= g_{1,i}(a(t), t) \\ b(t) &= \left(H_i^2 + \tfrac{4}{3}\pi\rho_i - \tfrac{1}{3}\Lambda\right)\rho_i' - 3H_iH_i'\rho_i, \\ c(t) &= 4\pi\rho_i' - 3H_iH_i', \end{aligned} \tag{6.19}$$

For the exterior region, we can replace M and v in the Oppenheimer-Volkov equation with (6.1) and (6.4) respectively. Then one can perform the differentials of v and expand, resulting in an expression which can be integrated right away to yield a solution for the exterior pressure in terms of an elliptic integral.

First, let us define the following functions which depend on r and t:

$$\begin{aligned} j(r,t) &= \frac{3}{4\pi\rho_e'^3}\int_a^r d\bar{r}\Big(\tfrac{16}{3}\pi^2\bar{r}^3\rho_e'^3 + 3H_e^2(m'\rho_e'' - m''\rho_e') - H_eH_e'\rho_e'(3m' + 4\pi\bar{r}^3\rho_e')\Big) \\ &\qquad \cdot \frac{1}{\bar{r}^2}\Big(1 - \frac{2m}{\bar{r}} + \Big(H_e^2 - \tfrac{8}{3}\pi\rho_e - \tfrac{1}{3}\Lambda\Big)\bar{r}^2 + \frac{9H_e^2m'}{16\pi^2\rho_e'^2\bar{r}^4}\Big(\tfrac{8}{3}\pi\rho_e'\bar{r}^3 + m'\Big)\Big)^{-\frac{3}{2}} \\ &= \frac{3}{4\pi\rho_e'^3}\int_a^r d\bar{r}\,\frac{\frac{16}{3}\pi^2\bar{r}^3\rho_e'^3 + 3H_e^2(m'\rho_e'' - m''\rho_e') - H_eH_e'\rho_e'(3m' + 4\pi\bar{r}^3\rho_e')}{\bar{r}^2\; g_{1,e}^3\big|_{r=\bar{r}}}, \end{aligned} \tag{6.20}$$

and

$$\begin{aligned} l(r,t) &= \Big\{1 - \frac{2m}{r} + \Big(H_e^2 - \tfrac{8}{3}\pi\rho_e - \tfrac{1}{3}\Lambda\Big)r^2 + \frac{9H_e^2m'}{16\pi^2\rho_e'^2r^4}\Big(\tfrac{8}{3}\pi\rho_e'r^3 + m'\Big)\Big\}^{1/2}. \\ &= g_{1,e} \end{aligned} \tag{6.21}$$

where one can see $j(r,t)$ is in the form of an elliptic integral.

With the functions defined above, we can write the external pressure in the form

$$p_e = \frac{1}{l(r,t)\,(j(r,t) + q(t))} - \rho_e(t), \tag{6.22}$$

where $q(t)$ is a 'constant of integration'. The explicit form of $q(t)$ can be found by applying the boundary conditions on the external pressure. It can be shown that this solution for p_e is valid for a non-uniform interior density (with uniform exterior density) as well.

Note that for a flat cosmology, the r^3 terms in the integrand of $j(r,t)$ cancel out, as differentiating equation (6.13) implies that

$$H_e(t)H_e'(t) = \tfrac{4}{3}\pi\rho_e'(t) \tag{6.23}$$

such that $j(r,t)$ is given by

$$j(r,t) = \frac{9H_e}{4\pi\rho_e'^3}(H_e(m'\rho_e'' - m''\rho_e') - H_e'm'\rho_e')\int_a^r d\bar{r}\,\frac{1}{\bar{r}^2\; g_{1,e}^3\big|_{r=\bar{r}}} \tag{6.24}$$

when flat.

Using the boundary condition $p_e(a(t),t) = p_b(t)$ to eliminate $q(t)$, we find

$$p_e = \frac{1}{l(r,t)\left(j(r,t) + \left[g_{1,b}(t)\,(p_b(t) + \rho_e(t))\right]^{-1}\right)} - \rho_e(t). \tag{6.25}$$

Both the interior and exterior pressures require the explicit form for $p_b(t)$. This can be found by applying the boundary condition at infinity to the exterior pressure equation; i.e. $p_e(r \to \infty, t) = p_\infty(t)$. The resulting expression can be rearranged to find $p_b(t)$ in terms of $H_e(t)$, $H_i(t)$, $a(t)$, $\rho_e(t)$, $\rho_i(t)$, and $p_\infty(t)$ in the form of an elliptic integral. Having found $p_b(t)$, the interior pressure is now defined via equation (6.18).

$H_e(t)$, $H_i(t)$ and $p_\infty(t)$ can be chosen freely. $\rho_e(t)$ is then easily found using the cosmological field equations (6.13) and (6.14). The variables $a(t)$ and $\rho_i(t)$ are dependent on $p_b(t)$, as shown in equations (6.9) and (6.10). Once we know the density ρ_* and radius a_* of the central object at some time t_*, we know $p_b(t_*)$, and we can integrate equations (6.9) and (6.10) through time, using the form for p_b found earlier. This defines the entire system.

6.4 Photon equations

We now derive the equations that define the null geodesic for a radially moving photon, where pressure is not assumed to be zero. For a radially moving photon, we can easily find from the metric by setting $ds^2 = 0$ that $\frac{dr}{dt} = \frac{1}{f_1}(g_2 \pm g_1)$. For an incoming photon we take the minus sign; hence, we can let the 4-momentum of the radially incoming photon in our (t, r, θ, ϕ) coordinate system be given by

$$[p^\mu] = (\dot{t}, \dot{r}, \dot{\theta}, \dot{\phi}) \propto \Phi(\lambda)\,(f_1, -(g_1 - g_2), 0, 0)\,, \tag{6.26}$$

where a dot refers to differentiation with respect to λ, an affine parameter along the photon's worldline. Then, the geodesic equations determine how Φ evolves with λ:

$$\frac{d\Phi}{d\lambda} = -\frac{\Phi^2}{f_1 g_1}\left(g_1^2\frac{\partial f_1}{\partial r} - g_1 g_2\frac{\partial f_1}{\partial r} - f_1 g_2\frac{\partial g_1}{\partial r} + f_1 g_1\frac{\partial g_2}{\partial r} - f_1^2\frac{\partial g_1}{\partial t}\right) \tag{6.27}$$

$$\frac{dt}{d\lambda} = \Phi f_1 \tag{6.28}$$

$$\frac{dr}{d\lambda} = -\Phi\,(g_1 - g_2) \tag{6.29}$$

Hence we can integrate the set of first-order ordinary differential equations above simultaneously to calculate the position and energy of the photon along its trajectory.

6.5 An example

As a test, we can adopt a flat Λ cosmology. We choose the Hubble parameters $H_e(t) = \sqrt{\frac{\Lambda}{3}}\coth\left(\frac{3}{2}\sqrt{\frac{\Lambda}{3}}t\right)$ and a time-shifted form for H_i, $H_i(t) = H_e(t - t_c)$. This time-shifted form for $H_i(t)$ is in fact the expected solution for a pressureless universe, as it also satisfies the

Table 6.1: Parameters and initial conditions used

Exterior Hubble parameter	$H_e(t_0)$	72 km s^{-1}Mpc^{-1}
Interior Hubble parameter	$H_i(t_0)$	-111 km s^{-1}Mpc^{-1}
Current time	t_0	13.1 Gyr
Cosmological constant	Λ	1.14×10^{-35} s^{-2}
Collapse time	t_c	19.6 Gyr
Emission time	t_*	1.6 Gyr
Φ at emission	$\Phi(t_*)$	1
r at emission	$r(t_*)$	1400 Mpc
Size of bubble	$a(t_*)$	4 Mpc
Interior density	$\rho_i(t_*)$	1.05×10^{-27} kg m^{-3}
Reception time	t_R	12.5 Gyr

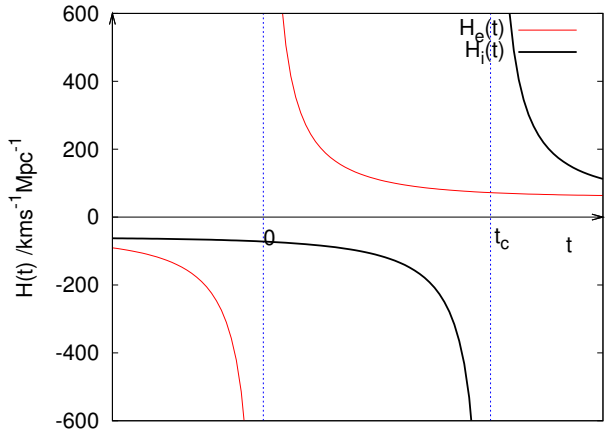

Figure 6.2: Plot of $H_e(t) = \sqrt{\frac{\Lambda}{3}} \coth\left(\frac{3}{2}\sqrt{\frac{\Lambda}{3}}t\right)$ and $H_i(t) = H_e(t - t_c)$, for $t_c > 0$. We can see that when $0 < t < t_c$, $H_e(t) > 0$ and hence the exterior is expanding, and $H_i(t) < 0$ i.e. the interior is collapsing. Note that as t approaches t_c, the interior region collapses to a point.

Einstein field equations, albeit with a different constant of integration in time. We expect deviations from the pressureless equations to be small; hence choosing this form for $H_i(t)$ enables us to see how pressure affects quantities, such as density and photon energy, from those expected using the pressureless equations. Changing the value of t_c with respect to t controls the collapse or expansion of the interior, as seen in figure 6.2.

We can see from equations (6.13) and (6.14) that this implies the form for the exterior density to be $\rho_e(t) = \frac{\Lambda}{8\pi}\text{cosech}^2\left(\frac{3}{2}\sqrt{\frac{\Lambda}{3}}t\right)$ for $\Lambda > 0$, $k = 0$ and $p_\infty = 0$. $\rho_i(t)$ and $a(t)$ were found numerically by solving the equations for the boundary pressure and integrating their time derivatives simultaneously.

We apply the model to a collapsing interior, i.e. with t_c chosen such that $t < t_c$ and hence $H_i(t) < 0$. We release the photon at a fixed time $t_* \approx 1.6$ Gyr and distance $r(t_*) = 1400$ Mpc, and follow its path as approaches the centre. The initial conditions and parameters used to make

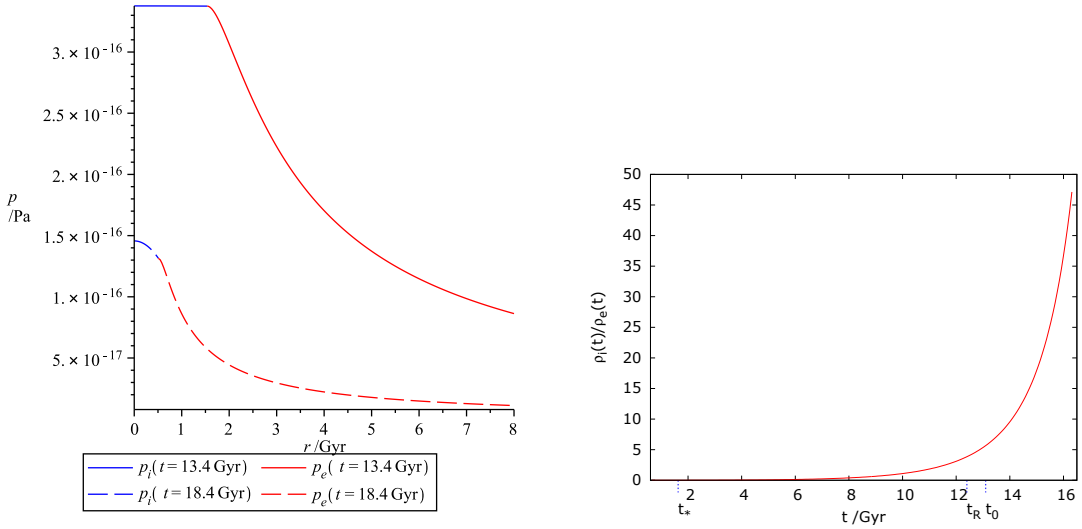

(a) Pressure profile at $t = 13.4$ Gyr, 18.4 Gyr

(b) Evolution of $\rho_i(t)/\rho_e(t)$

Figure 6.3: Pressure profile and $\rho_i(t)/\rho_e(t)$ of the system described in Table 6.1

this plot are presented in table 6.1. The pressure profile of the system is shown in figure 6.3(a). As expected, the pressure goes as $1/r$ as $r \to \infty$. At earlier times, pressure in the interior is higher despite the lower density, due to the impact of the exterior cosmology on the boundary pressure.

To consider the effect of pressure on the photon path, we can compare how Φ and r are affected by the inclusion of pressure. We calculated how the quantities along the photon path vary when pressure is excluded from the momentum equations in (6.27) to (6.29). The same initial conditions of $a(t_*)$, $\rho_i(t_*)$ and emission time and location were used. The results are presented in figure 6.4. Figure 6.4(a) shows that pressure has no significant cumulative effect on Φ up to 10^{-7}. The jumps are due to numerical error; it shows that the effects due to pressure are so small that they are buried in the numerical error. As this error is much smaller than the magnitude of Φ (which is of order 10^{-1}), we can choose to ignore this. As for the r coordinate, we can see that excluding pressure slightly underestimates the r coordinate of the incoming photon, but the magnitude is very small. For example, the fractional error in r from neglecting pressure at $t = 8$ Gyr is approximately -3×10^{-7}.

We have also assumed that p/ρ is small in most places. Figure 6.5(a) shows this assumption is valid at t_0. To verify this is the case for other times, we plot the evolution of this ratio, evaluated at the boundary, as the value of p/ρ is expected to be highest at this point (see figure 6.5(a)). We can see the ratio remains small at most times; the assumption $p/\rho \ll 1$ breaks down at times earlier than 0.6 Gyr.

Assuming a perfect gas with mean molecular weight of $m_p/2$, we can convert this ratio to

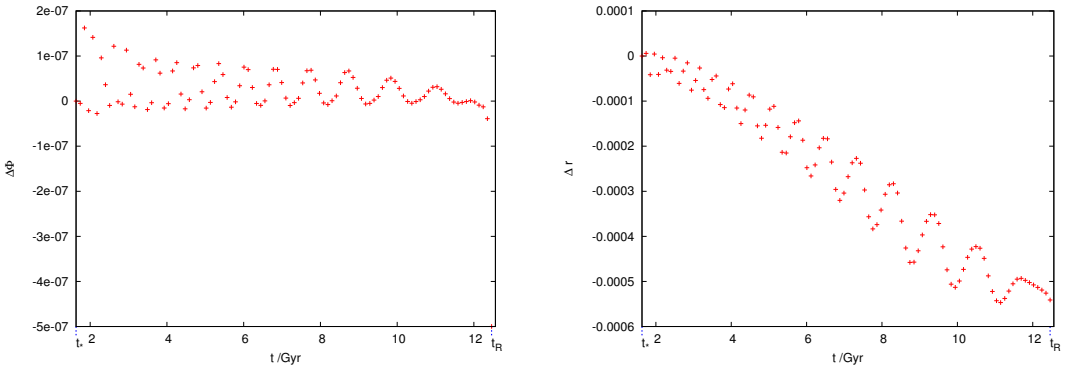

(a) (b)

Figure 6.4: (a)Plot of $\Delta\Phi \equiv \Phi_{p=0} - \Phi$; i.e. the difference in Φ when pressure is included and excluded, with conditions listed in Table 6.1. Considering that $\Phi(t_*) = 1$ and $\Phi(t_R) \approx 0.224$, the fractional difference is about 10^{-6} in magnitude. The jumps are present because the numerical error is comparable or larger than the difference introduced due to pressure. (b) Plot of $r_{p=0} - r$, the difference in the r coordinate of the incoming photon, with and without pressure. Excluding pressure introduces a small cumulative error to the r coordinate.

temperature by using

$$T(r,t) = \frac{m_p}{2k_B}\left[\frac{p(r,t)}{\rho(t)}\right]_{\text{SI}}. \tag{6.30}$$

This is shown on the right hand vertical axis in figure 6.5(a).

We note that we are imposing a particular form for $H_e(t)$ and $H_i(t)$. This means that at times far away from the reference point, we may have an unrealistic system. In fact, when we try to evaluate various quantities at early times, the system breaks down. At early times we are forcing a collapsing interior into a very rapidly expanding exterior; hence we are imposing an unrealistic equation of state. We could circumvent this problem by, for example, embedding a curved interior which expands along with the exterior at early times, and collapses in the future. However, for the moment, as we are focusing on phenomena around our current epoch, we leave this for future study.

Lastly, we note that the energy of photon, $E \propto \Phi f_1$, from equation (6.26). From (6.2) and (6.8), we find

$$f_{1,e} = 1 + \frac{p_e}{\rho_e(t)}. \tag{6.31}$$

for $p_\infty = 0$. Similarly, from (6.5) and (6.9),

$$f_{1,i} = \frac{\left(1 + \frac{p_b(t)}{\rho_e(t)}\right)\left(1 + \frac{p_i}{\rho_i(t)}\right)}{1 + \frac{p_b(t)}{\rho_i(t)}} \tag{6.32}$$

Since we expect $p/\rho \ll 1$, we can see that pressure has a minimal effect on f_1, such that $E \approx \Phi$.

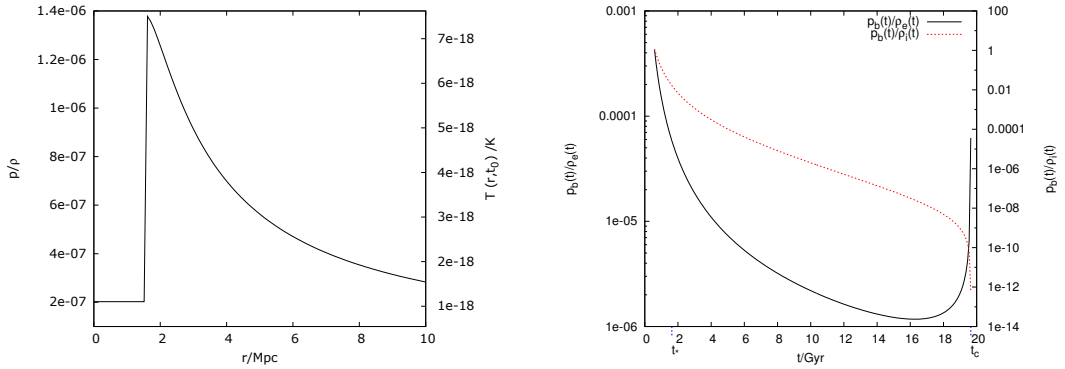

(a) (b)

Figure 6.5: (a) Temperature profile today. The ratio p/ρ is shown on the left hand axis in natural units, and this is scaled to reflect temperature in Kelvin on the right hand axis. (b) The evolution of $\frac{p_b(t)}{\rho_e(t)}$(left axis, black line) and $\frac{p_b(t)}{\rho_i(t)}$ (right axis, red dotted line) with time. We can see that the value of p/ρ evaluated just *outside* the boundary (i.e. $\frac{p_b(t)}{\rho_e(t)}$) remains small even at times as early as $t \approx 0.6$ Gyr. It increases significantly as t approaches t_c, because of the increase in $p_b(t)$. We also plot p/ρ just *inside* the boundary. $\frac{p_b(t)}{\rho_i(t)}$ is larger at early times and is equal to unity at $t \approx 0.6$ Gyr.

The above results demonstrate that within the equations that determine the photon's path, we can ignore pressure without a significant bias. Ignoring pressure makes the calculations much simpler and has no significant effect on the position and energy of the photon, except at very early times when pressures are very high.

6.6 Conclusion

To conclude, we find explicit expressions for pressure that are valid in the spherical top-hat model shown in figure 6.1. Using an example consisting of a collapsing spherical inhomogeneity embedded in an exterior expanding universe, we show that the effect of pressure on the photon momentum is minimal and that it is hence valid to ignore pressure when calculating the photon's path and energy.

Chapter 7

Conclusions and future work

In this dissertation we have shown that spherically-symmetric solutions in relativity have many applications in cosmology, ranging from small to large scale structures and early to late epochs of the Universe, using a combination of analytic and numerical techniques at our disposal.

A natural place to start was to develop a theoretical understanding of the relationship between the tetrad-based method and the more commonly used LTB approach. Our study revealed that the LTB approach contains a gauge ambiguity, which does not exist in our choice of 'physical' coordinates. The tetrad-based method offers an Eulerian picture of the fluid that makes it easier to interpret physically. An interesting toy model to consider was the generalised Swiss cheese model, which then led us verify Birkhoff's theorem and show that the common analogy to Gauss' theorem, namely that the gravitational field in a vacuum in a spherically-symmetric system is only affected by the mass in the interior, is false in the relativistic case.

We then examined the theoretical basis of the so-called $R_{\rm H} = ct$ cosmological model, whose theoretical claims start off by considering the very same Swiss cheese model considered in our previous chapter. We showed that both the theoretical foundation for the $R_{\rm H} = ct$ model and the zero active mass condition that it requires are based on incorrect reasoning. This naturally led us to consider the behaviour of various horizons during the relativistic evolution of homogeneous and isotropic cosmological models.

Having examined the theoretical framework behind the tetrad-based vs. LTB methods, we then applied our understanding to a specific cosmological context in Chapter 4, in the form of the Draco void and its effect on the CMB. Our numerical computations enabled us to see explicitly that varying the velocity profile whilst keeping the density profile relatively similar

can have a large effect on the CMB. This exposed clearly some weaknesses in using the LTB method for fitting a model to the data, that one can circumvent via a careful consideration of both the density and velocity profiles. For a more rigorous, realistic model of a void, one can fit to the galaxy survey and the CMB data but we leave this for future work as our aim was to illustrate the differences in the effects on the CMB from small deviations in the parameterisation of models.

Having studied the Swiss cheese model in Chapter 2, which contains uniform density in the interior and exterior regions, and a system with a continuous density but zero pressure in the study of voids in Chapter 4, a natural progression was to consider a fluid with a more realistic continuous density profile and non-zero pressure. With pressure included, we showed in Chapter 5 that the equations can no longer be reduced to a system of first-order differential equations; hence this required us to find a way to numerically solve partial differential equations, which we achieved using the finite difference method and 4th order Runge-Kutta for the evolution over time. Here we focused on a perfect fluid having a fixed equation of state parameter w, but our method is not restricted to such fluids. Hence, it would be interesting in the future to apply the method to model spherically symmetric systems outside the cosmological field, for example effects in the interstellar medium.

When studying the effects of pressure, we focused on small perturbations in fluids in the early epoch, and found that in the linear regime, analytic solutions can be found. Comparing with the non-linear behaviour obtained via numerical means, we found that non-linear perturbations have larger growth, and faster propagation speeds. In future work this could be used to calculate non-linear effects on the BAO. We also took the opportunity to examine fluids with negative pressure, which revealed interesting insights into the role of scale and the range of w that affects whether a stable growth of structure is possible. We found that our results are consistent with previous results from Fabris & Martin (1997).

In our studies we tried to keep our calculations as analytic as possible before using numerical methods. For instance in Chapter 6, we find the analytical expressions for pressure for the spherical top-hat density profile. Another example is the exact analytical solutions to the linearised field equations for fluids with fixed equation of state, presented in Chapter 5. Obtaining analytic expressions is instrumental in furthering our intuition in cosmological phenomena. In the future it would be illuminating to solve for the evolution of linear perturbations for a general equation of state w, which could be used to aid our understanding of the evolution of the acoustic oscillations while the Universe undergoes cooling. Our analytic expressions also enable us to choose the appropriate growing and decaying modes, that one can use to select the correct mode to evolve into large non-linear structure.

In the final chapter, we use the toy model with a spherical top-hat density to calculate

the effect of pressure on the propagation of a photon. We show that except for very early epochs when pressures are exceptionally high, pressure has a negligible effect on the energy and position of a photon, hence verifying that the common practice of neglecting pressure effects on photon propagation is indeed valid.

There are many areas within astrophysics and cosmology where our methods can be applied in the future. One area is the study on the effect of local inhomogeneities on observed cosmological parameters. As discussed in the Introduction there has been a resurgence of interest on modelling inhomogeneities, due to the possibility that a local void may explain the effect of dark energy. It has also been suggested that the apparent discrepancy between the value of the Hubble constant obtained from the CMB and Type Ia supernovae can be explained by a local underdensity (Romano & Vallejo 2015; Wu & Huterer 2017). As most of the existing studies on such effects use the LTB method, it would be of interest to apply our methods to these problems. Another possible area of research is the effects of dark energy on the Local Group and the investigation of where the transition to the Hubble flow will occur. This could in principle then be compared to the data from the Gaia satellite, which will provide accurate proper motion as well as radial velocity measurements. In addition, spherically symmetric solutions will also be of increasing importance in tests of modified gravity models, and we believe that our tetrad-based methods will be useful in this area as well.

Bibliography

Alexander S., Biswas T., Notari A., Vaid D., 2009, J. Cosmology Astropart. Phys., 9, 025

Alonso D., García-Bellido J., Haugbølle T., Vicente J., 2010, Phys. Rev. D, 82, 123530

Angulo R. E., Baugh C. M., Frenk C. S., Lacey C. G., 2008, MNRAS, 383, 755

Bassett B., Hlozek R., 2010, in Ruiz-Lapuente P., ed., , Dark Energy: Observational and Theoretical Approaches. Cambridge University Press, p. 246

Bene G., Csapo A., 2010, preprint (arXiv:1002.4610)

Bikwa O., Melia F., Shevchuk A., 2012, MNRAS, 421, 3356

Bilicki M., Seikel M., 2012, MNRAS, 425, 1664

Biswas T., Notari A., 2008, J. Cosmology Astropart. Phys., 6, 021

Bolejko K., Célérier M.-N., 2010, Phys. Rev. D, 82, 103510

Bondi H., 1947, MNRAS, 107, 410

Brechet S. D., Hobson M. P., Lasenby A. N., 2007, Classical and Quantum Gravity, 24, 6329

Brouzakis N., Tetradis N., Tzavara E., 2007, J. Cosmology Astropart. Phys., 2, 013

Brouzakis N., Tetradis N., Tzavara E., 2008, J. Cosmology Astropart. Phys., 4, 008

Caldwell R. R., Stebbins A., 2008, Physical Review Letters, 100, 191302

Carroll S. M., Hoffman M., Trodden M., 2003, Phys. Rev. D, 68, 023509

Cartan É., 1937, La théorie des groupes finis et continus et la géométrie différentielle: traitées par la méthode du repère mobile. Cahiers scientifiques, Gauthier-Villars, https://books.google.co.uk/books?id=wELvAAAAMAAJ

Célérier M.-N., 2012a, preprint (arXiv:1203.2814)

Célérier M.-N., 2012b, A&A, 543, A71

Chevallier M., Polarski D., 2001, International Journal of Modern Physics D, 10, 213

Clarkson C., 2012, Comptes Rendus Physique, 13, 682

Clifton T., Zuntz J., 2009, MNRAS, 400, 2185

Colless M., et al., 2001, MNRAS, 328, 1039

Cooray A., Sheth R., 2002, Phys. Rep., 372, 1

Courant R., Friedrichs K., Lewy H., 1928, Mathematische Annalen, 100, 32

Crocce M., Scoccimarro R., 2008, Phys. Rev. D, 77, 23533

Dabrowski Y., Hobson M. P., Lasenby A. N., Doran C. J. L., 1998, MNRAS, 302, 15

Dabrowski Y., Hall M. J., Sawicki I. L., Lasenby A. N., 1999, MNRAS, 318, 9

Del Campo S., Cárdenas V. H., Herrera R., 2012, Modern Physics Letters A, 27, 1250213

Dyer C. C., Roeder R. C., 1972, ApJ, 174, L115

Dyer C. C., Roeder R. C., 1973, ApJ, 180, L31

Eddington A. S., 1930, MNRAS, 90, 668

Einstein A., 1915, Sitzungsberichte der Königlich Preußischen Akademie der Wissenschaften (Berlin), Seite 844-847.,

Einstein A., 1917, Sitzungsberichte der Königlich Preußischen Akademie der Wissenschaften (Berlin), Seite 142-152.,

Einstein A., 1923, Zeitschrift für Physik, 16, 228

Einstein A., Straus E. G., 1945, Reviews of Modern Physics, 17, 120

Eisenstein D. J., Hu W., 1998, ApJ, 496, 605

Eisenstein D. J., et al., 2005, ApJ, 633, 560

Eisenstein D., Seo H.-J., White M., 2007, ApJ, 664, 660

Ellis G. F. R., van Elst H., 1999, in Lachièze-Rey M., ed., NATO Advanced Science Institutes (ASI) Series C Vol. 541, NATO Advanced Science Institutes (ASI) Series C. pp 1–116 (arXiv:gr-qc/9812046)

Fabris J. C., Goncalves S. V. B., 2000, Brazilian Journal of Physics, 33, 834

Fabris J. C., Martin J., 1997, Phys. Rev. D, 55, 5205

Feng L., Lu T., 2012, preprint, (arXiv:1203.1784)

Finelli F., Garcia-Bellido J., Kovacs A., Paci F., Szapudi I., 2014, preprint (arXiv:1405.1555v1)

Finelli F., Garcia-Bellido J., Kovacs A., Paci F., Szapudi I., 2016, MNRAS, 455, 1246

Flanagan É. É., Kumar N., Wasserman I., 2013, Phys. Rev. D, 88, 043004

Fleury P., 2014, J. Cosmology Astropart. Phys., 6, 054

Fleury P., Dupuy H., Uzan J.-P., 2013, Phys. Rev. D, 87, 123526

Friedmann A., 1922, Zeitschrift für Physik, 10, 377

Friedmann A., 1924, Zeitschrift für Physik, 21, 326

Garcia-Bellido J., Haugbølle T., 2008, J. Cosmol. Astropart. Phys., 2008, 003

Geshnizjani G., Chung D. J., Afshordi N., 2005, Phys. Rev. D, 72, 023517

Groth E., Peebles P., 1975, A&A, 41, 143

Gullstrand A., 1922, Ark. Mat. Astron. Fys., 16, 1

Guzik J., Bernstein G., Smith R. E., 2007, MNRAS, 375, 1329

Harwit M., 1998, Astrophysical Concepts. Springer-Verlag, New York

Hawking S. W., Ellis G. F. R., 1973, The large-scale structure of space-time. Cambridge University Press

Hu W., Sugiyama N., 1995, ApJ, 444, 489

Hu W., Sugiyama N., 1996, ApJ, 471, 542

Hubble E., 1929, Proceedings of the National Academy of Science, 15, 168

Israel W., 1966, Il Nuovo Cimento B, 44, 1

Israel W., 1967, Il Nuovo Cimento B, 48, 463

Jassal H. K., Bagla J. S., Padmanabhan T., 2005, Phys. Rev. D, 72, 103503

Kainulainen K., Marra V., 2009, Phys. Rev. D, 80, 127301

Kaloper N., Kleban M., Martin D., 2010, Phys. Rev. D, 81, 104044

Kantowski R., 1969, ApJ, 155, 89

Kim D. Y., Lasenby A. N., Hobson M. P., 2016, MNRAS, 460, L119

Lake K., Abdelqader M., 2011, Phys. Rev. D, 84, 044045

Lasenby A., Doran C., Gull S., 1998, Phil. Trans. R. Soc. Lond. A, 356, 487

Lasenby A. N., Doran C. J. L., Hobson M. P., Dabrowski Y., Challinor A. D., 1999, MNRAS, 302, 748

Lasky P. D., Lun A. W. C., 2006, Phys. Rev. D, 74, 084013

Lavaux G., Wandelt B. D., 2012, ApJ, 754, 109

Lavinto M., Räsänen S., 2015, J. Cosmology Astropart. Phys., 10, 057

Lavinto M., Räsänen S., Szybka S. J., 2013, J. Cosmology Astropart. Phys., 12, 051

Lemaître G., 1927, Annales de la Société Scientifique de Bruxelles, 47, 49

Lemaître G., 1931, MNRAS, 91, 483

Lemaître G., 1933, Annales de la Société Scientifique de Bruxelles, A53, 51

Lewis G. F., 2013, MNRAS, 432, 2324

Lewis G. F., van Oirschot P., 2012, MNRAS, 423, L26

Linder E. V., 2003, Physical Review Letters, 90, 091301

Lynden-Bell D., Bičák J., 2016, Class. Quantum Grav., 33, 075001

Mackenzie R., Shanks T., Bremer M. N., Cai Y.-C., Gunawardhana M. L. P., Kovács A., Norberg P., Szapudi I., 2017, MNRAS, 470, 2328

Marcos-Caballero A., Fernández-Cobos â. R., Martínez-González E., Vielva P., 2016, MNRAS, 460, 15

Marra V., Kolb E. W., Matarrese S., Riotto A., 2007, Phys. Rev. D, 76, 123004

Marra V., Kolb E. W., Matarrese S., 2008, Phys. Rev. D, 77, 023003

McVittie G. C., 1933, MNRAS, 93, 325

McVittie G. C., 1956, General relativity and cosmology. Chapman & Hall, London UK

Melia F., 2003, The Edge of Infinity - Supermassive Black Hole in the Universe. Cambridge University Press, doi:10.1017/CBO9780511536366

Melia F., 2007, MNRAS, 382, 1917

Melia F., 2009, Int. J. Mod. Phys. D, 18, 1113

Melia F., 2012, J. Cosmol. Astropart. Phys., 2012, 029

Melia F., 2015, MNRAS, 446, 1191

Melia F., 2016, Frontiers of Physics, 11, 119801

Melia F., 2017, Frontiers of Physics, 12, 129802

Melia F., Maier R. S., 2013, MNRAS, 432, 2669

Melia F., Shevchuk A. S. H., 2012, MNRAS, 419, 2579

Melia F., Wei J.-J., Wu X.-F., 2015, AJ, 149, 2

Meszaros P., 1974, A&A, 37, 225

Mimoso J. P., Le Delliou M., Mena F. C., 2013, Phys. Rev. D, 88, 043501

Misner C. W., Sharp D. H., 1964, Physical Review, 136, 571

Misner C. W., Thorne K. S., Wheeler J. A., 1973, Gravitation. Freeman & Company, New York

Mitra A., 2014, MNRAS, 442, 382

Montanari F., Durrer R., 2011, Phys. Rev. D, 84, 023522

Nadathur S., Lavinto M., Hotchkiss S., Räsänen S., 2014, Phys. Rev. D, 90, 103510

Nakao K.-i., 1995, preprint (arXiv:gr-qc/9507022)

Nandra R., Lasenby A. N., Hobson M. P., 2012a, MNRAS, 422, 2931

Nandra R., Lasenby A. N., Hobson M. P., 2012b, MNRAS, 422, 2945

Nandra R., Lasenby A. N., Hobson M. P., 2013, Phys. Rev. D, 88, 044041

Nolan B. C., 1998, Phys. Rev. D, 58, 064006

Nolan B. C., 1999, Classical and Quantum Gravity, 16, 1227

Nolan B. C., 2014, Classical and Quantum Gravity, 31, 235008

Nolan B. C., 2017, preprint (arXiv:1707.07612)

Nottale L., 1982, A&A, 110, 9

Oppenheimer J. R., Volkoff G. M., 1939, Phys. Rev., 55, 374

Painlevé P., 1921, C. R. Acad. Sci. (Paris), 173, 677

Pisani A., Sutter P. M., Hamaus N., Alizadeh E., Biswas R., Wandelt B. D., Hirata C. M., 2015, Phys. Rev. D, 92, 083531

Planck Collaboration et al., 2016, A&A, 594, A13

Plebański J., Krasiński A., 2006, An Introduction to General Relativity and Cosmology

Rees M. J., Sciama D. W., 1968, Nature, 217, 511

Robertson H. P., 1935, ApJ, 82, 284

Robertson H. P., 1936a, ApJ, 83, 187

Robertson H. P., 1936b, ApJ, 83, 257

Romano A. E., Chen P., 2011a, Int. J. Mod. Phys. D, 20, 2823

Romano A. E., Chen P., 2011b, J. Cosmol. Astropart. Phys., 2011, 12

Romano A. E., Vallejo S. A., 2015, Europhysics Letters, 109, 39002

Sakharov A., 1966, Soviet Journal of Experimental and Theoretical Physics, 22, 241

Schwarzschild K., 1916, in Sitzungsberichte der Königlich Preussischen Akademie der Wissenschaften zu Berlin. pp 189–196

Shafer D. L., 2015, Phys. Rev. D, 91, 103516

Siegel E. R., Fry J. N., 2005, ApJ, 628, L1

Slepian Z., Eisenstein D. J., 2016, MNRAS, 457, 24

Smith R. E., Scoccimarro R., Sheth R. K., 2007, Phys. Rev. D, 75, 063512

Sussman R. A., 2009, Phys. Rev. D, 79, 025009

Sussman R. A., Quiros I., González O. M., 2005, General Relativity and Gravitation, 37, 2117

Sutter P. M., Lavaux G., Wandelt B. D., Weinberg D. H., 2012, ApJ, 761, 44

Szapudi I., et al., 2014, preprint (arXiv:1406.3622)

Szybka S. J., 2011, Phys. Rev. D, 84, 044011

Tegmark M., et al., 2004, ApJ, 606, 702

Thorne K., Blandford R., 2017, Modern Classical Physics: Optics, Fluids, Plasmas, Elasticity, Relativity, and Statistical Physics. Princeton University Press, https://books.google.co.uk/books?id=U1S6BQAAQBAJ

Tokutake M., Yoo C.-M., 2016, J. Cosmology Astropart. Phys., 10, 009

Tolman R. C., 1934, Proc. Natl. Acad. Sci. U.S.A., 20, 169

Valkenburg W., 2009, J. Cosmology Astropart. Phys., 6, 10

Vanderveld R. A., Flanagan É. É., Wasserman I., 2008, Phys. Rev. D, 78, 083511

Vilenkin A., Shellard E. P. S., 2000, Cosmic Strings and Other Topological Defects. Cambridge University Press, http://www.cambridge.org/mw/academic/subjects/physics/theoretical-physics-and-mathematical-physics/cosmic-strings-and-other-topological-defects?format=PB

Walker A. G., 1937, Proc. London Math. Soc, s2-42, 90

Wei J.-J., Wu X.-F., Melia F., 2013, ApJ, 772, 43

Wei J.-J., Wu X.-F., Melia F., Wei D.-M., Feng L.-L., 2014a, MNRAS, 439, 3329

Wei J.-J., Wu X.-F., Melia F., 2014b, ApJ, 788, 190

Wei J.-J., Wu X.-F., Melia F., 2015, MNRAS, 447, 479

Weyl H., 1929, Zeitschrift fur Physik, 56, 330

Winter D., 2000, J. Math. Phys., 41, 5582

Wu H.-Y., Huterer D., 2017, MNRAS, 471, 4946

Zhang S.-N., Yi S., 2012, in Int. J. Mod. Phys. Conf. Ser.. pp 419–430, doi:10.1142/S2010194512006642

Zibin J. P., 2008, Phys. Rev. D, 78, 043504

Zibin J., 2014, preprint (arXiv:1408.4442)

Zibin J. P., Moss A., Scott D., 2008, Physical Review Letters, 101, 251303

d'Inverno R., 1992, Approaches to Numerical Relativity. Cambridge University Press, doi:10.1017/CBO9780511524639

van Oirschot P., Kwan J., Lewis G. F., 2010, MNRAS, 404, 1633

van Oirschot P., Kwan J., Lewis G. F., 2015, in The 13th Marcel Grossmann Meeting. pp 1567–1569, doi:10.1142/9789814623995_0226